Mathesis of star formation – from kpc to parsec scales

Dissertation

zur

Erlangung des Doktorgrades (Dr. rer. nat.)

der

Mathematisch-Naturwissenschaftlichen Fakultät

der

Rheinische Friedrich-Wilhelms-Universität Bonn

vorgelegt von

Guang-Xing Li

aus

Hohhot, Inner Monglia, China

Bonn, November 2014

Angefertigt mit Genehmigung der Mathematisch Naturwissenschaftlichen
Fakultät der Rheinischen Friedrich-Wilhelms-Universität Bonn

1. Referent: Prof. Dr. Karl Menten
2. Referent: Prof. Dr. Pavel Kroupa

Tag der Promotion   20.11.2014

Erscheinungsjahr **2015**

Knowledge is not for knowing: knowledge is for cutting.

Michel Foucault

SUMMARY

In this thesis I present a series of studies aiming to understand the formation of stars from gas in the Milky Way. Generally speaking, I will progress from larger to smaller scales.

The kilo-parsec scale ($\sim 10^3$ parsec $\sim 10^{21}$ cm) is the scale at which dynamics of the molecular clouds is coupled to dynamics of the Milky Way disk. Here we present an observational study of molecular gas at $49.5° < l < 52.5°$ and -5.0 km s^{-1} $< v_{\text{lsr}} <$ 17.4 km s^{-1}. The molecular gas is found in the form of a huge ($\gtrsim 500$ pc) filamentary gas wisp. It has a large physical extent and a velocity dispersion of ~ 5 km s^{-1}. The filamentary gas wisp is composed of two molecular clouds and an expanding bubble. The length of the gas wisp exceeds by much the thickness of the molecular disk of the Milky Way, and this is consistent with the cloud-formation scenario in which gas is cold prior to the formation of molecular clouds.

Molecular clouds ($1 - 100$ parsec) are the nurseries of the stars. There are many indications that molecular clouds are turbulence-dominated objects. However, it is not clear what role gravity plays. We propose a new method (`G-virial`) to quantify the role of gravity in molecular clouds. Our new method takes the gravitational interactions between all pixels in 3D position-position-velocity data cube into account, and generates maps of the importance of gravity in 3D position-position-velocity space. With our method we demonstrate that gravity plays an importance role in the individual regions in the Perseus and Ophiuchus molecular cloud, and find that high values of `G-virial` are reached in cluster-bearing regions. We also demonstrate the capability of our method in finding regions and quantifying the properties of the regions in the clouds.

Protostellar outflow (~ 1 parsec) is a prominent process accompanying the formation of stars. In this work, we theoretically investigate the possibility that the outflow results from interaction between the wind and the ambient gas in the form of turbulent entrainment. In our model, the ram-pressure of the wind balances the turbulent ram-pressure of the ambient gas, and the outflow consists of the ambient gas entrained by the wind. We demonstrate that the outflow phenomena can be naturally generated through this process, and discuss the potential usage of outflows as a probes of the dynamical state of the turbulent molecular gas.

Publications

Chapter 2 was published as:

A 500 pc filamentary gas wisp in the disk of the Milky Way, **Li, G.-X.**, Wyrowski, F., Menten, K., & Belloche, A. 2013, A&A, 559, A34.

Chapter 3 was submitted to A&A as :

G-virial: A general method to quantify gravity in molecular clouds, **Li, G.-X**, Wyrowski, F., Megeath, T., Menten, K. Shi, X.

Chapter 4 was published as:

Turbulent entrainment origin of protostellar outflows, **Li, G.-X.**, Qiu, K., Wyrowski, F., & Menten, K. 2013, A&A, 559, A23.

Preface

My subject is matter that exists *between* the stars. If you look into the sky, even with naked eyes you see some dark patches imprinted on the starry Milky Way, and those are the objects of my interest. However the study of the interstellar medium is quite different from the study of other astrophysical objects, such as that of stars or galaxies, where we are interested in the "properties" of the objects. In the study of the interstellar medium, we deal with structures, and therefore the question "What do we define as an object?" and the question "What are the properties of the objects?" are tightly linked. *In other words, in order to study our objects, we need to add a set of labels (physical parameters) to an object. In order to add labels, we need to define an object in the first place.* Therefore the contents of the labels are dependent on what we define as an object. In the traditional sense, astrophysics is "the branch of astronomy that deals with the physics of the universe, including the physical properties of celestial objects, as well as their interactions and behavior" and in interstellar medium study we also need to answer the question "What is an object?", and this will make interstellar medium a special field in astrophysical study.

To break this loop, we need to be brave enough to define our object and establish order, and at the same time we must be aware of the subjective nature of the definition. We must take the risk of imposing a set of structures on our object, then try to get the parameters from our labelling system. We need to establish systematic order, and at the same time we must know what we put in to our definitions. We must be aware that the labelling system comes from our minds, and such a labelling system is essential for our physical understandings. What we need is *mathēsis* – the subjective science of establishing a systematic calculable order for things. *Mathēsis* is something that is derived out of our subjectivity, and in this thesis I will show how a change of the subjective understanding can lead to a change of the *mathēsis* and finally to the establishment of a new field of research (Chapter 3).

If the *mathēsis* restricts our understandings, so does our knowledge. We are constantly gazing into nature with our eyes. Our perception of nature is established with the help of our knowledge, and such knowledge also restricts our ability to identify new phenomena. To some extent, in order to discover new things, we need to "forget" what we know and look with fresh eyes. This also implies questioning the already established "questions". In chapter 2, I will show how a pair of fresh eyes can help with this change.

It is through this way that the internal structure of the thesis should be understood: judging from the table of content, the body of thesis consists of three chapters focusing on different physical scales. There are two reasons for this: First, I work on different subjects since they are connected through the physical processes, e.g. turbulence and gravity. Since these physical processes are intrinsically scale-free, it is possible to study

them at different physical scales. Second, the different subjects have another similarity: they tend to question the already-established framework our knowledge is based on. If a creative research involves "thinking out of the box", then one of the efforts that I made is to break these boxes in the first place.

Contents

---

[1]Part of this chapter has been published as "A 500 pc filamentary gas wisp in the disk of the Milky Way", Li, G.-X., Wyrowski, F., Menten, K., & Belloche, A. 2013, A&A, 559, A34.

3 G-virial: a general method to quantifying gravity in molecular clouds [2]

4 Protostellar outflow as an entrainment phenomenon [3]   **64**

List of Figures

List of Tables

Chapter 1

Introduction

1.1 Evolution of cosmic gas

Today we believe that the universe is composed of baryonic matter, dark matter, and dark energy [Spergel et al., 2007]. However almost all the signals that we see come from ordinary baryonic matter. In today's universe baryonic matter is largely decoupled from the cosmic radiation field and exists in the form of intergalactic medium, interstellar medium and stars and planets.

The evolution of the universe is a process that is largely dominated by gravity. For dark matter this is completely and exclusively true and for ordinary matter this true at the large scale [1]. As a result, stars have become a plausible destiny of the gas. The cosmic evolution of gas is a process where it is accreted into clusters of galaxies, into galaxies, and then assembled into individual molecular clouds and finally into stars. However in each of the steps there are substantial losses.

The subject of this thesis is star formation, and this is part of the whole evolution of the baryons. Here I would like to define the scope by imposing two constraints. The first constraint is on the physical scale. In this thesis I will only study star formation which occurs in galaxies. Therefore I will deal with the final step of the star formation process which converts gas into stars. The second constraint is on the way in which star formation occurs. Star formation can occur in diverse ways: it can occur in a quiescent way along the spiral arms of galaxies, and it can occur violently in giant clumps of high-redshift galaxies [Dekel et al., 2009]. The former mode is relevant for nearby galaxies (e.g. M51, [Schinnerer et al., 2013]) and the latter mode is relevant for high-redshift galaxies with irregular shapes [Elmegreen & Elmegreen, 2005].

---

[1]The common factors that can resist against gravity include kinetic energy, radiation and magnetic fields.

1.2 Star formation in galaxies

1.2.1 Processes of the interstellar medium

The interstellar medium of the Milky Way and other galaxies is composed of several phases [Dalgarno & McCray, 1972, Field et al., 1969]. The reasons why there are different phases include the followings: on the observational side, we see different components with quite different temperatures. On the theoretical side, the separation of phases is caused by different cooling agents in the medium. In other words, discontinuity in physical properties of the gas can be derived from discontinuity in their thermodynamical properties.

In star formation, we are mainly concerned with four phases [McKee & Ostriker, 1977]: the *warm ionized* phase, the *warm neutral* phase, the *cold neutral* phase and the molecular phase. The warm ionized phase is composed of diffuse HII gas with temperatures of 6000-12000 K, and densities ~ 0.1 cm^{-3} [2], and is traced by H$_\alpha$ emission. The cold neutral phase has temperatures of ~ 80–100 K and densities of ~ 50 cm^{-3}. It can be seen as UV and optical absorption features towards bright stars or quasars. The molecular phase is the denser and colder phase that is directly related to star formation. It is composed of H$_2$ gas, and has temperatures of 10–20 K, and densities > 10 cm^{-2}. This phase comprises 30 % of the mass of the Milky Way ISM, but occupies only 0.05% of its volume .

Theoretically speaking, the problem of star formation is a (radiative and magnetic) hydrodynamical problem, and to understand it, we tend ask questions in the following ways: What are the initial conditions of star formation? What are the boundary conditions? What factors dominate the evolution of the objects? For the third question, the commonly-used parameters are dimensionless numbers, and in star formation the important dimensionless numbers include Mach number, virial number and Reynolds number. The Mach number quantifies how much compression has been exerted to the gas. For molecular clouds, going from larger to smaller scales, the Mach number goes down, and at ~ 0.1 pc the Mach number reaches one, which means the compression becomes inefficient [Krumholz & McKee, 2005]. The Reynolds number of the interstellar medium is typically very large. This is why the medium is turbulent [3] [Mac Low & Klessen, 2004]. The virial number quantifies the importance of gravity relative to kinetic motion [4]. Since gravity is important in most of the astronomical situations, a

---

[2]The unit is the number of H$_2$ per cubic centimeter.

[3]A Reynolds number $Re \sim 10^4$ is usually taken as the boundary between laminar flows and turbulent flows.

[4]The definition of virial parameters differs in the literature. It is either $2\,E_{\rm k}/E_{\rm p}$ or $E_{\rm p}/2\,E_{\rm k}$ where $E_{\rm p}$ is the potential energy and $E_{\rm k}$ is the kinetic energy.

larger virial number can be reached at various physical scales [Kauffmann et al., 2013]. However, along with gravity, other factors such as magnetic field may also be important. The importance of magnetic field has recently been recognized [Li et al., 2013c, Li & Henning, 2011, Li et al., 2011].

Another important factor is the dynamical timescale. This is because star formation is not a process which can occur forever. At the large scale, it is restricted by the evolution of the Galactic disk and at the small scale it is restricted by the evolution of protostars. On the large scale, it is found that molecular clouds are constantly evolving. They interact with the stars in the galaxy through gravity and they are constantly interacting with each other through collisions/agglomerations [Tan, 2000, Dobbs & Pringle, 2013]. Therefore the star formation timescale is limited by the lifetimes of molecular clouds. The star formation timescale provides another constraint. The formation of low-mass stars takes 10^7 yrs and the formation of high-mass stars takes 10^4 yrs [5]. This limitation comes from the stellar evolution. The star formation process, which occurs in molecular clouds, has to be faster than the rate at which stars evolve.

The timescale for collapse is the dynamical timescale, which is

$$\frac{t}{\text{yr}} \sim \left(\frac{n_{\text{H}_2}}{5 \times 10^{15}}\right)^{-1/2} , \tag{1.1}$$

where n_{H_2} is the number of H_2 molecules per cubic centimeter. Here a dynamical timescale of 10^7 yr implies a H_2 density of 50 cm^{-2} and a dynamical timescale of 10^4 yr implies a H_2 density of 5×10^7 cm^{-2}. Therefore, massive stars must form in the densest parts of the molecular clouds. It is also worth noting that these dense parts are surrounded by gas halos with lower density, and it is because of this that the formation of massive stars will be accompanied by the formation of a cluster of low and intermediate mass stars.

1.2.2 Galaxy scale

Seen from the galactic scale, the most prominent features are the spiral arms. Spiral arms are created through either gravitational instability that occurs at the disk scale [Toomre, 1964] or perturbations from nearby galaxies [Toomre & Toomre, 1972]. It is still under debate what makes the spiral pattern of the galaxies.

In spite of this, it is possible to understand star formation without knowing the formation mechanism of the spiral arms. It is sufficient to say that the spiral arms are

---

[5]This is the Kelvin-Holmholz timescale. See e.g. http://en.wikipedia.org/wiki/Kelvin-Helmholtz_mechanism
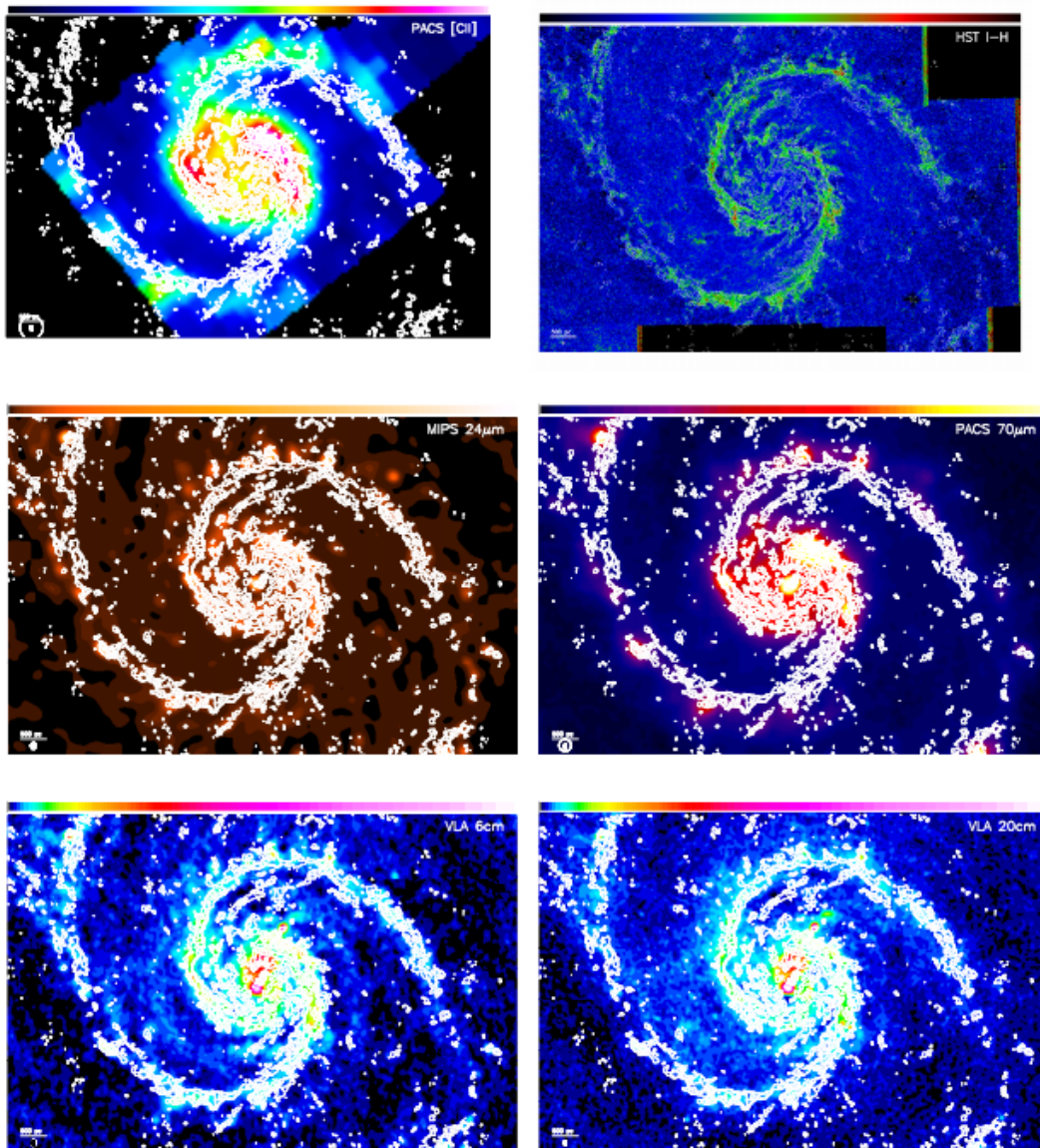
FIGURE 1.1: Comparison of the CO(1-0) line emission in the central part of M51 as observed by the PAWS project overlaid in contours (top right) on the Herschel [CII] line map tracing photo-dissociation (top left), the HST I – H color image tracing extinction (top right), the MIPS HiRes $24\mu m$ image tracing hot dust emission (middle left), the PACS 70 μm image tracing warm dust emission (middle right), the VLA 6 cm image tracing thermal and non-thermal radio continuum (bottom left), and the VLA 20cm image tracing mainly non-thermal radio continuum (bottom right). Figure and caption from Schinnerer et al. [2013]. The physical scale of the images is ~ 10 kpc.

concentrations of atomic gas, molecular gas and stars. In recent years the observations of nearby galaxies have became capable of resolving individual molecular clouds (Fig. 1.1), and in future studies of nearby galaxies and studies of molecular clouds will become more connected [Schinnerer et al., 2013].
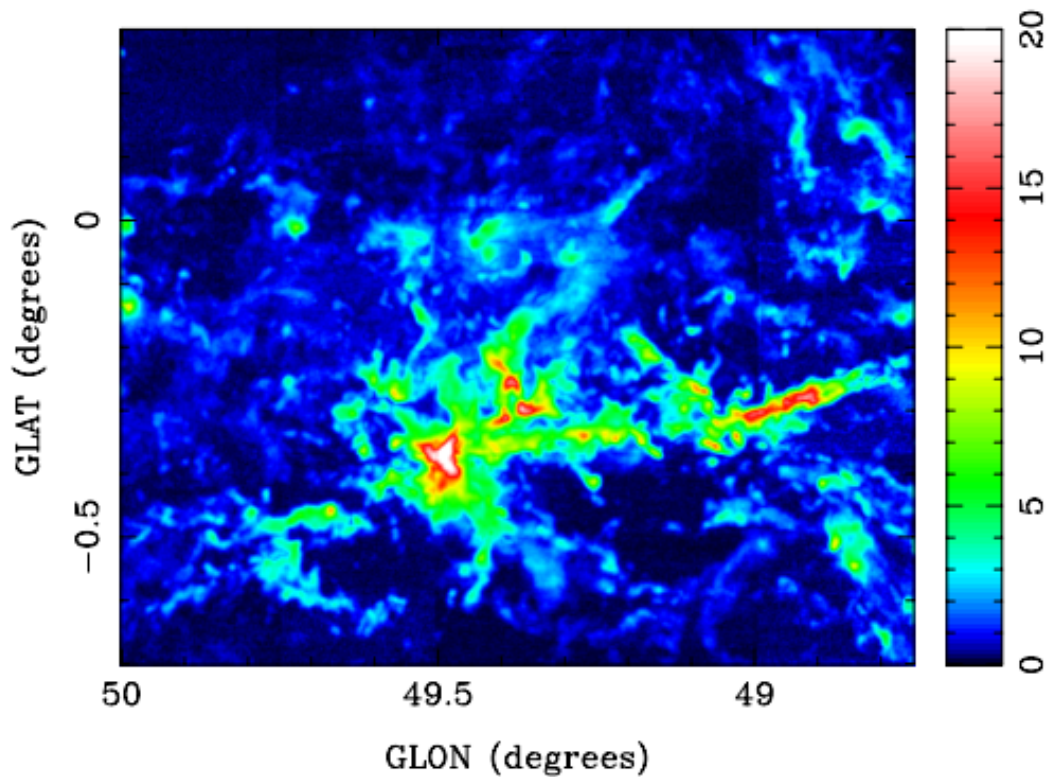
FIGURE 1.2: A typical molecular cloud (W51) in our galaxy. False color image of the ^{13}CO(2-1) maximum line intensity for the velocity range $30 - 85$ km s^{-1}. Color wedge is labeled in T_{mb} (K). From Bieging et al. [2010]. The distance is ~ 6 kpc (derived from galactic rotation). The physical extent is ~ 100 pc.

1.2.3 Molecular cloud

Fig. 1.2 shows a map of the W51 molecular cloud.

The molecular gas exists as a separate phase of the Milky Way ISM since it can cool via the atomic fine-structure lines such as the 157μm transition of C^{+}, as well as the emission from cold dust and CO molecules. On the other hand, it is difficult to heat the dense molecular gas simply because the optical depth is too large even for infrared emission to penetrate [6]. As a result, the only heating source for the dense molecular gas is cosmic-ray heating [Field et al., 1969]. For molecular gas in extreme regions, such as in our galactic center or in high-redshift galaxies, it is also possible that it is heated by dissipation of kinetic energy of turbulence [Guillard et al., 2012].

Molecular clouds are the most massive objects in our galaxy. Their masses range from 10^2 $M_\odot$ to 10^6 $M_\odot$ and their dimensions range from a parsec to tens of parsec [Roman-Duval et al., 2010, Fig. 1.3].

---

[6]Low-density gas can still be heated even by the FUV emission which penetrates into the gas [Hollenbach & Tielens, 1999].
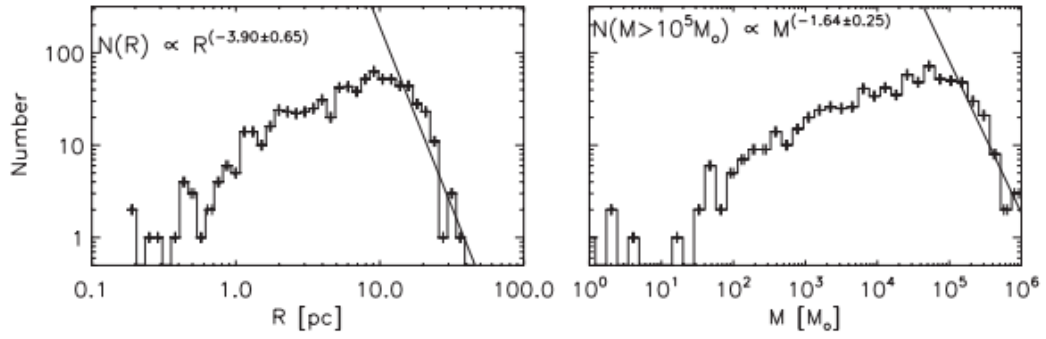
FIGURE 1.3: Histograms of the physical properties of molecular clouds from the GRS survey [Jackson et al., 2006], From Roman-Duval et al. [2010].

Molecular clouds are the nurseries of stars [7], and the formation of stars depends on the dynamics of molecular clouds. On the very large scale, it is believed that molecular clouds are coupled to the warm HI gas through magnetic fields [Crutcher, 1999], and at smaller scale it is believed gravity will dominate over turbulence, and molecular clouds should be subject to collapse.

Since inside the clouds magnetic fields are not thought to dominate, the current theory of molecular cloud dynamics is a combination of supersonic turbulence and gravity. The typical molecular clouds obey an empirical velocity-linewidth relation [Larson, 1972], and this is usually interpreted as an evidence that molecular clouds in the Milky Way and other nearby galaxies are dominated by supersonic turbulence [Ballesteros-Paredes et al., 2007]. On the other hand, gravity is found to be important at different physical scales in molecular clouds [Kauffmann et al., 2013].

1.2.4 Clumps

At smaller scales, dense and compact molecular clumps are found in molecular clouds. The clumps are the innermost, densest regions of the molecular cloud. Observationally, the clumps can be traced by continuum emission from cold dust.

There is no phase separation between the cloud and the clumps. Therefore clumps should not be treated as a different kind of object but should be understood as an integral part of molecular clouds. The concept of clumps is summarized in Williams et al. [2000]. It is found that clumps are mostly roundish objects, and there are far fewer massive clumps that low-mass clumps (Fig. 1.4).

---

[7]Although recently it is being debated if molecular clouds are necessary for star formation to take place [Glover & Clark, 2012].
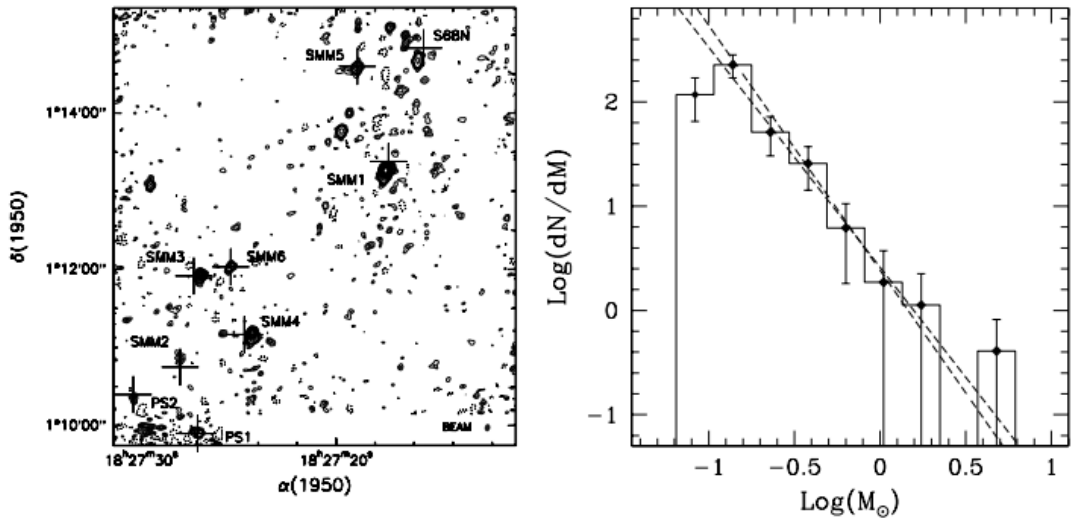
FIGURE 1.4: Image and mass spectrum of the 3mm continuum sources in the Serpens molecular cloud. From [Testi & Sargent, 1998].

The clumps are interesting for two reasons. First, they have high densities. In the case of free-fall the dynamical timescale $t_{\rm ff}$ is related to density by

$$t_{\rm ff} \sim \rho^{-1/2} \ , \tag{1.2}$$

and as a result of their high density, they have a short dynamical timescale, and this is necessary for massive star formation to take place.

1.2.5 Filaments

Molecular clouds have filamentary structure [Bally et al., 1987, Schneider & Elmegreen, 1979, Williams et al., 2000, Goldsmith et al., 2008, Men'shchikov et al., 2010], Recently, thanks to the *Herschel* Space Observatory, which provides high-fidelity maps of the cold ISM traced by the cold dust, it has been realized that filaments are ubiquitous [André et al., 2013] (Fig. 1.5).

The density structure of the filaments can be summarized as follows. First, the interstellar filaments have an universal width, and universal density structure. The typical width of a filament is ~ 0.1 pc and its density structure is usually parametrized as [Whitworth & Ward-Thompson, 2001, Nutter et al., 2008, Arzoumanian et al., 2011]

$$\rho = \frac{\rho_0}{(1 + r/r_0^2)^{p/2}} \ . \tag{1.3}$$
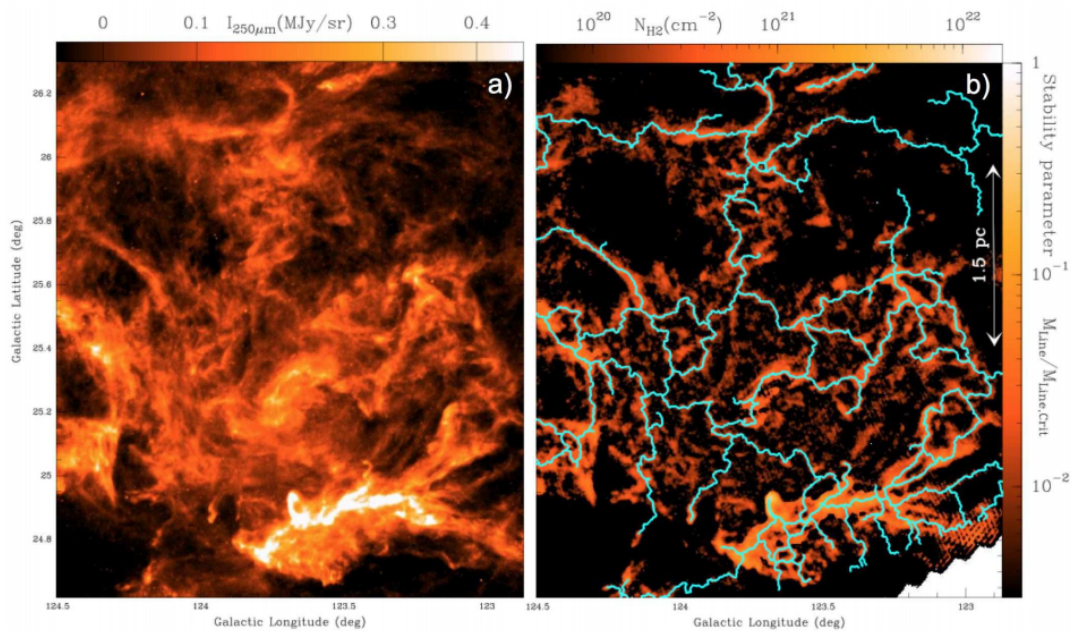
FIGURE 1.5: (a) *Herschel*/SPIRE 250 μm dust continuum map of a portion of the Polaris flare translucent cloud [e.g. Men'shchikov et al., 2010, Ward-Thompson et al., 2010] (b) Corresponding column density map derived from Herschel data [e.g. André et al., 2010]. The contrast of the filaments has been enhanced using a curvelet transform [Starck et al., 2003]. The skeleton of the filament network identified with the DisPerSE algorithm [Sousbie, 2011] is shown in light blue. From [André et al., 2013].

where $r_0 \sim 0.1$ pc and $p \sim 2$. ρ_0 is around 10^{22} cm^{-2} and can vary over two orders of magnitude. Therefore, the filaments have quasi-universal width and density profile. At the same time, the density at the ridges of the filaments can vary quite a lot.

The filaments are intimately related to star formation. It is found that dense cores in which the formation of individual or a multiple of stars takes place, tend to appear in filaments with high column density [Polychroni et al., 2013]. The formation of star clusters occurs where filaments intersect [Peretto et al., 2012].

The theoretical explanation of the filaments is still unclear. The quasi-universal density structure implies that the physical processes that are responsible for *maintaining* the filaments must be robust and well-protected. The theoretical impact of the filaments are still not fully clear. If the ISM is organized in the form of the filaments, it is easy to imagine that the way in which collapse occurs in molecular gas must be quite different from the case without the filaments [Pon et al., 2012].

1.2.6 Protostars and star formation

By zooming into the clumps with submillimeter interferometers, we witness the formation of individual stars/binaries. Here dust continuum emission can trace such regions

since dust has a low opacity and therefore can probe high column density. Furthermore, line emission from molecular transitions with high critical densities can probe high volume density gas in such regions since only there these molecules get excited.

Fig. 1.6, 1.7 show an interferometric observation of a clump, where individual star-forming sites are traced with dust continuum emission and the motion of the gas with lower densities is traced by the CO(2-1) line. The kinetics of the gas in the region is highly complicated. In Fig. 1.6 multiple outflows from a cluster of objects are found through high-resolution interferometer observations [Qiu et al., 2011]. In such clumps star formation occurs in a highly clustered way.

In dense regions a multiple of physical processes are at work: the gas is turbulent [McKee & Tan, 2002], and gravitationally bound [Kauffmann et al., 2013], magnetic field can again become important [Qiu et al., 2013, Tan et al., 2013], at the same time radiation is coming from forming stars, and it is also found that nearly all the protostars can launch outflows during at least part of their lifetime [Arce et al., 2007]. Therefore, inside clumps we are dealing with a multiple of physical processes, and feedback from forming stars in the form of radiation, outflows and stellar winds becomes significant. It is because of these difficulties that the formation of stars is still an unresolved issue.

We are still at the stage of revealing these physical processes. The effect of outflows can be traced through interferometer observations of molecular lines such as low-J transitions of the CO molecule, and the fragmentation process can be traced by interferometer observations of dust continuum emission or line emission from dense gas tracers such as CS. Magnetic fields have been resolved for an increasing number of sources [Qiu et al., 2013], and the effect of radiation can be constrained by studying the temperature structure of the molecular gas with complex molecules. Our knowledge in this field is still increasing.

1.2.7 Different modes of star formation: clustered or not clustered

It was noted as early as 1785 by William Herschel that stars can from in a clustered way. However, until today, the origin of stellar clusters remains largely a mystery [Lada, 2010].

Star formation can be either clustered or not. Fig. 1.8 show the distribution of protostars in the Ophiuchus and Taurus molecular clouds where the former is representative of the clustered way of star formation while the latter the distributed way.

The connection between molecular gas condensation and star cluster formation has been addressed by Longmore et al. [2012] where the mass and radii of different molecular
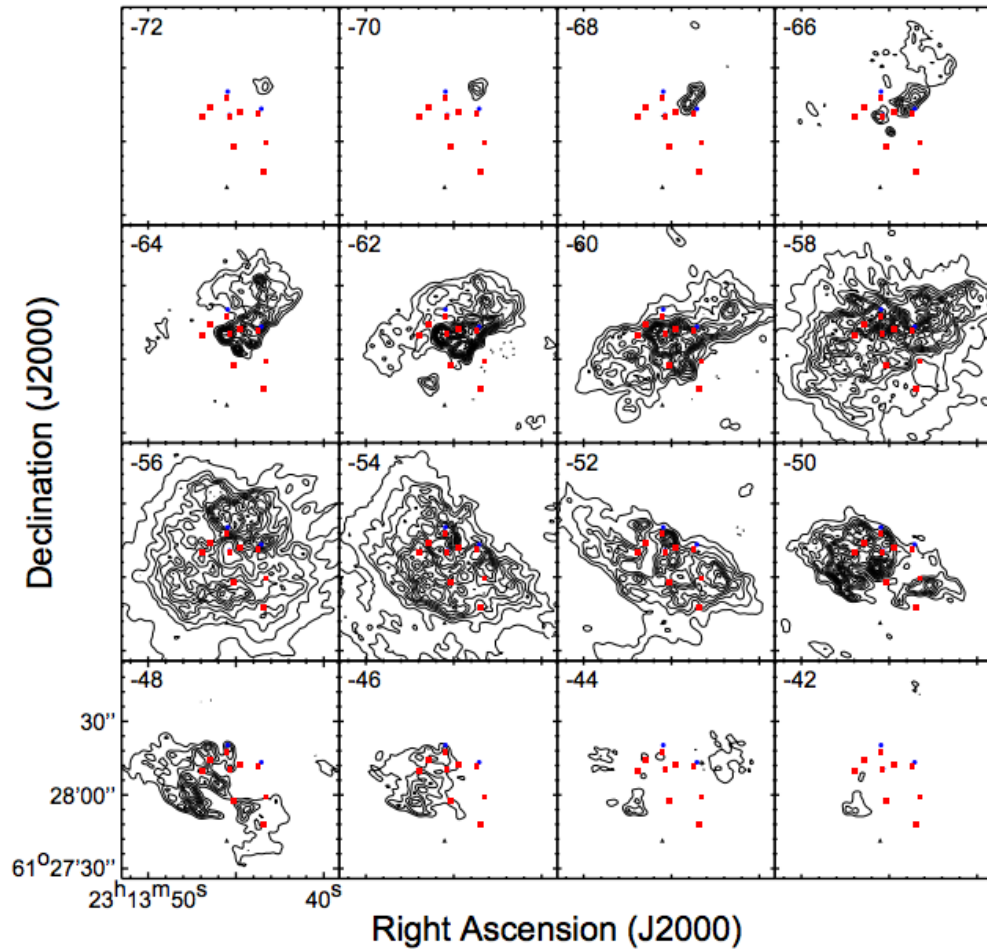
FIGURE 1.6: Zooming into the cluster forming NGC 7538 IRS 1–3 massive star-forming region. The region is hot (~ 200 K) and is rich of organic molecules. The plot shows velocity channel maps of CO (2–1) emission. Different panels correspond to maps of the gas moving at different velocities. The red dots stand for dense cores where the formation of individual and a multiple of stars is taking place. The distance is ~ 2.56 kpc and the physical scale is ~ 1 pc. From [Qiu et al., 2011].

condensations are summarized. Clusters tend to form in molecular condensations of higher density.

Even if the stars are forming in a clustered way it does not guarantee that a star cluster will be formed. This is because such an embedded cluster can sometimes be destroyed later when the molecular gas disperses. The exact destruction process remains unclear. The plausible causes include tidal fields, dynamical relaxation and interactions between clusters and giant molecular clouds [Longmore et al., 2014].
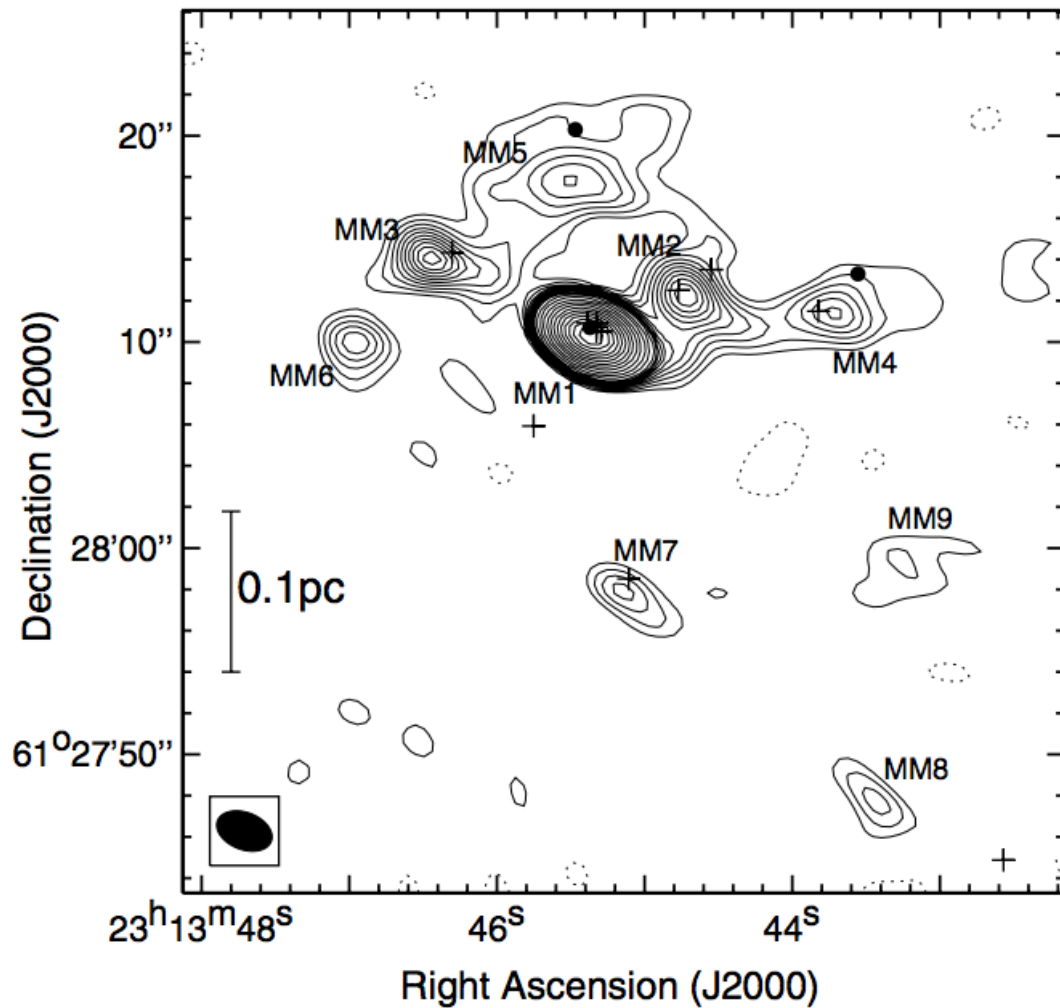
FIGURE 1.7: 1.3 mm continuum emission from the same region as Fig. 1.6. The contour levels increase from 30 to 165 mJy beam^{-1} in steps of 15 mJy beam^{-1} and continuing to 3255 mJy beam^{-1} in steps of $30\times(1,2,3,...,12)$ mJy beam^{-1}; dotted contours show negative emission with absolute levels the same as that of the positive. [Qiu et al., 2011].

1.2.8 Caveats

By presenting an introduction in this way I need to clarify a few points.

- **The spatial structures of the objects:** In fact, in nearly all the fields of interstellar medium study, we need to deal with complicated structures, and both the clouds and the clumps are objects that are extracted from the observational data with certain algorithms. As a result, their physical properties are parameter-dependent and their boundaries are vague. It is because of this difficulty that structure analysis of gas condensations are becoming popular [Goodman et al., 2009, Rosolowsky et al., 2008].
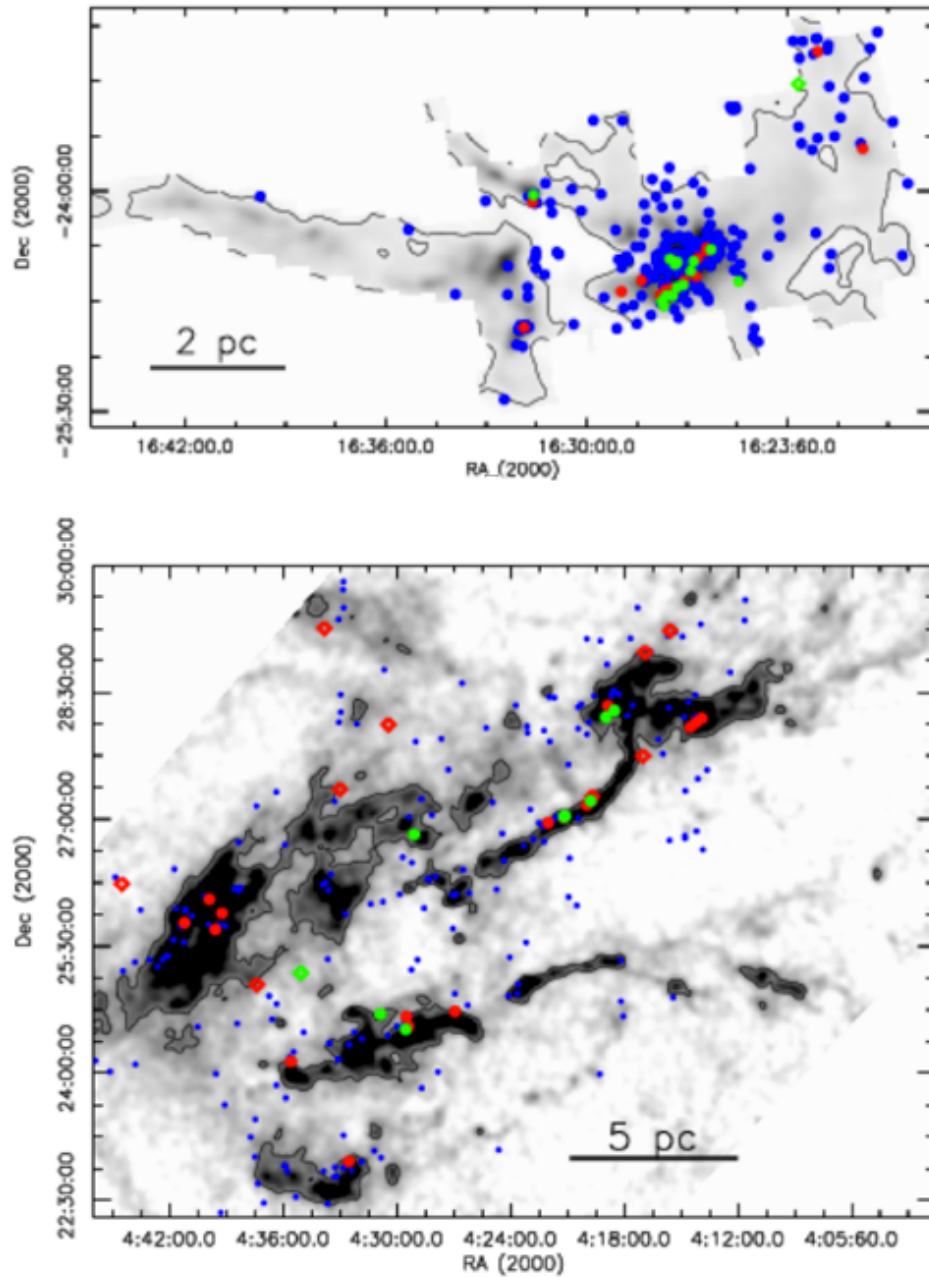
FIGURE 1.8: Ophiuchus and Taurus extinction map. Shown are all Class IIs (blue), rising spectrum protostar candidates (red), and at spectrum (green) protostar candidates with extinction $A_v > 3$ (circles) and with $A_v < 3$ (diamonds), as well as the $A_v = 3$ contours. From [Kryukova et al., 2012]. The extinction method is described in [Lada et al., 1994].
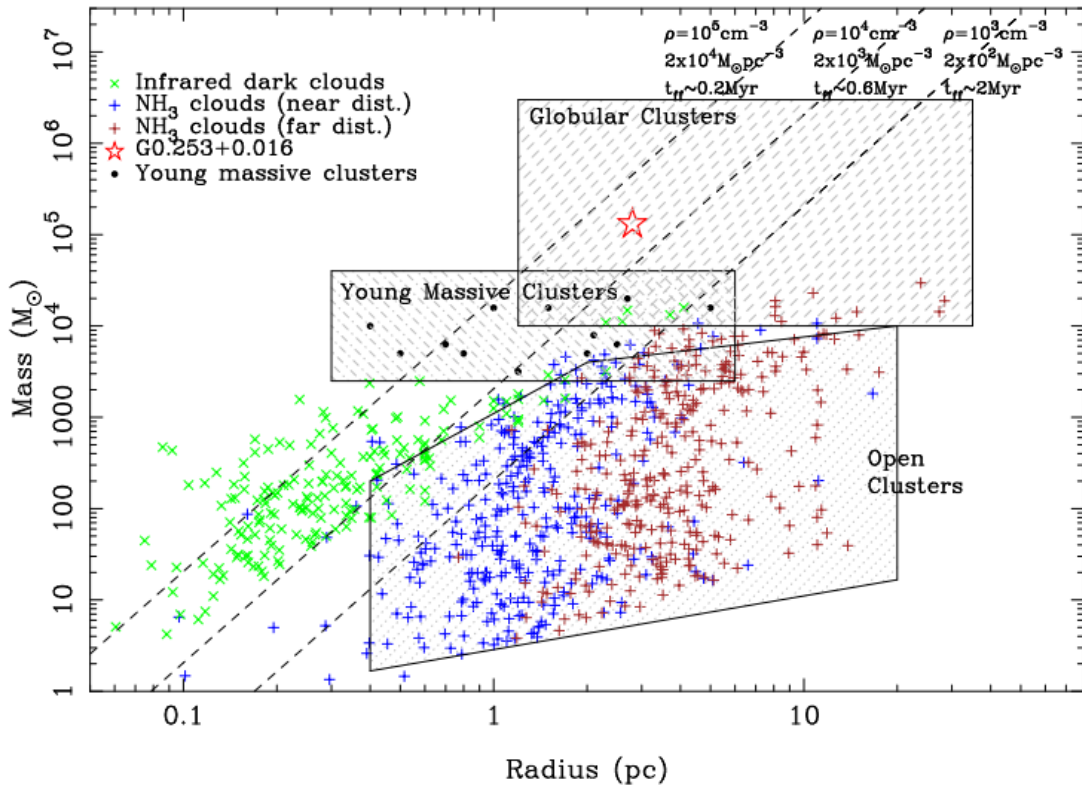
FIGURE 1.9: Radius versus mass for Galactic dense, cluster-forming molecular clouds. Plus symbols show ammonia clouds detected in HOPS [Walsh et al., 2011] (blue/brown denote an assumed near/far kinematic distance, respectively). Green crosses show infrared dark clouds (IRDCs) from the survey of [Rathborne et al., 2006]. The dashed lines show constant density and free-fall time. From [Longmore et al., 2012].

- **The transient nature of the objects:** The second one is the interpretation of the objects, or in other words, what we take as an object. This is a difficulty since the interstellar medium is rapidly evolving, and in most cases, with limited observational time-span we can only access one snapshot of the whole process. As a result, the transient nature of the structures that we see is sometimes neglected. In the past, molecular clouds have been studied by taking them as separate objects, and it is only recently that the interaction (agglomeration, merger) between molecular clouds have been widely recognized [Tan, 2000, Tasker & Tan, 2009, Dobbs et al., 2011].

- **The effect of the environment:** We also need to be aware of the effect of the environment all the time. By reading what I have written, it looks as if the objects are "born" from the environment and would evolve on their own. However the real situation is more complicated, and even galaxies which look like isolated objects, are constantly accreting gas from their surroundings. At the cloud scale

the relevant issue is the "triggered star formation"[Whitworth et al., 1994] where molecular clouds are compressed by expanding bubbles and collapse.

1.3   Scope of the thesis

In this thesis I will present my work on several areas of star formation study. I choose to work on several different subjects in the context of star formation. The different subjects are tightly related.

In Table 1.1 I summarize the physical processes relevant for my work. I list the observational tracers, the observed objects, as well as the physical processes. The factors that are directly-related to my work are underlined.

On the $\sim$ kpc scale, we are at the intersection point between Galactic astrophysics and star formation. It is the physical scale where boundary conditions of molecular clouds are set, and if molecular clouds are dominated by turbulence which is "injected outside the molecular cloud", this is the physical scale where this injection takes place [Klessen, 2011].

On smaller scales (10 – 100 pc), we are in the regime where cold gas exists in the form of molecular clouds. Here star formation depends on the dynamics of the cloud just like *our* weather depends on the dynamics of the clouds in the Earth's atmosphere. Therefore the central theme is *what determines the evolution of molecular clouds*. If we want to understand the behavior of the molecular cloud that leads to the formation of the stars, we need to understand the roles of different factors such as turbulence, gravity and magnetic field. On the other hand, the formation and dispersion of molecular clouds are more complicated. This is discussed in Dobbs & Pringle [2013] and partially covered in Chapter 3.

On a smaller scale ($\sim$ pc), we enter the regime where the effects of star formation become important. The massive stars can heat the gas of the cloud and they can disrupt the entire cloud in different ways (through photons and through stellar winds). Outflows from protostars are also important [8]. We also see copious star formation along with the formation of massive stars. Perhaps this is the most difficult regime since the physical scale is smaller [9] and the physics are complicated. As a result, our understandings are still primitive.

---

[8]However the feedback from outflows is dominated by the low-mass protostars.
[9]Which means they are difficult to observe. This is now changing with ALMA.

Physical Scale	**Physical Processes**	Objects	**Observational Tracers**
~ 10 kpc	Gravitational Instability [Toomre, 1964]	Galaxies Spiral Arms	All wavelengths
~ 1 kpc	Gravitational Instability Galactic Shear [Pringle et al., 2001] Cloud-Cloud Interactions [Tan, 2000]	Sections of Spiral Arms Spurs [Lynds, 1970, Weaver, 1970] **Filamentary Gas Wisps [Li et al., 2013b]**	Dust Extinction [Lada et al., 1994] **CO (molecular gas)** [Wilson et al., 1970] HI (atomic gas)[Ewen & Purcell, 1951]
$10 - 100$ pc	HI – H_2 Phase Transition [Field et al., 1969] Cosmic-ray Heating CO, C^+, C cooling, dust cooling Turbulence [Mac Low & Klessen, 2004], **Gravity** Bubble Expansion [Whitworth et al., 1994]	Giant Molecular Clouds Bubbles [Churchwell et al., 2006]	Dust Extinction **CO (molecular gas)** HI (atomic gas)
~ 1 pc	Cosmic-ray Heating CO, C^+, C cooling, dust cooling Turbulence, Gravity **Molecular Outflows [Li et al., 2013a]** Feedback from Outflows (low-mass objects) [Arce et al., 2007] Radiative feedback (massive stars) Stellar winds (massive stars)	Clumps [Williams et al., 2000] (e.g. ATLASGAL [Schuller et al., 2009] clumps)	Extinction Emission from cold dust CS (dense molecular gas) CO isotopes with low abundance, e.g. $C^{18}O$
~ 0.1 pc	Fragmentation into dense cores Turbulence becomes subsonic [Larson, 1981] Magnetic field?	Dense cores	Interferometer observations of dust continuum emission and molecular lines

TABLE 1.1: A summary of the current status of star formation study. The red column shows the physical processes and the blue column shows the observational tracers. The black column in the middle shows the corresponding objects. All the topics are sorted according to the physical scale, with larger physical scales on the top and smaller physical scales on the bottom. Topics that are tightly related to the thesis are underlined.

1.4   Motivations and contents

The topics of this thesis are arranged according to physical scales. From Chapter 2 to Chapter 4, from $\sim 10^3$ pc to ~ 1 pc.

On the kiloparsec scale, I work on the connection between the dynamics of the Milky Way and the dynamics of molecular clouds. In the past, molecular clouds are usually studied as objects separated from the Galactic disk, and therefore the influence of the environment on the dynamics of the molecular clouds is overlooked. On the other hand, many problems in molecular cloud research arise at large scales. One such example is the driving of turbulence in the cloud. It has been suggested that turbulence in the clouds is injected "from the outside" [Klessen, 2011]. In order to answer how this injection takes place, it is necessary for us to look at the structure of molecular gas *beyond* the cloud scale. This motivates our study in Chapter 2.

On the ~ 100 pc, the dynamics of the molecular cloud is governed by a combination of turbulence, gravity, and magnetic fields. Here I focus on the effect of gravity in molecular clouds. Gravity is a long-range interaction, and is found to be important in the majority of astrophysical situations. In observational studies, the importance of gravity is usually evaluated in terms of the virial parameter. However, this requires a pre-defined boundary of the object. In interstellar medium research, we are dealing with complicated structures, and it is difficult to define such boundaries without introducing certain biases. In Chapter 3, I propose a new method to quantify gravity in molecular clouds, and in this new method, no pre-defined boundary is required.

On the ~ 1 pc scale, the coupling between the forming stars and their environment becomes important. Molecular outflows develop from the interaction between winds from the forming stars and their envelopes. To explain how outflows form is to understand how the interaction takes place. Many of the models of outflows have been established in the 1990s, when the turbulent nature of the ambient gas had not been well-recognized yet. As a result, in the previous outflow models the interaction occurs between wind and a quiescent envelope. Later, I realized that a moderate amount of turbulent motion in the envelope can easily affect the formation of the outflow. In Chapter 4, I provide a self-consistent model of molecular outflows where the effects of the turbulent motion of the ambient gas have been fully taken into account.

In the last chapter I give a summary of the findings and discuss their implications.

Chapter 2

A giant 500 pc molecular filamentary gas wisp [1]

2.1 Introduction

Molecular clouds belong to the densest and coldest parts of the Milky Way interstellar medium [Field et al., 1969, McKee & Ostriker, 1977]. Shielded from interstellar radiation fields, they provide conditions necessary for star formation to take place. Observationally, molecular clouds exhibit a complicated, irregular, and filamentary morphology [Bally et al., 1987, Schneider & Elmegreen, 1979, Williams et al., 2000, Goldsmith et al., 2008, Men'shchikov et al., 2010], and (sub)millimeter-line observations of molecular clouds suggest that the gas in the clouds is moving supersonically. Consensus has not been reached concerning the origin and nature of molecular clouds.

It must be recognized that molecular gas is just one of the phases of the Milky Way interstellar medium, and its evolution is determined by many processes that occur in the disk. To understand it, we must also look into the large-scale structure of the multi-phased interstellar medium, and understand the cloud evolution within this context.

Both observational and theoretical approaches have been taken in this direction. Observationally, the distribution of molecular gas in nearby galaxies can be accessed through millimeter line mapping [e.g. Schinnerer et al., 2013], from which structures such as spiral arms, filaments, and spurs can be identified. Theoretically, the structure of the multi-phased interstellar medium in a galactic disk has been studied through simulating the whole disk with different approaches [Kim & Ostriker, 2002, Shetty & Ostriker,

---

[1]Part of this chapter has been published as "A 500 pc filamentary gas wisp in the disk of the Milky Way", Li, G.-X., Wyrowski, F., Menten, K., & Belloche, A. 2013, A&A, 559, A34.

2006, Tasker, 2011, Dobbs et al., 2011, Van Loo et al., 2013], complemented by analytical calculations [Lee & Shu, 2012]. It was found that filaments or spurs can be created through the combination of gravitational instability of a galactic disk, galactic shear, and frequent encounters/agglomeration between molecular clouds [Pringle et al., 2001, Dobbs & Pringle, 2013].

In the Milky Way, studies of the structure of molecular gas have been confined spatially to the molecular cloud scale or have been limited to the structure of the spiral arms [Larson, 1981, Solomon et al., 1987, Rathborne et al., 2009, Roman-Duval et al., 2009, 2010]. This is partly due to the complicated morphology of molecular gas and partly due to the superposition of the emission of molecular gas from different structures along the line of sight. In spite of these difficulties, it is of both observational and theoretical interest to identify large, coherent molecular structures in the Milky Way apart from the spiral arms, since these structures are natural tracers of the large-scale gas circulation in the Milky Way disk. In contrast to the extragalactic case, where we are limited by the resolution and sensitivity of the telescopes (and the filtering of interferometers), for our Milky Way it is possible to study the kinematics of the molecular gas and the associated star formation with in more detail.

The Milky Way interstellar medium has long been thought to be dynamic. Shells and rims are generally found in the disks of the Milky Way and other galaxies [Churchwell et al., 2006]. It has been proposed that the expansion of H II regions, which creates shells and rims, can collect the interstellar medium into a gravitationally unstable state [Elmegreen & Lada, 1977, Whitworth et al., 1994, Whitworth & Francis, 2002], and trigger star formation. The expansion of the bubbles can also energize the interstellar medium of the Milky Way efficiently [Norman & Ferrara, 1996, Mac Low & Klessen, 2004].

In this work, we present an observational study of the region at $49.5° < l < 52.5°$ in the Milky Way. The molecular gas in the region exhibits a high degree of coherence, and forms a filamentary gas wisp (gas filament) with a length of $\sim 3°$. The eastern part of the filamentary gas wisp sits at the edge of a bubble and is located at $\sim 0.75°$ above the galactic plane. This eastern part is listed in the context of infrared bubbles as one of the "favorites of the Milky-Way-Project volunteers" [Simpson et al., 2012], and it was studied in terms of the G52L nebula by Bania et al. [2012], who claimed that it may be the largest single H II region in the Milky Way. Based on several estimations [Watson et al., 2003, Anderson & Bania, 2009, Roman-Duval et al., 2010, Bania et al., 2012], the filamentary gas wisp has a distance of 9.77 kpc, which implies a physical length of $\gtrsim 500$

pc. This is ~ 5 times longer than the Nessie Nebula reported by Jackson et al. [2010] [2]. The physical length of the filamentary gas wisp exceeds by much the size of a molecular cloud, and this filamentary gas wisp is by far the largest coherent molecular structure identified in the Milky Way. It exhibits a coherent velocity structure, and is composed of several molecular structures, including two molecular clouds and one expanding bubble structure. We present observations and an analysis of the region (Sect. 4.3, 2.3), followed by a detailed discussion focusing on the implications on the dynamics of the Milky Way interstellar medium and the life cycle of molecular gas (Sect. 2.4). In Sect. 2.5 we conclude.

2.2 Archival data

We obtained 3.6 μm and 8 μm data from the GLIMPSE project [Benjamin et al., 2003], which is a fully sampled, confusion-limited, four-band near-to-mid infrared survey of the inner Galactic disk. We obtained 24 μm data from the MIPSGAL project [Carey et al., 2009], which is a survey of the Galactic disk with the MIPS instrument on *Spitzer* at 24 μm and 70 μm.

We obtained ^{13}CO(1-0) molecular line data ($\nu_0 = 110.2$ GHz) from the Galactic Ring Survey [Jackson et al., 2006], which is a survey of the Milky Way disk with the SEQUOIA multipixel array on the Five College Radio Astronomy Observatory 14 m telescope, and covers a longitude range of $18° < l < 55.7°$ and a latitude range of —b—¡1° with a spatial resolution of 46 arcsec.

2.3 Results

2.3.1 Region

Figure 2.1 shows the *Spitzer* three-color image of the region from $49.5° < l < 52°$. The overlaid contours show the molecular gas traced by ^{13}CO(1-0). The CO emission in all the panels is integrated within -5.0 km s^{-1} < v_{lsr} < 17.4 km s^{-1}. Several features can be identified. At $51.5° < l < 52.5°$, there is a bubble with a radius of $\sim 1°$ [G52L nebula, Bania et al., 2012]. The molecular gas is situated to the north of the bubble. At $51° < l < 52.5°$, the molecular gas is organized in the form of two molecular clouds (G052.24+00.74 and G051.69+00.74). The cloud G052.24+00.74 has a roundish shape.

---

[2]Note that Goodman et al. [2013] report a much larger length of "many hundreds of pc" for the Nessie nebula. See also http://milkywaybones.org/ for more details.
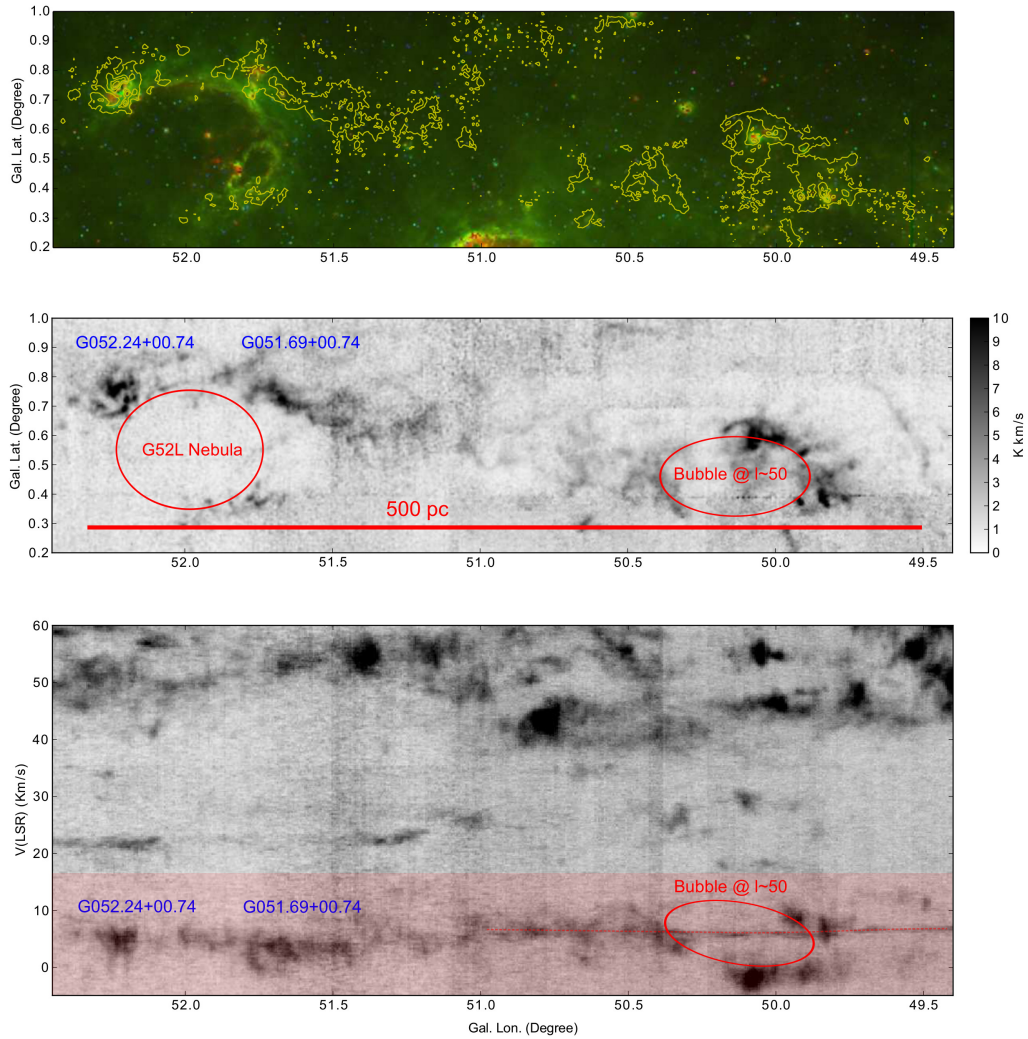
FIGURE 2.1: **Top panel:** Spitzer GLIMPSE [Benjamin et al., 2003] and MIPSGAL [Carey et al., 2009] three-color image of the region. Red: 24 μm, green: 8 μm, blue: 3.6 μm. Overlaid contours are the velocity-integrated ^{13}CO(1-0) emission (-5.0 km s^{-1} < v_{lsr} < 17.4 km s^{-1}) from the Galactic Ring Survey [Jackson et al., 2006]. Contours correspond to 3.5, 7.3, 11.2, 15 K km s^{-1}. **Middle panel:** Velocity-integrated ^{13}CO(1-0) map of the region integrated within -4.95 km s^{-1} < v_{lsr} < 17.36 km s^{-1}. A scale bar of 500 pc is added assuming a kinematic distance of 9.8 kpc. **Bottom panel:** Galactic-latitude-integrated ^{13}CO(1-0) position-velocity map of the region (integrated from $-0.2°$ < b < 1°). The clouds G052.24+00.74, G051.69+00.74, the bubble at $l \sim 50°$, and the G52L nebula [Bania et al., 2012] are indicated in the middle and bottom panels. The velocity range we used to produce the ^{13}CO(1-0) integrated intensity map is indicated in the bottom panel as the red shaded region. The emission at 5.2 km s^{-1} < v_{lsr} < 7.2 km s^{-1} is due to contamination from a different molecular cloud, and some of the emission lies on the red dashed line. This component has a smaller line width $\lesssim 0.5$ km s^{-1}, which implies that the contamination comes from a close-by cloud. This is supported by its apparent diffuse morphology. Channel maps of the region are provided in Appendix 2.6.1.

This cloud is connected with another molecular cloud, G051.69+00.74. This cloud has a more elongated geometry, and star formation occurs only at its eastern part.

At $49.5° < l < 50°$, there is noticeable contamination from gas with 5.2 km s^{-1} $< v_{\rm lsr} < 7.2$ km s^{-1} (see the red arrows in Fig. 3.6). The contaminating gas has an extremely narrow line width ($\lesssim 0.5$ km s^{-1}) and tends to spread along the spatial direction. This makes it easily distinguishable from the emission from the gas filament. This narrow line width implies that the emission comes from a close-by cloud. This is supported by the fact that the contaminating gas has a more diffuse morphology (see Appendix 2.6.1 for ^{13}CO(1-0) channel maps of the region). This distinction is similar to the supernova remnant G016.05-0.57 studied in Beaumont et al. [2011].

The two molecular clouds (G052.24+00.74 and G051.69+00.74) have a similar velocity and velocity dispersion: the cloud G052.24+00.74 has $v_{\rm lsr} \sim 4.6$ km s^{-1} and $\delta v \sim 2.6$ km s^{-1} and the cloud G051.69+00.74 has $v_{\rm lsr} \sim 3.6$ km s^{-1} and $\delta v \sim 3.6$ km s^{-1} [Roman-Duval et al., 2010]. In the position-position and position-velocity space, they are connected with some wispy gas filaments (at $l \sim 52°$ and $b \sim 0.8°$ of the top and middle panels of Fig. 2.1). The similarity of the velocity dispersions and the proximity of the clouds in position-velocity space imply that the two clouds are physically connected.

It can be readily seen from the ^{13}CO(1-0) emission that this double-cloud system belongs to a large filament (Fig. 2.1 and Appendix 2.6.1). The filamentary gas wisp is coherent in both the spatial and the velocity direction, which makes it distinguishable from other molecular structures, for instance the ~ 50 km s^{-1} clouds (Appendix 2.6.2). Seen from the middle panel of Fig. 2.1, the filamentary gas wisp extends from $l = 49.5°$ to $l = 52.5°$, which implies an angular extent of $\gtrsim 3°$. Seen from the bottom panel of Fig. 2.1, the filamentary gas wisp has a limited velocity range of ~ 22 km s^{-1} (-5.0 km s^{-1} $< v_{\rm lsr} < 17.4$ km s^{-1}). Similar to the double-cloud system, all the molecular gas in the filamentary gas wisp has a similar velocity dispersion. At $49.5° < l < 50.5°$, the filamentary gas wisp seems to be split in both the position-position and position-velocity maps (middle and bottom panels of Fig. 2.2). This coincides with the presence of a bubble in the infrared band. To summarize, the filamentary gas wisp is composed of two molecular clouds and one bubble.

Star formation occurs in different parts of the filamentary gas wisp. Star formation in molecular clouds can be conveniently traced by 24 μm emission, which originates from the dust heated by newly-born stars. In the *Spitzer* image, this appears as red regions (Fig. 2.1 top and Fig. 2.3). In the cloud pair G052.24+00.74 and G051.69+00.74, several star-forming sites can be identified (Fig. 2.3) based on the *Spitzer* 24 μm emission, three of which are currently hosting compact H II regions [Lockman, 1989, Urquhart et al.,
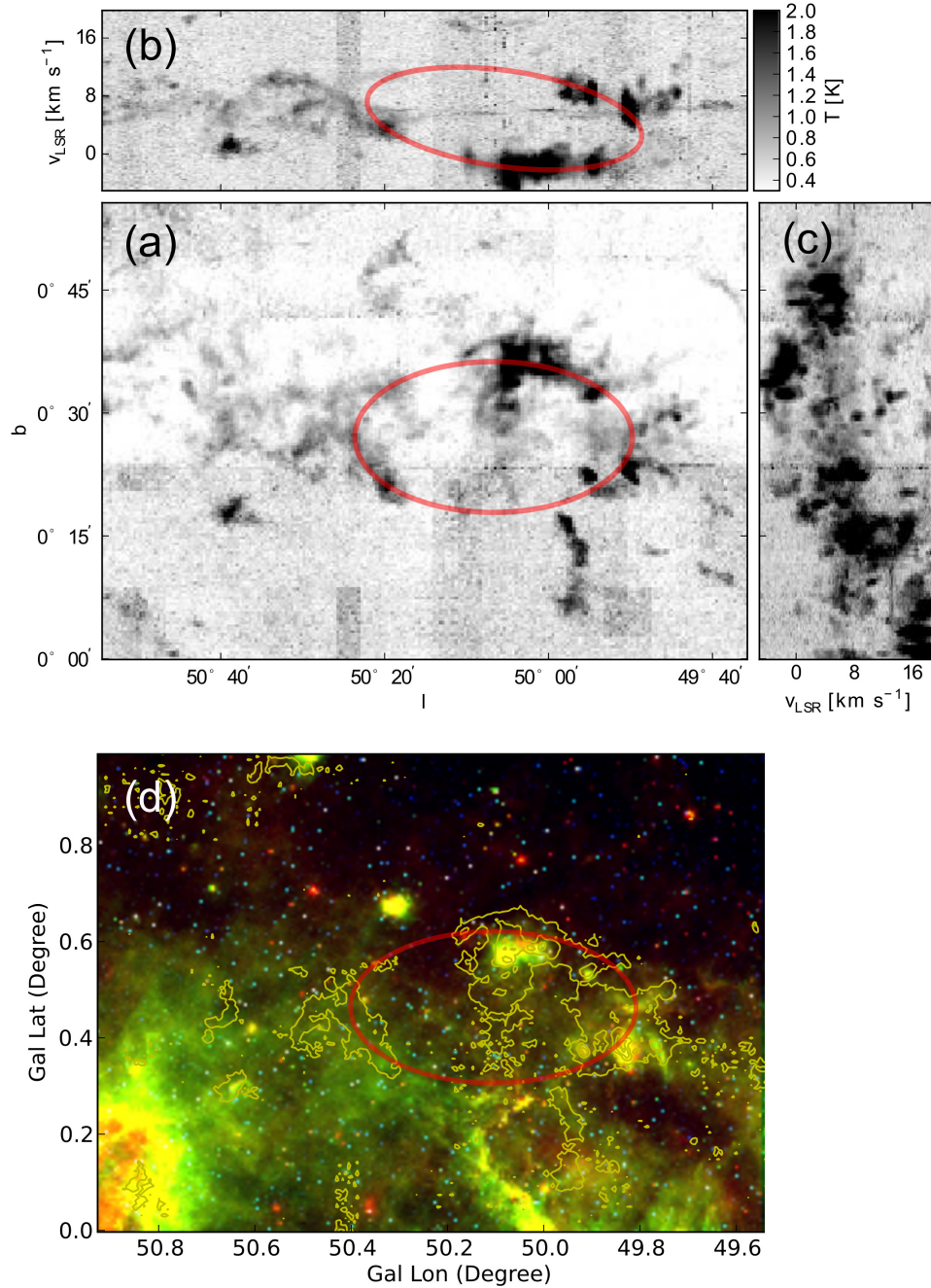
FIGURE 2.2: **(a)** Galactic longitude-latitude map of the peak temperatures of the ^{13}CO(1-0) data cube along the velocity axis. **(b)** Galactic-longitude-velocity map of peak temperatures of ^{13}CO(1-0) along the galactic latitude axis. **(c)** Velocity-galactic-latitude map of peak temperatures of ^{13}CO(1-0) along the galactic longitude axis. **(d)** Spitzer GLIMPSE [Benjamin et al., 2003] and MIPSGAL [Carey et al., 2009] three-color image of the region. Red: 24 μm, Green: 8 μm, Blue: 3.6 μm. Overlaid contours are the velocity-integrated ^{13}CO(1-0) emission from the Galactic Ring Survey [Jackson et al., 2006] (-4.95 km s$^{-1} < v_{lsr} < 17.36$ km s^{-1}). Contours correspond to 3.5, 7.3, 11.2, 15 K km s^{-1}. In **(a) (b)**, and **(d)**, the bubble is indicated as a red ellipse.

2009]. At $51.5° < l < 52.5°$, all the star-forming sites are located at the edge of the G52L bubble.

2.3.2 Distance and size of the filament

The distance to the region has been estimated by several authors. Without trigonometric parallaxes, the distance to the region can be determined with the kinematic method. One key step in determining the kinematic distance is to resolve the kinematic distance ambiguity.

There are different ways to resolve the ambiguity. Distance of the filamentary gas wisp can be determined by studying the distance to molecular clouds and H II regions that belong to the filament. Using HI self-absorption, Roman-Duval et al. [2010] found that the molecular clouds G052.24+00.74 and G051.69+00.74 are located at the far distance. Using the H_2CO absorption line, Watson et al. [2003] found that the H II region G52.23+0.74 is located at the far distance. Recently, Anderson & Bania [2009] and Bania et al. [2012] studied the distance to the H II regions G052.201+0.752 and G052.259+0.700 with HI emission/absorption method, and again found that they are at the far distance. Therefore we conclude that the filamentary gas wisp is located at the far distance, which is approximately 9.8 kpc. This suggests a galactocentric distance of 8.2 kpc, and the filamentary gas wisp probably resides in or around the Perseus arm.

Accordingly, the filamentary gas wisp we identified has a spatial extent of ~ 500 pc. If the filamentary gas wisp follows the spiral structure, it is probably angled $\sim 45°$ to our line of sight, and therefore probably has a deprojected length a factor of $\sqrt{2}$ longer. Therefore we conclude that the filamentary gas wisp has a length of $\gtrsim 500$ pc. It is one the of the largest coherent molecular structures in the Milky Way apart from the spiral arms and the molecular ring. The total mass of the filamentary gas wisp can be estimated using the $^{13}CO(1-0)$ emission. To do this, we integrated over the region with the line-of-sight integrated flux $I > 3.5$ K km s^{-1}. This corresponds to the first contour in the upper panel of Fig. 2.1. This mass estimate should be considered as a lower limit since by selecting this threshold we only take the region with a high column density ($N_{H_2} > 1.75 \times 10^{21}$ cm^{-2}) into account. Using Eq. 1–3 of Roman-Duval et al. [2010] and assuming an excitation temperature of 10 K, we obtain a total mass of $\sim 1 \times 10^5 M_\odot$ for the whole gas wisp ($49.5° < l < 52.5°$). According to Simon et al. [2001], the derived mass is only weakly sensitive to this choice of excitation temperature, and in our case an excitation temperature of 20 K gives a mass of $\sim 0.6 \times 10^5 M_\odot$.

The two clouds at the eastern part of the filamentary gas wisp have $b \sim 0.74°$. Using a kinematic distance of 9.77 kpc, the double-cloud system is ~ 130 pc above the Galactic

plane. At a Galactocentric distance of ~ 8 kpc, the molecular disk of the Milky Way has a FWHM thickness of $90 - 180$ pc [at 7–8 kpc the FWHM is ~ 90 pc and at 8–9 kpc the FWHM is 186 pc, Nakanishi & Sofue, 2006]. This corresponds to an e-folding height of 38–80 pc. Therefore the height of the double-cloud system is about 1.5–4 times the e-folding height of the Galactic disk. The double-cloud system is a unique cloud system that is located far above the Galactic plane. According to Bania et al. [2012], one possible explanation is that the material of the system has been displaced by the expansion of the G52L nebula.

2.3.3 The bubble structure at $l \sim 50$

Figure 2.2 shows the bubble structure at $l \sim 50°$. Its boundary is visible in both the 8 μm emission, which traces polycyclic aromatic hydrocarbon (PAHs) and in the ^{13}CO(1-0) emission. The bubble is not easily visible at 24 μm, which traces hot dust heated by a central star. Because of the apparent absence of the 24 μm emission, the bubble structure does not seem to be driven by the expansion of a H II region. This is also supported by the absence of a diffuse H II region in the VGPS [Stil et al., 2006] continuum image.

It is more likely that the bubble structure is driven by the expansion of a supernova. The *Spitzer* image of the bubble resembles that of several supernova remnants in the Churchwell et al. [2006] catalog. From panel (a) of Fig. 2.2, using the kinematic distance of 9.8 kpc, we estimate a diameter of $1° \sim 180$ pc, and from panel (b) of Fig. 2.2 we estimate a total expansion velocity of 10 km s^{-1}. These give an age of 50 Myr. The energy of a possible supernova explosion can be estimated through the Sedov-Taylor solution: $E \sim r^3 v^2 \rho \sim 0.16 \times 10^{51}$ erg. The energy is consistent with a supernova explosion. Here, a density of 10^{-24} g cm^{-3} is used, which is typical of warm neutral medium [cf. Bocchino et al., 2010].

2.4 Discussion

2.4.1 Morphology of the filamentary gas wisp

This giant molecular structure is among the largest molecular structures studied in the Milky Way ($\gtrsim 500$ pc). The physical size of the gas filamentary gas wisp is much larger than that of a typical molecular cloud [~ 10 pc, Roman-Duval et al., 2010]. The velocity dispersion along a single line of sight in the filamentary gas wisp is not significantly different from that of ordinary molecular clouds.

The molecular gas in the filamentary gas wisp is concentrated in the vertical (Galactic-latitude) direction and elongated along the horizontal (Galactic-longitude) direction. At different locations, the filamentary gas wisp exhibits a different width. At $49.5° < l < 50.5°$, the filamentary gas wisp is split in the map, which makes it difficult to define its width. From the map, the cloud G052.24+00.74 appears to be more extended in the vertical direction than the cloud G051.69+00.74. We therefore used its vertical extent as an estimate of the width of the filamentary gas wisp. The vertical extent of the cloud G051.69+00.74 is measured for the region with $I > 3.5$ K km s^{-1} ($N_{H_2} > 1.75 \times 10^{21}$ cm^{-2}). This corresponds to the first contour in the upper panel of Fig. 2.1. We found that the cloud extends from $b \sim 0.65°$ to $b \sim 0.82°$. From this we estimated a diameter of 30 pc, which implies an aspect ratio of $\sim 600/30 = 20$ for the gas wisp. The gas wisp is one of the most elongated molecular structures found in the Milky Way [see also the Nessie nebula, Jackson et al., 2010]. The width of the filamentary gas wisp is narrower than the FWHM thickness of the molecular disk of the Milky Way, which is about 90–180 pc [Nakanishi & Sofue, 2006] at a Galactocentric distance of ~ 8 kpc.

Similar large-scale molecular structures have been observed in other galaxies. In spiral galaxies, elongated gas condensations are frequently observed. They can be seen as narrow dark lanes that extend perpendicular to the spiral arms [Lynds, 1970, Weaver, 1970]. The exact definitions of dust lanes or spurs differ in the literature. However, in most cases spurs refer to the objects whose widths are similar to that of spiral arms [Elmegreen, 1980]. In our case, the filamentary gas wisp should not be termed a spur because its width is narrower than the width of the spiral arms of a typical galaxy, which is ~ 500 pc [Egusa et al., 2011].

In our case, the filamentary gas wisp is about one or two orders of magnitudes longer than ordinary molecular clouds, but is still much narrower than the spurs in galaxies. Therefore we propose that the filamentary gas wisp is a new object that is yet to be classified. Because of this, we termed it a gas wisp in this work to emphasize its elongated morphology.

Even though the thickness of the filamentary gas wisp is similar to the resolution of the PAWS survey [Schinnerer et al., 2013] of M51, filamentary gas wisps of this size would not be detected. This is because the survey is only sensitive to objects with a mass $\gtrsim 1.2 \times 10^5 M_\odot$ and the clouds in the filamentary gas wisp are only $\sim 10^4 M_\odot$. However, similar large-scale gas structures in nearby galaxies are probably suitable targets for ALMA thanks to its improved sensitivity. Nearby face-on galaxies are expected to be excellent sites for studying these gas wisps since line-of-sight confusion can be avoided. A future project at ALMA targeting at the molecular gas in nearby face-on galaxies is

expected to resolve similar gas condensations and provide a more complete picture of the structure of molecular gas in galaxies.

2.4.2 Implications for the formation of molecular clouds

The formation and evolution of molecular clouds is one of the fundamental problems in interstellar medium studies. To account for the short formation timescale of molecular clouds, two scenarios have been proposed. The first scenario involves colliding flows. In this scenario, molecular clouds form from diffuse gas (warm neutral medium) collected into a dense phase (cold neutral medium/molecular medium) through colliding flows [Audit & Hennebelle, 2005, Heitsch et al., 2006, Vázquez-Semadeni et al., 2007, 2010, Inoue & Inutsuka, 2012]. The molecular gas can form quickly in the converging flows because of dynamically-triggered thermal instability.

The second scenario has been proposed by Pringle et al. [2001] and Dobbs & Pringle [2013]. In this scenario, the gas is already relatively dense and cold prior to becoming a giant molecular cloud. According to Pringle et al. [2001], there is expected to be copious cold gas in the inter-arm regions since the circulation of the molecular gas is a process that occurs at the disk scale. To describe the global circulation of the gas, we divided it into the in-arm phase in which the gas is situated inside the spiral arms, and the inter-arm phase in which the gas is situated in the inter-arm regions. As discussed in Pringle et al. [2001], in the inter-arm phase, the cold gas exists in the form of wisps, and the gas in these wisps will show up as giant molecular clouds during the spiral-arm phase. This has been largely confirmed by the simulations of Dobbs & Pringle [2013], which track the evolution of single molecular clouds. These authors found that molecular clouds begin to disperse as they leave the spiral arm. Due to differential shear, the molecular clouds are transformed into filamentary gas wisps in the inter-arm region. Since the shear occurs at a large scale, we expect to see gas wisps whose physical scale exceeds the thickness of the Milky Way disk. In our case, the physical length of the filamentary gas wisp ($\gtrsim 500$ pc) is much larger than the scale-height of the Milky Way molecular disk. This is consistent with the cloud-formation scenario by Pringle et al. [2001] and Dobbs & Pringle [2013]. Such large-scale structures are also observed in other numerical simulations of galactic disks [Tan, 2000, Kim & Ostriker, 2002, Dobbs & Bonnell, 2006, Dobbs et al., 2006, Shetty & Ostriker, 2006, Tasker & Tan, 2009, Ceverino et al., 2012].

On the other hand, it is difficult to understand the filamentary gas wisp in the converging flow scenario. In this scenario, molecular gas forms from the converging HI gas through the dynamically-triggered thermal instability. As summarized in Dobbs et al. [2012], the sources of the converging flows can be stellar winds or supernovae [Koyama & Inutsuka,
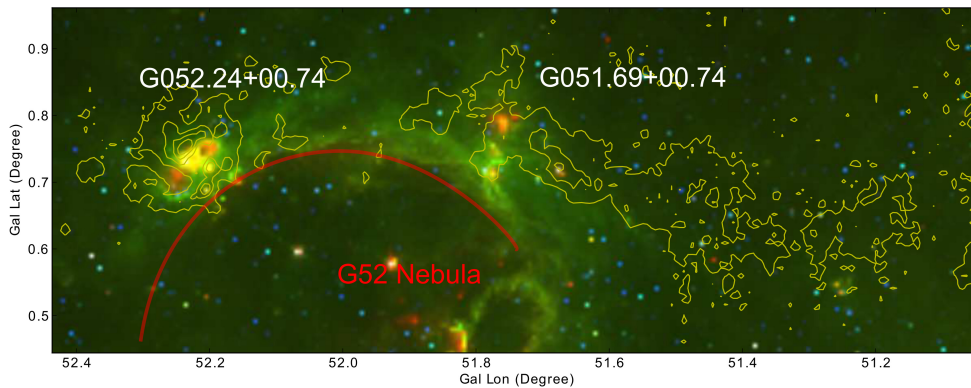
FIGURE 2.3: Spitzer GLIMPSE [Benjamin et al., 2003] and MIPSGAL three-color image of the clouds G052.24+00.74 and G51.69+00.74. Red: 24 μm, green: 8 μm, blue: 3.6 μm. Overlaid contours are the velocity-integrated ^{13}CO(1-0) emission $(-4.95$ km s^{-1} $< v_{\mathrm{lsr}} < 17.36$ km s$^{-1})$ from the Galactic Ring Survey [Jackson et al., 2006]. Contours correspond to 3.5, 7.3, 11.2, 15 K km s^{-1}. The cloud G052.24+00.74 and G51.69+00.74 as well as the G52L nebula are indicated.

2000, Heitsch & Hartmann, 2008, Ntormousi & Burkert, 2011], turbulence in the interstellar medium [Ballesteros-Paredes et al., 1999], spiral shocks [Leisawitz & Bash, 1982], and gravitational instability. In our case, the filamentary gas wisp cannot be created by converging stellar winds, supernovae, or turbulence in the interstellar medium, since these mechanisms are local and cannot create structures that are larger than the thickness of the Milky Way disk. Spiral shocks and gravitational instability might create conditions favorable for converging flows to occur. However, to access these possibilities we need to simulate converging flows in a galactic context and properly quantify the role of the dynamically-triggered thermal instability in the formation of molecular gas. This task has not been achieved yet. Either the converging flow scenario is unable to explain how filamentary gas wisps form, or our current understanding of converging flows in a galactic context is incomplete.

2.4.3 Star formation in the molecular cloud pair G0524.2+00.74 and G051.69+00.74

It is unclear to what extent molecular clouds are gravitationally bound. Gravity is important at a variety of physical scales during star formation. According to Roman-Duval et al. [2010], the clouds G052.24+00.74 and G051.69+00.74 have virial parameters of 0.29 and 0.33, respectively. This means that both clouds are gravitationally bound [3].

---

[3] Here and in Roman-Duval et al. [2010] the virial parameter α of a molecular cloud is the ratio of its virial mass M_{vir} to its mass.
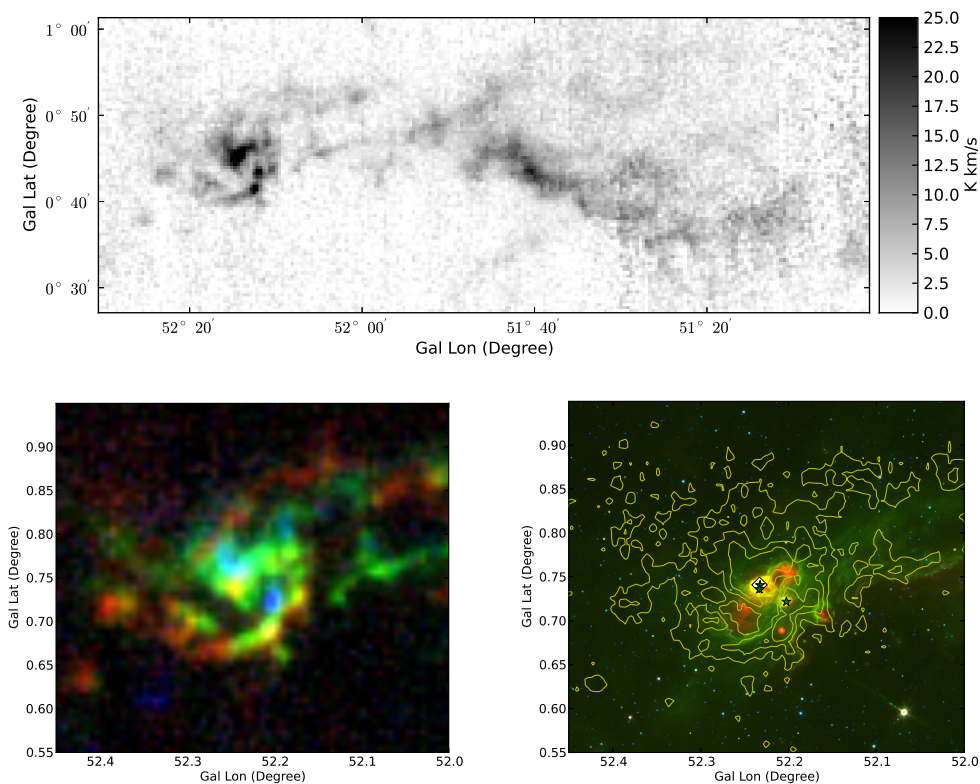
FIGURE 2.4: **Upper qpanel:** ^{13}CO(1-0) emission integrated from -4.5 to 15.0 km s^{-1} from the GRS survey [Jackson et al., 2006]. The cloud G052.24+00.74 is at the left side. This cloud is connected with a neighbouring cloud G051.69+00.74 by some filamentary gas wisps. A channel map of the region can be found in §2.6.1. **Lower left panel:** Composite 3-color image of the ^{13}CO(1-0) emission from the Spiral Cloud G052.24+00.74. Red: $6.52 < v_{lsr} < 15.02$ km s^{-1} Green: $3.12 < v_{lsr} < 6.10$ km s^{-1} Blue: $-4.53 < v_{lsr} < 2.7$ km s^{-1}. **Lower right panel:** Spitzer GLIMPSE [Benjamin et al., 2003] and MPISGAL 3-color image of the Spiral Cloud G052.24+00.74. Red: 24 μm, Green: 8 μm, Red: 3.6 μm. Overlaid contours are the velocity-integrated ^{13}CO(1-0) emission. Contours correspond to 5, 10, 15 K km s^{-1}. The white diamond in the center stands for a star cluster discovered in the GLIMPSE survey [Mercer et al., 2005], and the green stars stand for H II regions [Lockman, 1989, Urquhart et al., 2009].

Star formation takes place in several sites, which is traced by the 24 μm emission in the *Spitzer* image. As indicated in Fig. 2.3, all these sites seem to be located at the edge of a bubble (G52L nebula).

The connection between the location of the star-forming sites and the edge of the bubble agrees with the statistical study of Thompson et al. [2012], in which a significant overdensity of young stellar objects toward the edges of the bubbles was found. This is consistent with the collect-and-collapse scenario of triggered star formation [Elmegreen & Lada, 1977, Whitworth et al., 1994].

2.4.4   The spiral-shaped molecular cloud G052.24+00.74

Figure 2.4 shows the structure of the cloud. Seen from ^{13}CO emission from the GRS survey [Jackson et al., 2006], the cloud exhibit a spiral-shaped morphology, with two "spiral arms" extend from the central part of the cloud. Each of the "spiral arm" is composed of several clumps. The ^{13}CO emission from the cloud also exhibit a clear velocity gradient: gas at the south-east part tends to be red-shifted and gas at the north-wast part of the cloud tends to be blue-shifted. Wisps of molecular gas connect the cloud with another cloud at $l \sim 51°$ (G051.69+00.74).

We use *dendrogram* [Rosolowsky et al., 2008, Goodman et al., 2009] [4] to quantify the clumpy structure of the cloud. The dendrograms are representations of how the iso-surfaces in the 3-D PPV(position-position-velocity) data cube nest inside one another. The "Leaves" of the dendrogram correspond to the regions that have emission enhancements in the 3-D PPV data cube, and are correspondent to the "clumps" found by the well-known *clumpfind* algorithm [Williams et al., 1994]. One advantage of using dendrogram is that its results are less dependent on technical parameters (for instance, the brightness temperature difference between contours). In this work, the term *cloud* is used to refer to the whole cloud G052.24+00.74, and the term *clump* is used to refer to the sub-structures of the cloud found by the *dendrogram* algorithm.

In Figure 2.5 we plot the leaves of the dendrogram. IDs of the leaves are also plotted. We divide the leaves (clumps) into different groups. First, we make a distinction between the clumps inside the "spiral arm" and the clumps outside the "spiral arm". Second, since three of the clumps (clump 18,19 and 22) show evidences for star formation (inside clump 22, a star cluster has already formed, and massive stars inside this star cluster are probably triggering the formation of a next generation of stars. A bubble is found in clump 18. RMS YSOs are found in clump 19 [Thompson et al., 2012] , we separated them from the rest of the clumps. Finally, we have three groups of clumps. The first group include the clumps that exhibit obvious star formation activities (clump 18, 19 and 22), the second group include the other clumps that are inside the "spiral arm", and the third group consists of the rest of the clumps.

We analyse the physical properties of the three different groups of clumps. In deriving the properties of the clumps, we assume a kinematic distance of 9.77 kpc [Roman-Duval et al., 2010], and use the same formalism as used in Goodman et al. [2009]. In Fig. 2.6, we plot $\sigma_{\rm v}^2/R$ versus Σ for all the clumps [Simon et al., 2001]. These two quantities are related to the viral parameter of the clump through [Bertoldi & McKee, 1992, where

---

[4]We use *astrodendro*, which is available at https://github.com/astrofrog/astrodendro

$\Sigma \equiv M/\pi R^2$]

$$\alpha_{\rm vir} = \frac{5\sigma_{\rm v}^2 R}{GM} \ , \tag{2.1}$$

where $\alpha_{\rm vir}$ is the viral parameter, $\sigma_{\rm v}$ is the velocity dispersion of the clump, R is the radius of the clumps, G is gravitational constant, and M is the mass clump. Lines with $\alpha_{\rm vir} = 0.5, 1, 2$ are included. The clumps that belong to the spiral arm are close to gravitationally bound ($0.5 < \alpha_{\rm vir} < 1$), while the other clumps are not. Interestingly, all the three clumps that show star formation activity have $\alpha_{\rm vir} \sim 0.5$.

The relation between the smallness of the viral parameter and the star formation activities leads us to suggest that the star formation inside the clumps is controlled largely by self-gravity. This can also be verified by looking at the free-fall timescales of the clumps. The characteristic timescale that governs the gravitational collapse of the clumps is the free-fall timescale, which is defined as $t_{\rm ff} \sim (G\rho)^{-1/2}$, $\rho \equiv M/R^3$. In Figure 2.7 we plot the mass of the clumps as function of the radii of the clumps. Lines that correspond to different free-fall timescale $t_{\rm ff}$ are added. The clumps that belongs to the spiral arm have significantly shorter free-fall timescale, and the three clumps that are forming stars have not only short free-fall timescale but also higher mass.

A star cluster is formed at the center of clump 22 [Mercer et al., 2005]. This clump is distinguished in two ways. First, it is the clump that resides right at the center of the spiral structure. Second, compared to all the other clumps, it has the smallest viral parameter and the shortest free-fall timescale.

2.5 Conclusions

We studied a giant coherent molecular structure (a filamentary gas wisp) at $49.5° < l < 52.5°$. The eastern part of the filamentary gas wisp is located ~ 130 pc above the Galactic disk (which corresponds to 1.5–4 e-folding scale-heights), and the total mass of the gas wisp is $\gtrsim 1 \times 10^5 M_\odot$. Apart from the spiral arms and the molecular ring, this is among the largest coherent molecular structures identified in the Milky Way. The velocity structure of the filamentary gas wisp is coherent and smooth at $50.5° < l < 52.5°$, and at $49.5° < l < 50.5°$, the gas wisp is disturbed by a bubble structure. This might be caused by a supernova. The overall velocity structure of the filamentary gas wisp can be understood as a quiescent filamentary gas wisp disturbed by the expansion of a bubble. The eastern part of the filamentary gas wisp is composed of a system of two molecular clouds (G052.24+00.74 and G051.69+00.74) and is located ~ 130 pc above the Galactic plane.
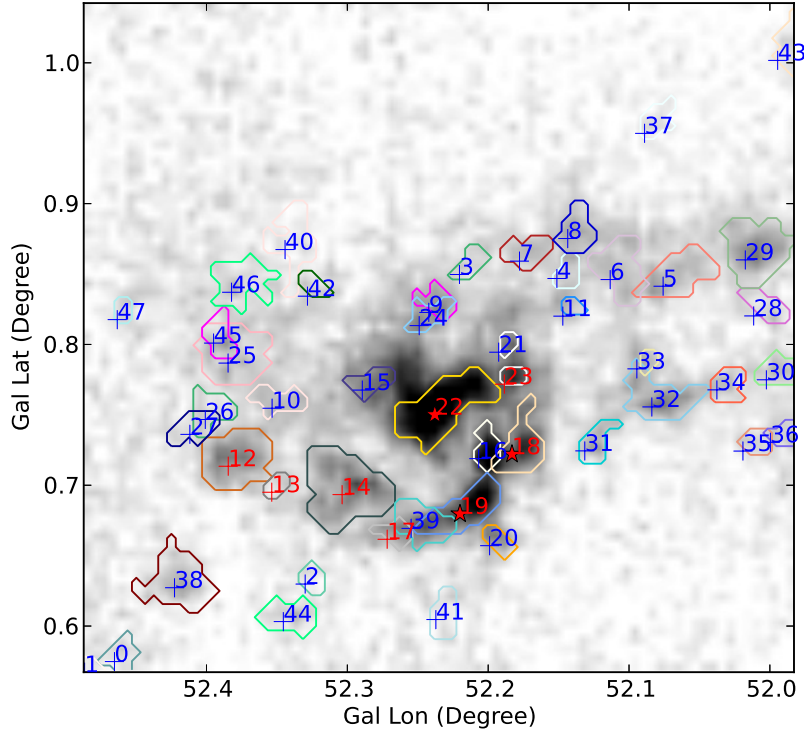
FIGURE 2.5: Clumps (leaves) found our by the dendrogram method. Here we use different colors to stand for different leaves for clarity. Each leaf have a unique ID. We divide the leaves into three groups, one group contains the clumps that belong to the "spiral arm" of the cloud (red numbers), and the other group contain the clumps that are outside the "spiral arm" (blue numbers). The third group contains the clumps 18,19 and 22, which exhibit clear evidences of ongoing star formation (red stars).

Star formation already takes place in several parts of this filamentary gas wisp. In the cloud pair G052.24+00.74 and G051.69+00.74, nearly the entire star formation occurs at the edge of a bubble [G52L nebula, Bania et al., 2012]. This is consistent with the collect-and-collapse scenario of triggered star formation [Elmegreen & Lada, 1977, Whitworth et al., 1994], and can be understood in the statistical context of Thompson et al. [2012].

The discovery of this filamentary gas wisp, whose length exceeds the thickness of the molecular disk of the Milky Way, suggests that the formation and evolution of molecular clouds is a phenomenon that occurs at the disk scale. The large physical extent is consistent with the cloud-formation scenario by Pringle et al. [2001] and Dobbs & Pringle [2013], in which the gas that constitutes the molecular clouds is already relatively cold prior to the cloud formation.

We are currently unable to answer how representative this filamentary gas wisp is in the Milky Way disk. One reason is that we are restricted by the line-of-sight confusion,
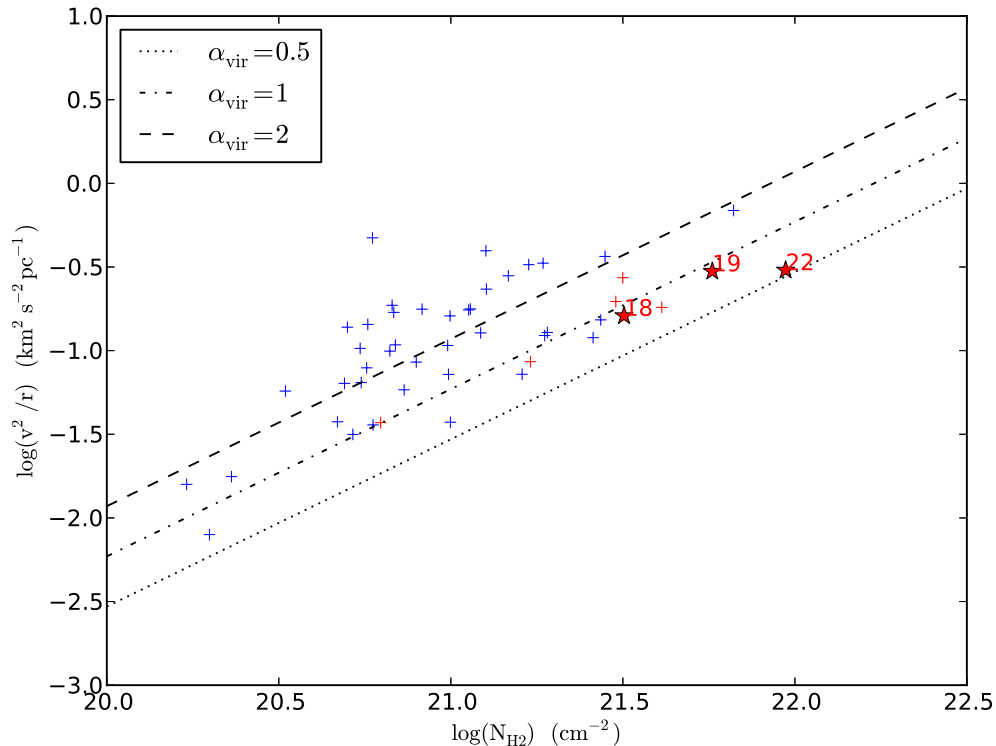
FIGURE 2.6: Ratio of σ_v^2/R as a function of clump column density N_{H_2}. We divide the leaves into three groups, one group contains the clumps that belong to the "spiral arm" of the cloud (red crosses), and the other group contain the clumps that are outside the "spiral arm" (blue crosses). The third group contains clump 18,19 and 22, which exhibit clear evidences of ongoing star formation (red stars with numbers). Lines of different virial parameters $\alpha_{vir} = 5\sigma_v^2 R/G\Sigma$ are included.

and the filamentary gas wisp is fragile in nature. In our case, at $49.5° < l < 50.5°$, the filamentary gas wisp is already being destroyed by the expansion of a bubble structure. It is possible that a significant fraction of the gas in the Milky Way exists in this form during at least part of its lifetime. Another difficulty is to properly quantify the coherence of molecular structures beyond the cloud scale. A position-velocity plot of the $^{13}CO(1-0)$ data from the same region shown in the bottom panel of Fig. 2.1 reveals filamentary structures at $v_{lsr} \sim 50$ km s^{-1}. From a visual inspection we found that these structures are not as coherent as the filamentary gas wisp (see Appendix 2.6.2 for a comparison). In general one cannot yet quantify the coherence of molecular structures in the Milky Way. More studies of the morphology of the molecular gas in both the Milky Way and other galaxies with improved observations and analyses are needed to fully understand the circulation of molecular gas at large scales.
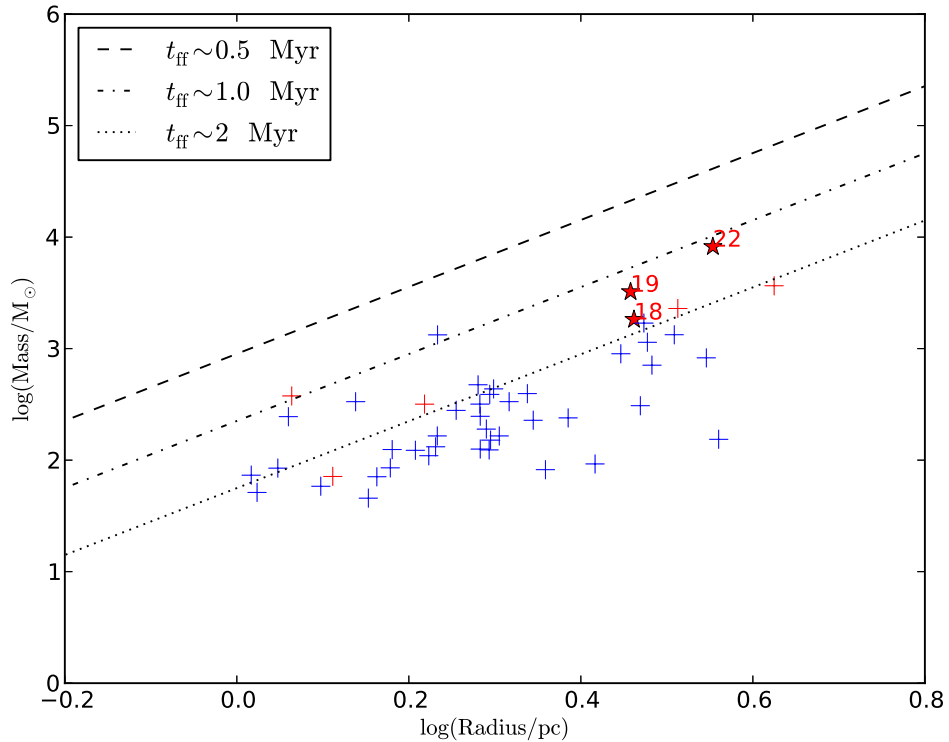
FIGURE 2.7: Clump mass versus clump radius for all the clumps. We divide the leaf into three groups, one group contains the clumps that belong to the "spiral arm" of the cloud (red crosses), and the other group contain the clouds that are outside the "spiral arm" (blue crosses). The third group contains clumps 18,19 and 22, which exhibit clear evidences of ongoing star formation (red stars with numbers). Lines of different free-fall timescale $t_{\rm ff} \sim \rho^{-1/2}$ are included.

2.6 Appendix

2.6.1 Channel map of the filamentary gas wisp

In Fig. 3.6 we present the channel maps of the ^{13}CO(1-0) emission from the GRS [Jackson et al., 2006] survey. Some contamination from local clouds is indicated.

2.6.2 A comparison with CO emission from the 50 km/s component

To demonstrate the coherence of our filamentary gas wisp, in Fig. 2.9 we present a map of the same region with the velocity integrated within 29.5 km s^{-1} < $v_{\rm lsr}$ < 73.3 km s^{-1}. Seen from the ^{13}CO(1-0) emission, this component is composed of individual patches of molecular clouds and is not as coherent as our filamentary gas wisp. The distance to the region is $\sim$ 5.3 kpc.
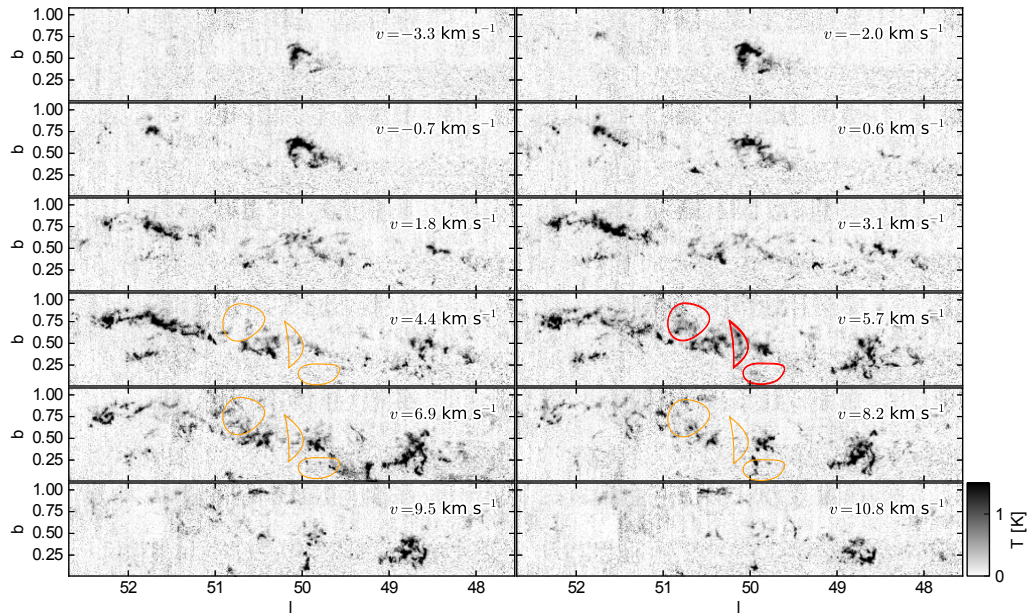
FIGURE 2.8: Channel maps of the GRS [Jackson et al., 2006] ^{13}CO(1-0) emission of the region. The contaminating gas has a narrow ($\sim$ 0.5 km s^{-1}) line width, and is detected only in single channels in the map. Some contamination from local clouds is indicated with red circles as examples, and these red circles are also plotted in yellow in the adjacent velocity channels for comparison.
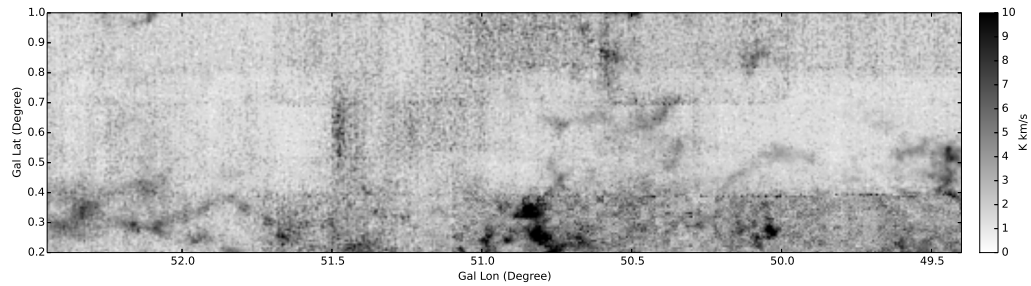
FIGURE 2.9: Velocity-integrated ^{13}CO(1-0) map of the $\sim$ 50 km s^{-1} clouds. The emission is from the same region as shown in Fig. 2.1 and is integrated within 29.5 km s^{-1} < v_{lsr} < 73.3 km s^{-1}.

2.7 Acknowledgements

Chapter 3

G-virial: a general method to quantifying gravity in molecular clouds [1]

3.1 Introduction

Star formation takes place in the dense and shielded parts of the interstellar medium. Observations show that the interstellar medium exhibits complicated, irregular and filamentary structures [Schneider & Elmegreen, 1979, Williams et al., 2000, Goldsmith et al., 2008, Men'shchikov et al., 2010]. Theoretically such structures are created by various physical processes such as turbulence, gravity, magnetic field and radiation.

To understand star formation it is necessary to understand how various physical processes affect it. Gravity is a long-range interaction, and plays important roles in the majority of astrophysical processes that occur at various physical scales. This is in particular true for turbulent molecular clouds in which star formation takes place [e.g. Heyer et al., 2009, Kauffmann et al., 2013]. However, it is not straight-forward to characterize the role of gravity on a cloud as a whole or its parts.

In observations, the structure of molecular gas can be traced by spectral lines in the 3D position-position-velocity space. The analyzed molecular clouds exhibit rich and complicated structures. However few constraints on the role of gravity in the clouds have been obtained so far. One major difficulty is to properly quantify the irregular structure of the gas. The virial parameter $\alpha_{\mathrm{vir}} = 5\sigma^2 R/GM$ [2] is commonly used to

---

[1]This chapter has been submitted to A&A as "G-virial: A general method to quantify gravity in molecular clouds", Li, G.-X, Wyrowski, F., Megeath, T., Menten, K. Shi, X.

[2]Here σ is the velocity dispersion and M is the mass [Bertoldi & McKee, 1992].

quantify the importance of gravity in the clouds, and to calculate it, we must define a region on which σ and M can be evaluated. As a result, the virial parameter is only suitable for the cases where the structures are well-defined. The morphology of the interstellar medium is so complicated that sometimes it is difficult to separate the individual objects from a continuous distribution of material.

Another difficulty with the virial parameter is that it is *localized*. To define the virial parameter we need to define the region, and by evaluating the virial parameter of that region, we automatically neglect the gravitational interaction between the region and its surroundings. As a result, the virial parameter can be used to quantify the importance of gravity for the individual structures, but it can not be used to understand the importance of gravity for a cloud as a whole. Gravity is a *long-range* interaction, and to understand its importance, we need to understand how it works outside the individual regions.

For instance, in observations, cluster-forming regions are found to be centrally-condensed in both the position-position space and the position-position-velocity space, and physically we expect that gravity is important at the centers of the cluster-forming regions and should become less important if we move from the centers to the outskirts. This stratified structure, which is of crucial importance for understanding stellar clustering, awaits to be quantified.

To understand the *global* importance of gravity, it is necessary to go beyond the individual regions, and quantify its importance at a varieties of physical scales. One way of achieving this is through the `dendrogram` [Rosolowsky et al., 2008] method, which decomposes the cloud into a set of nested structures and the study of gravity can be carried out based on these structures. However the `dendrogram` method is still incomplete. The method is still contour-based, and only the gravitational interactions between neighbouring regions are taken into account [e.g. Goodman et al., 2009]. As a result, this method is appropriate for the estimation of the importance of self-gravity, but is not sufficient to provide understandings on the importance of gravity on the cloud as a whole.

There are several other situations where an understanding of gravity is important, such as the evolution of giant molecular complexes in the Milky Way [**?**]. In this paper we introduce a new method named `G-virial` to quantify gravity in a variety of situations where mass is traced in the 3D position-position-velocity space. The method provides constraint on the *global* importance of gravity, and is complimentary to other methods which calculate the self-gravity such as the virial parameter method and the `dendrogram` method. Combined with methods such as the `dendrogram`, it enables us to identify gravitationally coherent regions in molecular clouds. The `G-virial` maps can be easily combined with the original data and enables derivations of relations such as mass-size

and velocity-size relation. In this paper we introduce our method, and provide sample applications to the Perseus and Ophiuchus molecular clouds which have been mapped in the COMPLETE survey [Ridge et al., 2006].

A related question is to understand the structure of the observed and simulated gas condensations. Currently, the structures of the gas condensations are quantified either by decomposing them into clumps or by studying the structure of the corresponding `dendrogram`. Through decomposing into clumps, we automatically ignore the structure of the gas condensations beyond the clump scale. A `dendrogram` can be potentially used to quantify structure of molecular gas at various scales. However, it remains to be discussed what should taken as the input of the `dendrogram` and what quantities should be evaluated on the resulting tree structure. Another difficulty is that the resulting tree structure in the `dendrogram` is relatively complicated, and is not straight-froward to use. In this paper, we explore the use of the `G-virial` to quantify the structures of the molecular condensations seen in observations and simulations.

3.2   Problem formulation

Observationally, molecular gas can be mapped by rotational transitions of molecules such as CO. Through proper modelling of the emission, it is possible to construct the distribution of the molecular gas in the form of a 3D position-position-velocity data cube which covers a continuous (x, y, v) space

$$m(x, y, v) = \rho(x, y, v) \, \mathrm{d}x \, \mathrm{d}y \, \mathrm{d}v \,, \tag{3.1}$$

where m represents the mass, x and y represent the spatial dimensions and v represents the velocity dimension. Here ρ has a dimension of $[M \, L^{-3} T]$, and represents the amount of mass per unit area per unit velocity. The distribution of ρ in the v dimension represents the distribution of gas at different velocities along the same line of sight.

We start with a mass distribution in a 3D position-position-velocity data cube (Fig. 3.1). We aim to understand how is a particle at pixel i bounded by mass from all the other pixels j. To achieve this, we split our task into two sub-tasks. First, we need to estimate the boundedness of pixel i by another pixel j in the 3D position-position-velocity data cube. Second, we need to estimate the gravitational boundedness of a pixel i based on the information we have about all the other pixels j.
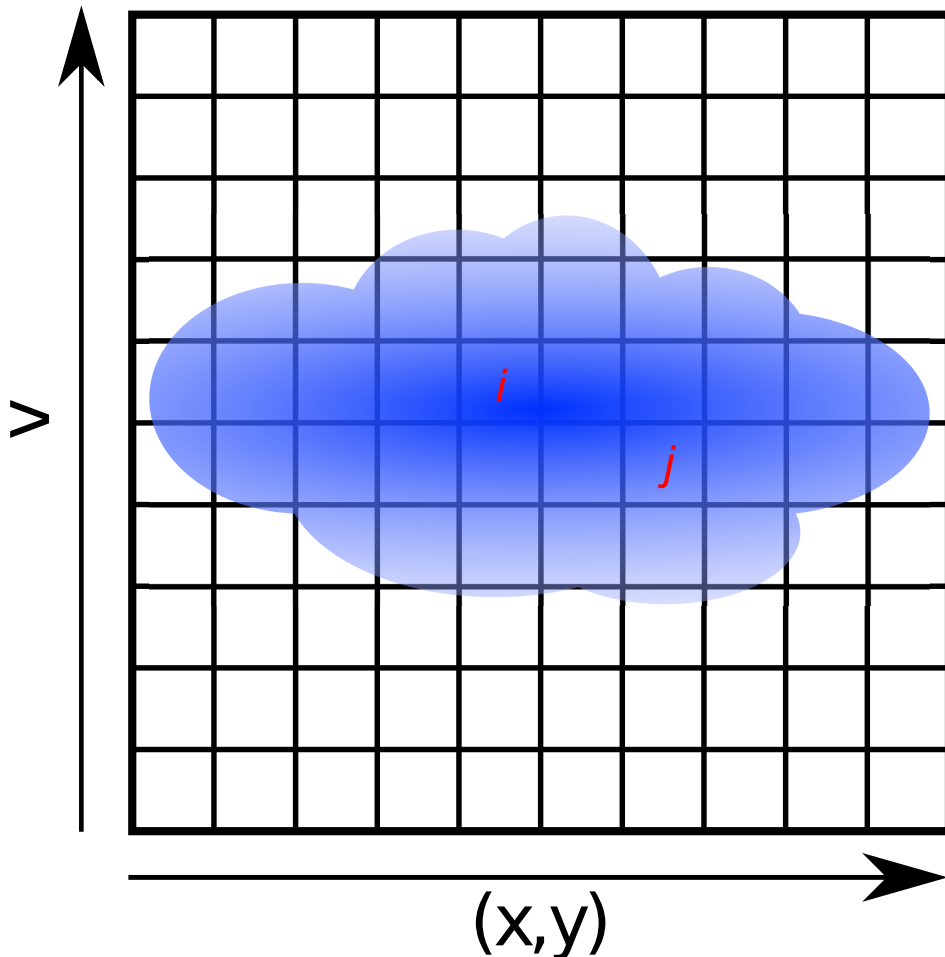
FIGURE 3.1: Illustration of the setup of of the problem. We consider a mass distribution in the 3D position-position-velocity data cube. This is represented as the black grid. x–y represents the spatial dimensions and v represent the velocity dimension. The mass distribution is represented in blue. For each pixel i, its `G-virial` can be determined by taking its interactions with all the other pixels j into account. See Sec. 3.2 for the details.

3.2.1   Boundedness a pixel pair in 3D data cubes

We start by defining the boundedness between a pair of pixels (i, j). We are interested in to what extent a particle i is bounded to another pixel j, and as a result, i is a mass-less test particle, and the boundedness of particle i is determined by the mass of the pixel j.

The available measurable quantities in the 3D position-position-velocity data cube include the mass m_j, the spatial separation δr_{ij} and the velocity separation δv_{ij}. We expect the boundedness should increase with m_j, and decrease with δr_{ij} since gravitational attraction increases with the mass and decreases with the distance.

The remaining question is how to make use of the information contained in the velocity direction. We expect that pixels with large velocity differences are not likely to be bounded to each other, for two reasons: First, a larger velocity separation implies a larger

kinematic energy, which consequently decreases the likelihood of being gravitationally bound. Second, it is found that the molecular gas obeys the Larson's relation [Larson, 1981] where the spatial length and velocity dispersion are related by [3]

$$\delta v \sim \delta r^{1/2} \ . \tag{3.2}$$

As a result, a larger velocity separation implies a larger spatial separation, which implies a lower gravitationally boundedness.

Here, we define the gravitational boundedness contributed from pixel j to pixel i as

$$I_{j \to i} = \frac{G m_j}{\delta r_{ij} \delta v_{ij}^2} \ . \tag{3.3}$$

The boundedness $I_{j \to i}$ increases with mass and decreases with spatial and velocity separation. Apparent similarities exist between Eq. 3.3 and the virial parameter. The virial parameter is defined as [Bertoldi & McKee, 1992][4]

$$\alpha_{\mathrm{vir}} = \frac{G \ m}{5 \ \sigma_{\mathrm{v}}^2 \ r} \ , \tag{3.4}$$

where m, r, σ are the mass, radius and velocity dispersion of the clumps. The virial parameter is a measurement of the gravitational boundedness of a clump. The quantity $I_{j \to i}$ defined by Eq. 3.3 has a dimension of [G Mass / Radius Velocity^2], which is the same as that of the virial parameter. Therefore, Eq. 3.3 can be viewed as a generalization of the virial parameter to a pixel pair, and a larger $I_{j \to i}$ is related to a larger change for pixel i to be bounded by pixel j.

3.2.2 The G-virial

We *define* the G-virial of a pixel i as the *sum* of the gravitational boundedness contributed from all the other pixels j. To be more precise,

$$\begin{aligned}
\alpha^i_{\texttt{G-virial}} &\equiv \sum_j I_{j \to i} \\
&= G \times \sum_j \frac{m_j((x_i - x_j)^2 + (y_i - y_j)^2)^{-\frac{1}{2}}}{(v_i - v_j)^2} \ ,
\end{aligned} \tag{3.5}$$

where $I_{j \to i}$ comes from Eq. 3.3.

---

[3]Here the power law index may vary among the literature. In Larson [1981] the index is 0.38 and in Roman-Duval et al. [2011] the index is found to be 0.51.

[4]Here our virial parameter is $E_{\mathrm{p}}/2 \ E_{\mathrm{k}}$, and in Bertoldi & McKee [1992] the virial parameter is $2 \ E_{\mathrm{k}}/E_{\mathrm{p}}$.

The physical meaning of Eq. 3.5 can be understood as follows: for one pixel i, its `G-virial` is determined by summing up its boundedness with all the other pixels j.

In Eq. 3.5, if j is close to i in both the spatial and the velocity direction, it contributes more to the `G-virial` at location i. The contribution is proportional to the mass m_j, and inversely proportional to δr_{ij} and δv_{ij}^2.

The reasons for the name `G-virial` in Eq. 3.5 include the followings: first, we name it as `G-virial` to emphasize its connection with the commonly-used *virial parameter*. Second, we added the letter `G` to emphasize that our virial parameter is a generalized version of the virial parameter and it is *global*. Different from the case of Bertoldi & McKee [1992] and Goodman et al. [2009] where the virial parameter is used to quantify self-gravity, our `G-virial` takes all the gravitational interactions between gas in the data cube into account. More clarifications concerning the concept of the `G-virial` can be found in Appendix 3.9.1.

The definition of the virial parameter in Bertoldi & McKee [1992] requires that the system is virialized. However, the concept of gravitational boundedness is more general and can be applied to the cases where the system has not virialized yet. Therefore, the `G-virial` method can be used to study the gravitational boundedness of both virialized and unvirialized systems.

3.3 Separating components with different velocities

One difficulty that we need to deal with is the line-of-sight confusion. Indeed, when calculating the `G-virial`, different components along the same line of sight are distinguished through their velocities. If two components happen to have the same velocity, the `G-virial` will be over-estimated, since the physically-unassociated components are treated as one single component in the calculations.

We argue that in many cases, the separation in the velocity axis do provide information so that we can separate different components based on the velocity difference. Let's consider two cases, the first one is the line-of-sight confusion in a given molecular cloud, and the second one is the line-of-sight confusion in our Milky Way disk.

In a molecular cloud, we can separate different components along the line of sight through the Larson's relation [Larson, 1981, Roman-Duval et al., 2011]. This is because the boundedness is proportional to $I \sim \delta r^{-1} \delta v^{-2}$ (Eq. 3.3) where δr and δv are the separations in position and velocity respectively. When two points stay along the same line of sight, the boundedness is likely to decrease since the velocity is likely to be different.

In the case of the Milky Way disk, since different spiral arms usually have different velocities, they will be separated easily in our calculations. Recall that in Eq. 3.3 the interaction is proportional to δr^{-1} and δv^{-2}. Therefore a small separation in velocity will lead to a huge decrease in interaction and finally make the contribution to the total G-virial negligible.

3.4 Numerical procedure

In the case of a 3D position-position-velocity data cube, for a pixel (x, y, v), we can rewrite Eq. 3.5 in its integral form,

$$\alpha_{\text{G-virial}}(x, y, v) =$$

$$\int \frac{Gm(x', y', v')}{((x - x')^2 + (y - y')^2)^{1/2}} \frac{1}{(v - v')^2 + c_0^2} \mathrm{d}x' \mathrm{d}y' \mathrm{d}v' , \quad (3.6)$$

where the integration is carried out over the whole data cube. With an observationally-constructed distribution of mass in the 3D position-position-velocity data cube, we can easily construct the G-virial using Eq. 3.6. In Eq. 3.6 we use $((v - v')^2 + c_0^2)$ instead of $(v - v')^2$ to suppress the contributions from pixels with velocity separations smaller than c_0. The reason is that a velocity separation of zero is not physical. The minimum meaningful velocity separation in a gas cloud is the sound speed. In our calculations, c_0 is chosen to be 1 km s^{-1}, which is comparable to the sound speed. The effect of changing c_0 will be discussed in Appendix 3.9.2.

Eq. 3.6 takes the form of a convolution, and can be conveniently calculated in Fourier space. In real space, the kernel is

$$K_{\text{x}} = \frac{1}{(x^2 + y^2)^{1/2} (v^2 + c_0^2)} , \quad (3.7)$$

and in Fourier space it can be shown that

$$K_{\text{k}} = \frac{2\pi}{(k_{\text{x}}^2 + k_{\text{y}}^2)^{1/2}} \frac{\pi e^{-c_0 |k_{\text{v}}|}}{c_0} . \quad (3.8)$$

Equation 3.8 enables us to calculate the G-virial map efficiently. In our calculations, we first make a 3D Fast Fourier Transform to the observationally-constructed mass distribution $m(x, y, v)$ and obtain $m_{\text{k}}(k_{\text{x}}, k_{\text{y}}, k_{\text{v}})$. Then we calculate the G-virial in

the Fourier space

$$\alpha_k(k_x, k_y, k_v) \qquad = \qquad m_k(k_x, k_y, k_v) \qquad \frac{1}{(k_x^2 + k_y^2)^{1/2}} \frac{\pi e^{-c_0|k_v|}}{c_0} \qquad . \quad (3.9)$$

In the last step the `G-virial` map is obtained by a inverse Fast Fourier Transform of α_k.

It can be found in Appendix 3.9.2 that the absolute values of the `G-virial` are dependent on c_0, however, the relative values of the `G-virial` are insensitive to c_0. As a result, the `G-virial` is a relative measurement of gravitational boundedness rather than an absolute one. In order for the `G-virial` maps from different regions to be comparable, a unique value of c_0 has to be chosen. c_0 also needs to be larger than the velocity resolution of the observations.

3.5 Numerical test

3.5.1 Quantifying gravity with G-virial

We validate the `G-virial` method by testing with a simple analytical model. For simplicities, the model is spherically symmetric. Along the radial direction, the density of the model decreases with radius, and the velocity of the model increases with radius.

This model is designed to mimic a typical molecular condensation [e.g. McKee & Tan, 2003]. In this study, the model is defined within $r_{in} < r < r_{out}$ where r is the radius, $r_{in} = 1$ pc and $r_{out} = 10$ pc. The density structure is

$$\rho(r) = \left(\frac{r}{r_0}\right)^{\gamma_\rho} \times \rho_0 , \qquad (3.10)$$

where $r_0 = 1$ pc, $\rho_0 = 10^3 \times m_{H_2}$ where m_{H_2} is the mass of molecular gas, and $\gamma_\rho = -2.2$. The velocity structure is parametrized as

$$v(r) = \left(\frac{r}{r_0}\right)^{\gamma_v} \times v_0 , \qquad (3.11)$$

where $r_0 = 1$ pc, $\gamma_v = 0.5$ and $v_0 = 1$ km s^{-1}. At a given radius, the magnitude of velocity is distributed uniformly between $0.9\ v(r)$ and $1.1\ v(r)$, and the direction of the velocity is distributed uniformly in 3D.

We define the virial parameter of a particle in our model (*p-virial*) as the ratio between its potential energy and its kinematic energy measured with respect to the center of
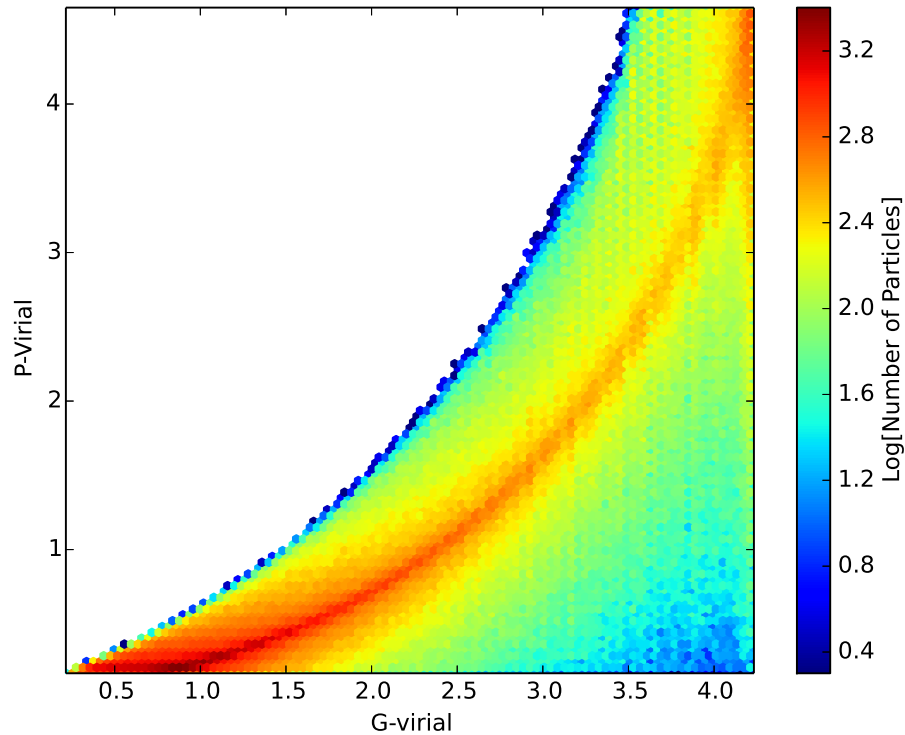
FIGURE 3.2: A comparison between the partical virial parameter *p-virial* the model and their `G-virial`.

mass. This definition is valid only when the center of mass is well-defined (see Appendix 3.9.1 for discussions). This model *p-virial* at a radius r can be expressed as as

$$\alpha_{\text{p-virial}}^{\text{model}} = \frac{E_{\text{p}}}{2\ E_{\text{kin}}} \ , \tag{3.12}$$

where E_p is the gravitational energy, which can be further expressed as

$$E_{\text{p}} = G\ m\ \left(\frac{1}{r} \times \int_{r_{\text{in}}}^{r'} 4\pi r'^2 \rho(r') \mathrm{d}r' + \int_{r}^{r_{\text{out}}} 4\pi r' \rho(r') \mathrm{d}r' \right) \ , \tag{3.13}$$

and

$$E_{\text{kin}} = \frac{1}{2}\ m\ v^2 \ , \tag{3.14}$$

is the kinematic energy where m is the mass of a particle.

The model is sampled through a total of 10^5 particles, and then turned into a 3D position-position-velocity data cube where the `G-virial` is evaluated. In the calculation, we take $c_0 = 1$ km s^{-1}.

In Fig. 3.2 we compare the virial parameters of the particles (*p-virial*) with their
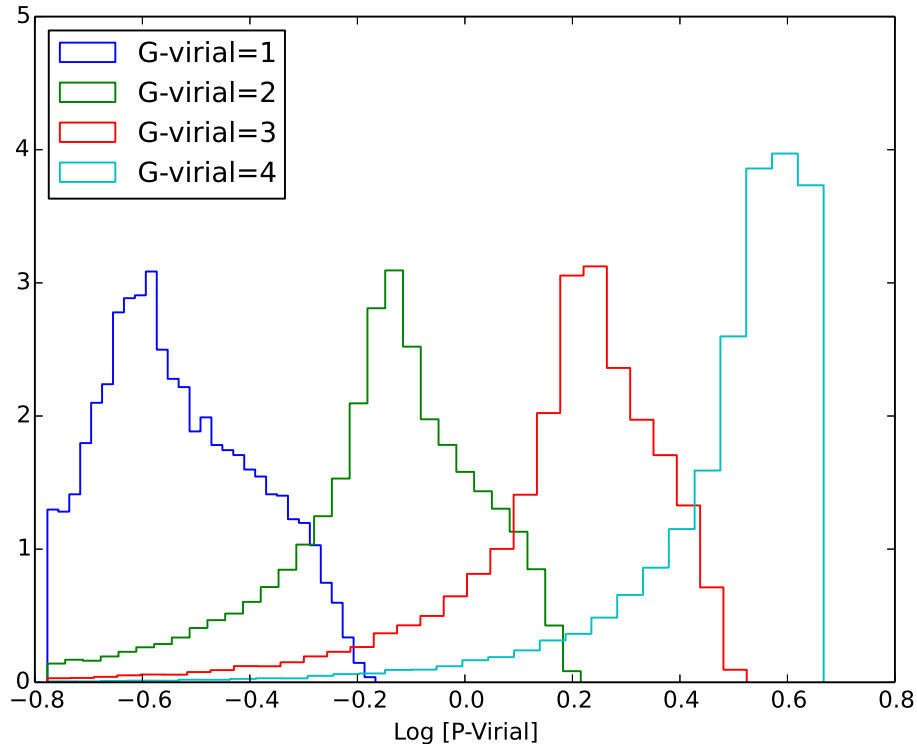
FIGURE 3.3:   Distribution of the model virial parameters at different values of the
`G-virial`.

`G-virial`. There is a good correspondence between *p-virial* and `G-virial` in that a
larger *p-virial* is related to a larger `G-virial`. However, the relation between *p-virial*
and `G-virial` is non-linear. Therefore the `G-virial` is a *relative* measurement of the
importance of gravity rather than an absolute one. Indeed, the absolute values of the
`G-virial` depend on the c_0 (Appendix 3.9.2). In Fig. 3.3 we select different values of
the `G-virial`, and plot the distributions of the model virial parameters. Particles with
the same `G-virial` have a distribution of *p-virial*. The primary reason for the scatters
of the *p-virial* is the projection effect: a particle may appears to be bound to another
particle in the 2D projection but in fact unbound in 3D. In spite of this, particles of
different *p-virial* can be separated based on their `G-virial`. Note that the uncertainty
will become smaller if we consider a continuous region rather than a single pixel.

3.5.2   Internal structure of the regions

For a given region, its `G-virial` map is centrally concentrated, and if we divide the region
based on different contours with different `G-virial` values, we get a set of regions that
nest inside one another. This allows us to evaluate the spatial concentration of molecular

gas based on contours of constant `G-virial` parameters. Inside a closed region where the `G-virial` of the pixels is larger than a given threshold, we can evaluate the parameters such as mass, radius and velocity dispersion. Suppose we have a map of mass distribution $m(x, y, v)$ and a map of the `G-virial` $\alpha_{\texttt{G-virial}}(x, y, v)$, the corresponding parameters are evaluated by taking all the pixels inside a given contour of the $\alpha_{\texttt{G-virial}}(x, y, v)$ map into account. The mass of a region is defined as

$$m = \int_R \rho(x, y, v) \mathrm{d}x\mathrm{d}y\mathrm{d}v , \qquad (3.15)$$

where R denotes a coherent region that satisfies $\alpha_{\texttt{G-virial}}(x, y, v) > \alpha_{\min}$ and the central velocity of a region is defined as

$$v_0 = \frac{\int_R \rho(x, y, v) \ v \ \mathrm{d}x\mathrm{d}y\mathrm{d}v}{\int_R \rho(x, y, v) \ \mathrm{d}x\mathrm{d}y\mathrm{d}v} . \qquad (3.16)$$

The velocity dispersion is defined as

$$\sigma_{\mathrm{v}} = \left(\frac{\int_R \rho(x, y, v) \ (v - v_0)^2 \ \mathrm{d}x\mathrm{d}y\mathrm{d}v}{\int_R \rho(x, y, v) \ \mathrm{d}x\mathrm{d}y\mathrm{d}v} \right)^{1/2} . \qquad (3.17)$$

The radius of the region is defined by diagonalizing the tensor of second moments of the position coordinates weighted by the intensity [Goodman et al., 2009], and is defined as

$$R = 1.91 \times (\sigma_{\min}\sigma_{\max})^{1/2} , \qquad (3.18)$$

where $\sigma_{\min}$, $\sigma_{\max}$ are the dispersions along the major and minor axes.

In Fig. 3.4 we compare the mass-radius relation reconstructed using the `G-virial` with the mass-radius relation in the model, and in Fig. 3.5 we compare the velocity dispersion-radius relation reconstructed using the `G-virial` with the model velocity-radius relation. The kinematic structure of the model can be reasonably constrained through the observations. This is not sensitive to c_0. This is because the definition of the regions R depends only on the *relative* values of the `G-virial`, which is unchanged if we change c_0 (Appendix 3.9.2).

3.6   Applications to molecular clouds

In this section we present applications of our method to several molecular clouds. Our method requires a map of the distribution of molecular gas in the 3D position-position-velocity space. Observationally this can be conveniently achieved using rotational transitions of the CO molecule.
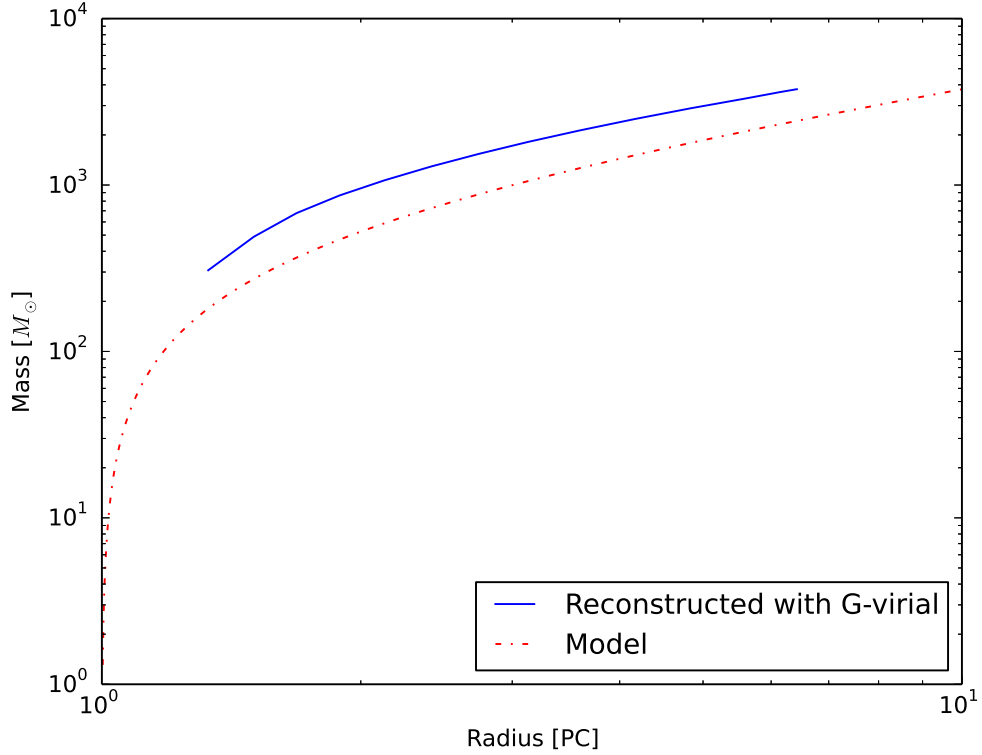
FIGURE 3.4: A comparison between the mass-radius relation of the model and the mass-radius relation reconstructed with the `G-virial`. See section 3.5.2 for details.

In the simplest case, this can be achieved by observing the ^{13}CO(1-0) transition alone. Assuming an excitation temperature of 10 K, a ^{12}CO abundance of X(^{12}CO/H$_2$)=8 × 10^{-5}, and a ^{12}CO to ^{13}CO ratio of R(^{12}CO/^{13}CO)=45, the column density can be estimated as [Simon et al., 2001, Roman-Duval et al., 2010]

$$N(H_2) = 4.92 \times 10^{20} \times \frac{T_{\mathrm{mb}}}{\mathrm{K}} \times \frac{\delta_{\mathrm{v}}}{\mathrm{km\ s^{-1}}} \ , \tag{3.19}$$

where T_{mb} is measured in K and δ_{v} is the velocity resolution of the data cube measured in km s^{-1}. Changing the excitation temperature to 20 or 30 K decreases the derived mass by 40% and 92%, respectively [Simon et al., 2001]. For an observed ^{13}CO(1-0) data cube $T_{\mathrm{mb}}(x, y, v)$, we construct a mass distribution $m(x, y, v)$ using

$$\frac{m(x, y, v)}{g} = 4.92 \times 10^{20} \ \times \frac{T_{\mathrm{mb}}(x, y, v)}{\mathrm{K}} \frac{\delta_{\mathrm{v}}}{\mathrm{km\ s^{-1}}}$$

$$\times \frac{m_{\mathrm{H_2}}}{g} \times \left(\frac{\delta_{\mathrm{x}}}{\mathrm{cm}}\right)^2 \ , \tag{3.20}$$

where δ_{x} is the pixel size of the spatial dimension in cm and δ_{v} is the channel width in km s^{-1}.
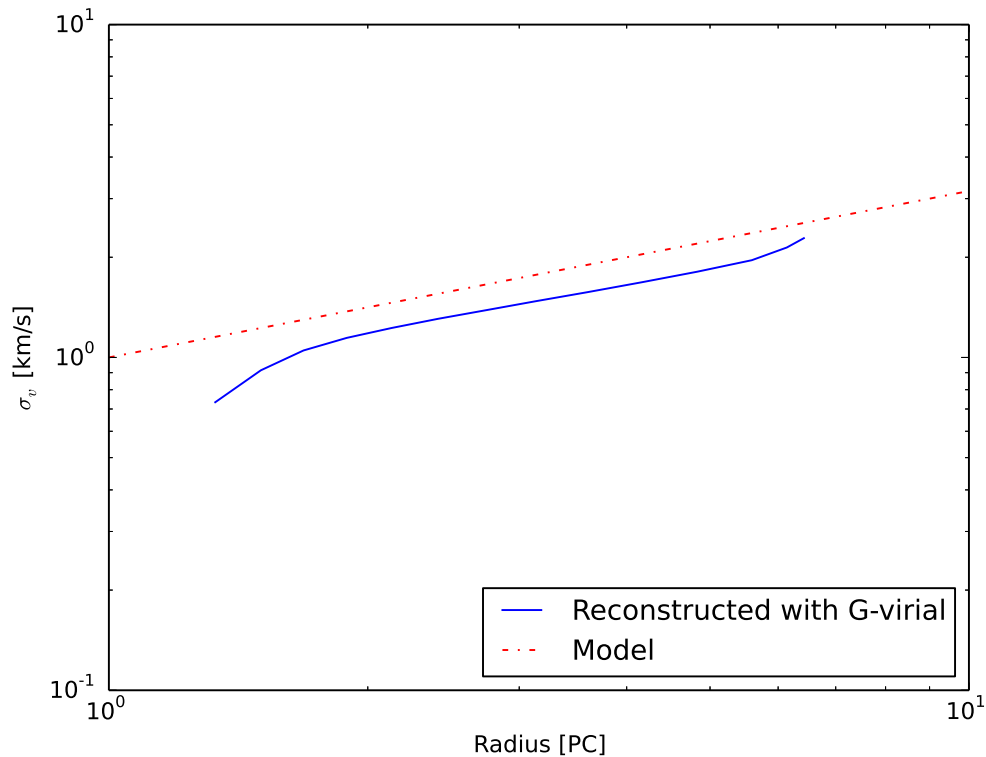
FIGURE 3.5: A comparison between the velocity-radius relation of the model and the velocity dispersion-radius relation reconstructed with the `G-virial`. See section 3.5.2 for details.

We apply our `G-virial` method to the publicly available data from the COMPLETE survey [Ridge et al., 2006]. The observations have a spatial resolution of 46 arcsec and a velocity resolution of 0.067 km s^{-1}, the mean RMS per channel is ~ 0.33 K in terms of T_A^*, and the beam efficiency is ~ 0.5.

With a distance of 250±50 pc and a total mass of $10^4 M_\odot$ [Enoch et al., 2006], the Perseus molecular cloud is among the best-studied molecular clouds in the Milky Way. It is composed of several distinct regions such as B1, B3, NGC1333 and IC348. The Ophiuchus molecular cloud has a distance of 125pc and a mass of 7×10^3 $M_\odot$ [de Geus et al., 1989] and contains clouds L1688 and L1689. In particular, L1688 and NGC1333 are cluster-bearing regions. IC348 also hosts a star cluster however it is generally considered older compared to other regions in Perseus [Gutermuth et al., 2009].

In this section, we provide a study of the structure of the Perseus and Ophiuchus molecular cloud with our `G-virial` method. We present maps of the `G-virial`, together with an analysis of the structure of the regions in the clouds based on the `G-virial` method.
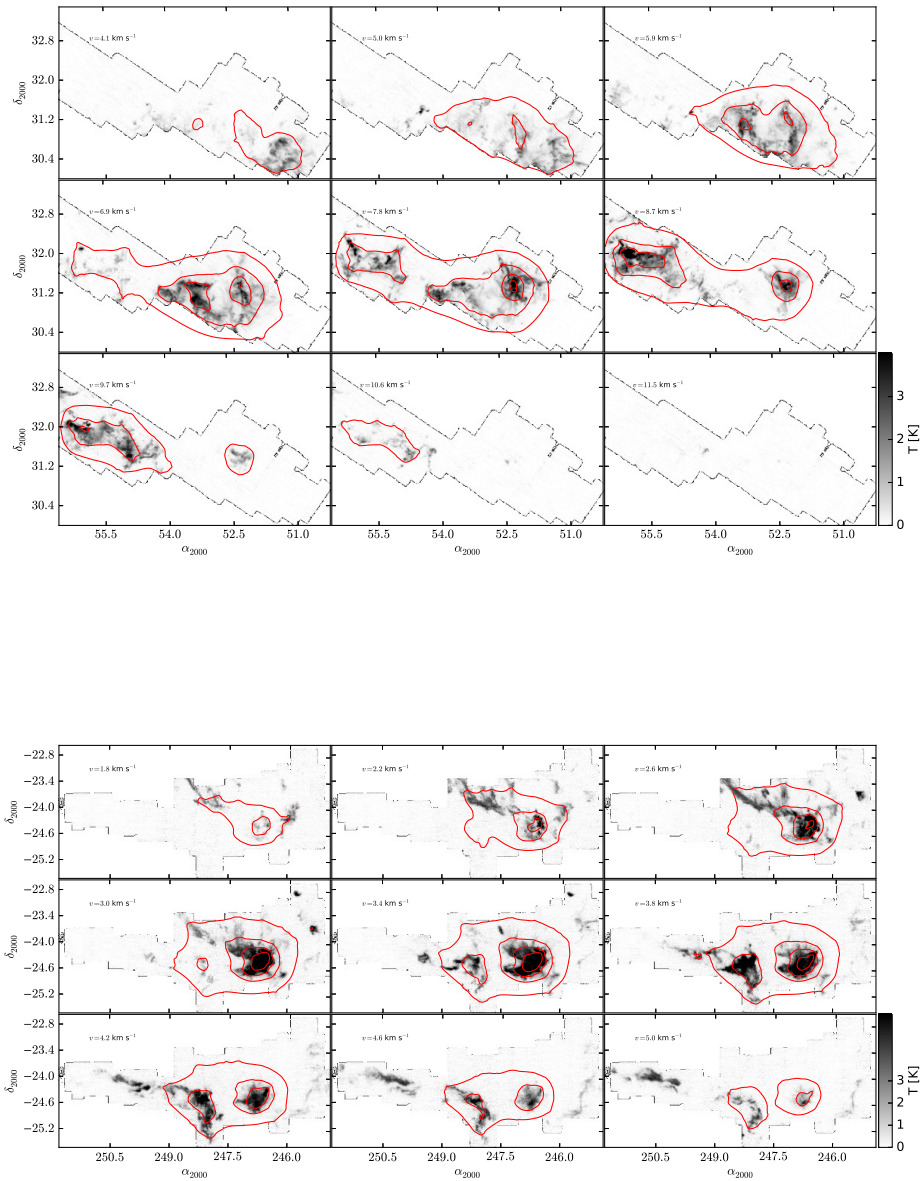
FIGURE 3.6: Channel maps of the ^{13}CO(1-0) emission and the corresponding `G-virial`. The upper panel shows the results from the Perseus molecular cloud and the lower panel shows the results from the Ophiuchus molecular cloud. Grayscale images stand for ^{13}CO(1-0) emission and the red contours represents the `G-virial`. Contour levels start from 1.2 in step of 0.8.

3.6.1 Maps of the G-virial parameter

In Fig. 3.6 we channel maps of the `G-virial` in the 3D position-position-velocity space. 3D renderings of the maps are presented in Appendix 3.9.3. For both clouds, the ^{13}CO(1-0) maps contain complicated and filamentary structure, whereas the `G-virial` maps are

smooth and contain less structures. Interestingly, higher values of `G-virial` are reached only at cluster-bearing regions such as NGC1333, IC348 and L1688, and this highlights the importance of gravity in such regions. Different regions are indicated in Fig. 3.7.

3.6.2 Identification of Regions

The `G-virial` offers a new way to divide the molecular cloud into regions. Previously, this has been done either by visual inspection, or with contour-based algorithms such as `clumpfind` [Williams et al., 1994]. It is worth mentioning that other region-finding algorithms are available, such as `dendrogram` [Rosolowsky et al., 2008] and `dochamp` [Whiting, 2012].

Many of the algorithms (e.g. `clumpfind` and `dendrogram`) are contour-based, and they tend to assign pixels to regions based on iso-column-density contours in the 2D case or on iso-intensity contours in the case of a 3D position-position-velocity data cube. Molecular clouds are characterized by a set of complicated hierarchical structures, and a naive application of the `clumpfind` tends to produce hundreds of "clumps" for one single molecular cloud. It has also been pointed out recently that contour-based methods suffer from superposition and confusion when the volume filling factor of emitting material is large [Beaumont et al., 2013].

In our analysis we focus on the role of gravity at a scale that is much larger than that of the individual structures identified with `clumpfind`, and as a result we need to identify much larger structures. This is achieved by applying the `dendrogram` [5] algorithm to our maps of the `G-virial`. Since the `G-virial` maps are much smoother than the intensity map, we can easily identify large and coherent regions from the position-position-velocity data cube. Moreover, gas in one individual region should be gravitationally interacting since it shares a common peak in the `G-virial` map. Fig. 3.7 shows the regions identified by applying the `dendrogram` algorithm to our `G-virial` map. In the `dendrogram` calculations, the minimum difference between different contours is set to 0.4, and the regions correspond to the "leaves" of the `dendrogram`. Each identified region consists of a continuous list of pixels in the 3D position-position-velocity space. In Fig. 3.7 the projected boundaries of the regions are plotted [6].

Compared to the `clumpfind`, our method tends to identify regions that are coherent and the `clumpfind` tends to break up those regions. The reason is that our `G-virial` map is much smoother than the original map [7]. With `G-virial` we can study the structure of

---

[5]Obtained from http://dendrograms.org/.

[6]All the regions are originally defined in 3D.

[7]This is similar to the case of Smith et al. [2009] where they identified structures form a simulation in the 3D position-position-position space based on gravitational potential.
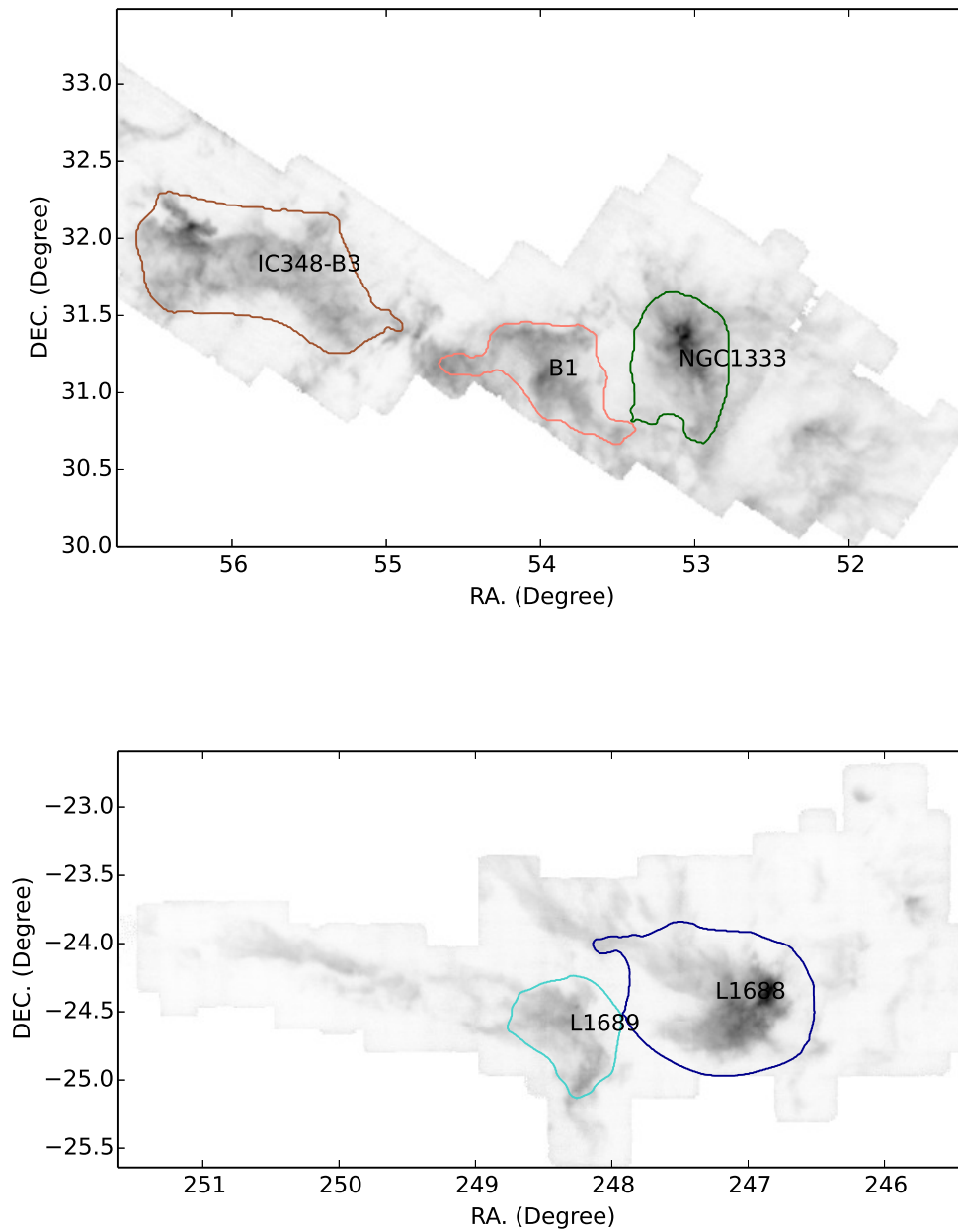
FIGURE 3.7: Regions identified by applying the `dendrogram` algorithm to our `G-virial` map. The grayscale images correspond to the velocity-integrated $^{13}CO(1-0)$ emission and the contours correspond to the projected boundaries of the identified regions. These regions correspond to the "leaves" of the `dendrogram`. The conventional names of the regions are labeled.

molecular gas in terms of *gravitationally coherent* regions. In the 2D case, our method is similar to the `gridcore` code which is based on 2D projected gravitational potential [Gong & Ostriker, 2011].

3.6.3   Internal structure of the regions

In this section we study the internal structure of the molecular gas in the individual regions. Previously, the structure of molecular gas was studied in terms of the clumps, and quantified using parameters that are evaluated for the whole clumps. While those methods do provide constraints on the role of gravity inside the regions, the role of gravity at on scales scales larger than the individual gas condensations is neglected. The spatial structure of molecular gas larger than the clump scale can be quantified using the `dendrogram` algorithm. However, the `dendrogram` method is contour-based, and only the connection between the adjacent regions are preserved. This makes it difficult to use `dendrogram` to quantify the structure of molecular gas on the large scale.

Here we provide an analysis of the structure of the individual regions with the `G-virial` method. As we have shown in section 3.5.2 the mass-radius and velocity-radius relation in the model can be reasonably reconstructed with our `G-virial` method.

In Fig. 3.8 we plot the dependence of velocity v_0 and velocity dispersion σ_v on the radii of the regions. The inner parts of the regions stay well at the center of the outer part of the regions in velocity space. This means the central part of the regions stays quiescent with respect to the outer parts, and this is consistent with the findings by Kirk et al. [2010], Walsh et al. [2004], André et al. [2007].

We assess the importance of gravity in these regions with the `G-virial` method. In our method, a larger `G-virial` is related to a larger importance of gravity, and as a result, the importance of gravity at a given region can be quantified by measuring the amount of gas at different thresholds of the `G-virial` parameter. In Fig. 3.9, we plot the dependence of gas mass on the `G-virial` for different regions, and in Fig. 3.10 we plot the dependence of the `G-virial` on the radius. For all the observed regions, the `G-virial` increases towards the centers. For cluster-bearing regions such as NGC1333 in Perseus and L1688 in Ophiuchus, much higher `G-virial` values have been reached at their centers. In short, we found a connection between higher `G-virial` and the clustered mode of star formation in these regions.

With our method it is straight-forward to derive relations such as the mass-radius and velocity-size relation. Recently, there has been growing interests in quantifying cloud structure in terms of various mass-size relations [e.g. Kauffmann et al., 2010a,b]. In Fig
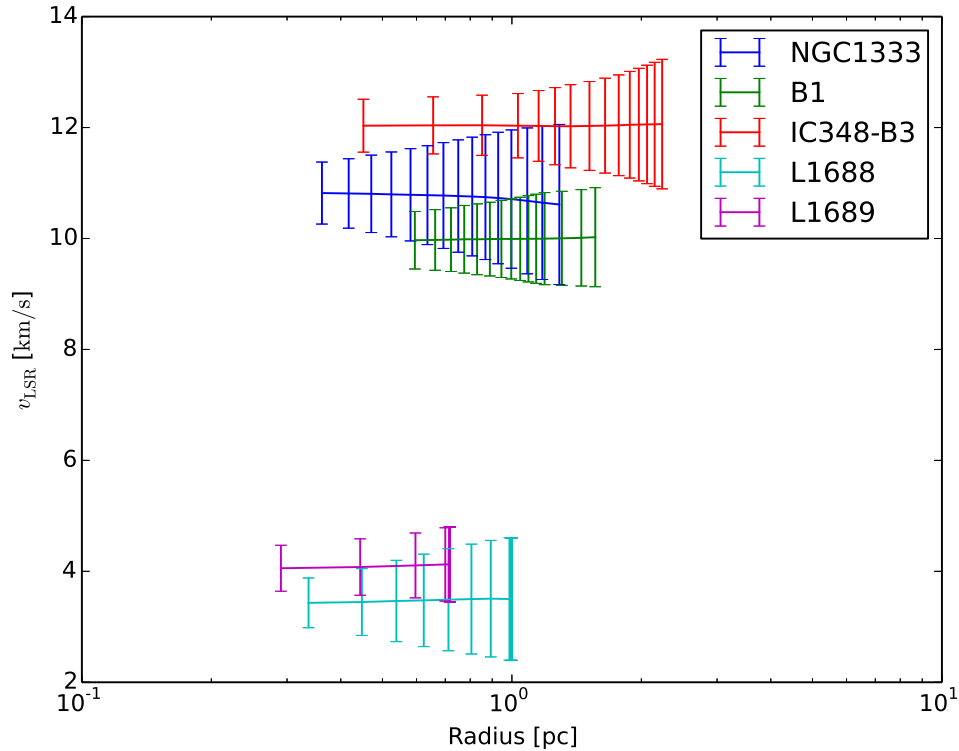
FIGURE 3.8: Dependence of velocity and velocity dispersion as a function of radius. Here the solid lines stand for the velocities of the regions, and the errorbars stand the velocity dispersions of the regions at given radii. The vertical extent of the errorbars are the 3D velocity dispersion $\sigma_v^{3D} = \sqrt{3}\,\sigma_v$.

3.11 we plot the mass-size relation obtained using our G-virial method (c.f. Section 3.5). Our mass-size relation is different from that of Kauffmann et al. [2010b] since the regions in our case are much more coherent. Another difference is that in our case the mass is evaluated within a given region where the G-virial is larger than a threshold, and in Kauffmann et al. [2010b] the mass in evaluated within a region where the column density is larger than a given threshold. In our case, along one single line of sight, only the gas that stays within a given surface of a constant value of the G-virial is taken into account while in Kauffmann et al. [2010b] all the mass along the line of sight is taken into account. Similar to Kauffmann et al. [2010b], we also found that cluster-bearing regions such as L1688 and NGC1333 are more massive than the regions devoid of clusters at a give radius. In Fig. 3.11 we also plot the scaling relations proposed in Larson [1981, $m(r) = 460 M_\odot (r/\mathrm{pc})^{1.9}$] and Kauffmann et al. [2010b, $m(r) = 400 M_\odot (r/\mathrm{pc})^{1.7}$] , and found that both provide reasonable descriptions of the structure of the regions approximately.

Molecular clouds are believed to be turbulence-dominated, and this is mainly inferred from the fact that the clouds obey the velocity-linewidth relation [Larson, 1981]. In Fig.
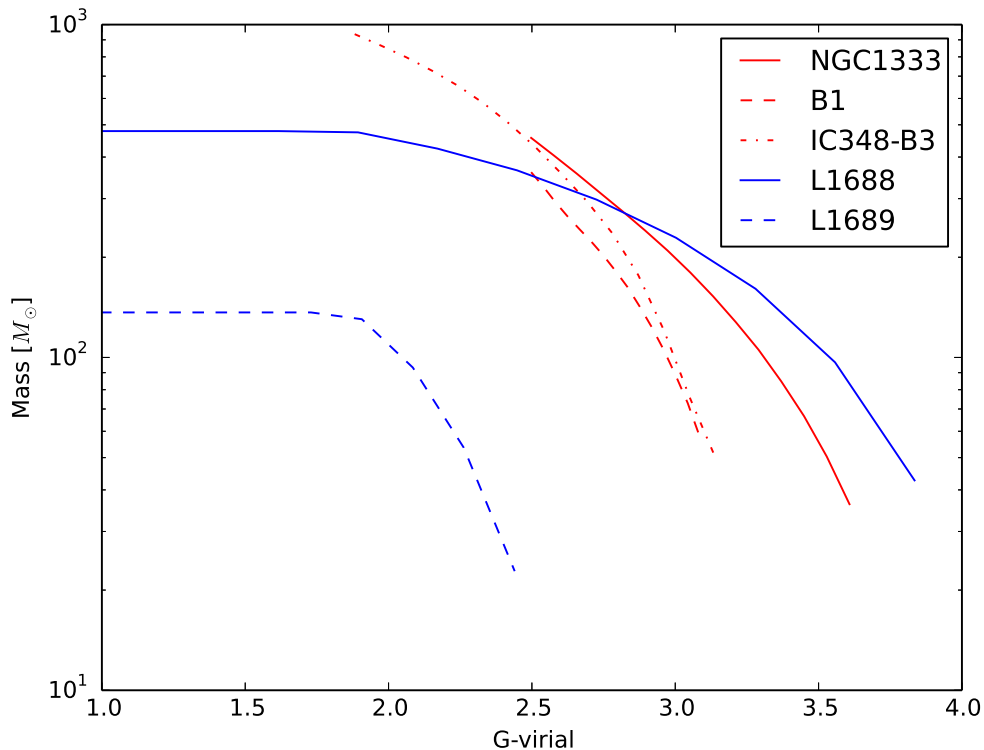
FIGURE 3.9: The amount of molecular gas enclosed in regions with different thresholds of the `G-virial`. The x-axis is the threshold of `G-virial` which we take to define the region, and the y-axis is the amount of gas that is enclosed in the region.

3.12 we plot the 3D velocity dispersion of our regions as a function of radius. Here the 3D velocity dispersion is $\sqrt{3}$ times of the velocity dispersion evaluated in Eq. 3.17. The scaling relation from Larson [1981] is also plotted ($L/\mathrm{pc} \sim 1.01 \times (\sigma_{\mathrm{v}}/ \mathrm{km\ s^{-1}})^{0.38}$). In our case, the velocity-linewidth relation is evaluated for centrally-condensed objects, and a smaller physical scale is related to the inner part of a gas condensation, whereas in Larson [1981] a smaller physical scale is related to a smaller size of a sub-region in a cloud [8]. For our centrally-condensed objects, the scaling relation from Larson [1981] seems to be valid. We also note that cluster-bearing regions such as NGC1333 and L1688 have much larger velocity dispersions at large radii.

Heyer et al. [2009] found a dependence of the scaling coefficient $\sigma_{\mathrm{v}}/r^{1/2}$ of the Larson's relation on the column density, and attributed this to the fact that the clouds are in self-gravitational equilibrium. We plot $\sigma_{\mathrm{v}}/r^{1/2}$ as a function of column density $\Sigma \equiv M/\pi r^2$ where M is the mass and r is the radius of our regions (Fig. 3.13). Since we decompose one region into a set of nested sub-regions based on the `G-virial`, one single region will appear as a curve in Fig. 3.13. Our regions are quite close to being gravitationally

---

[8]The physical scale here can have different meanings, see Lazarian & Pogosyan [e.g. 2004], Heyer & Brunt [e.g. 2004], Roman-Duval et al. [e.g. 2011].
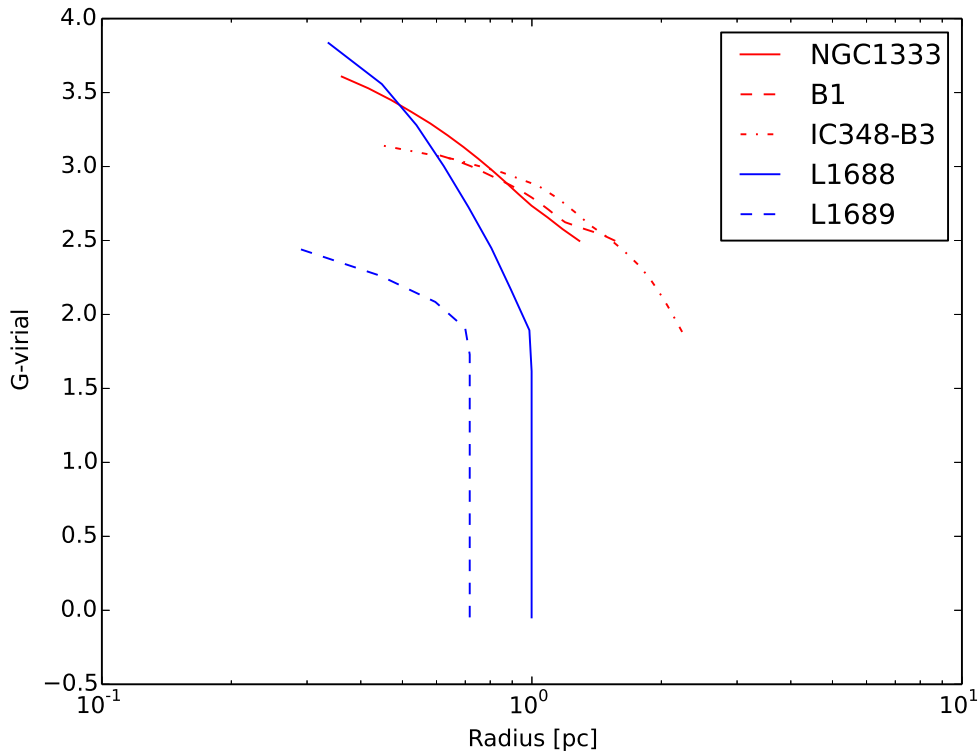
FIGURE 3.10: `G-virial` as a function of radius for different regions.

bound, and the scatter around the *y*-axis is much smaller than what is found for Milky Way molecular clouds as studied in Heyer et al. [2009]. This difference arises mainly from the fact that the `G-virial` method tends to identify regions that are gravitationally coherent. As a result, graviy is important throughout the regions.

3.7 Potential applications

The relevance of the `G-virial` method to the study of molecular gas and star formation can be understood in two aspects. First, the method offers a way to quantify the centrally-condensed molecular structures in the 3D position-position-velocity data cube. These structures, presumably produced by a combination of turbulence, gravity and magnetic field, provide the necessary conditions for the formation of stars and clusters. However, how the star formation process occurs depends on the kinematic structures of the gas condensations, which have not been well-quantified yet. Our method offers a framework to quantify the structure of these gas condensations in an uniform way, and enables us to compare these structures, either between theory and observations or between different observations.
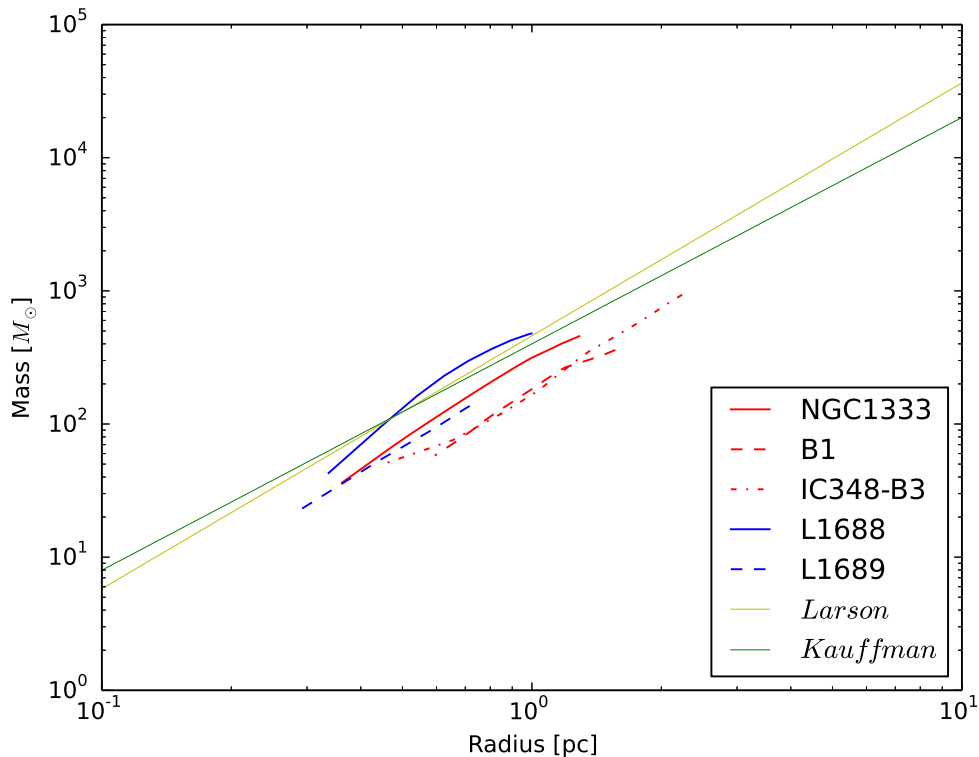
FIGURE 3.11: Enclosed mass as a function of radius for different regions. The scaling relation from Larson [1981] and Kauffmann et al. [2010b] are added. For all the curves, the `G-virial` goes down with increasing radii.

Second, the method offers a way to understand the importance of gravity. Star formation is a process that is driven ultimately by gravity. However, how gravity functions in molecular clouds is still largely unclear. One reason is that gravity is a long-range interaction and all the previous methods to quantify gravity in clouds tend to localize it [9]. With our method we are able to recover the effect of gravity across different physical scales, and this provides a more complete picture of the importance of gravity in star formation.

Since gravity is a process that is scale-free, the application of the method is not limited to molecular clouds for which it has been originally developed. It is applicable to other situations, e.g. to study the fragmentation of gas condensations observed at high-angular resolution observations, or to study the physical structure of star clusters where the velocity information is available. Such possibilities are still yet to be explored.

---

[9]`Dendrogram` can be viewed as one way of recovering the large-scale structure. However, the quantification of gravity with the virial parameter on the `dendrogram` depends on the tree structure, and is thus incomplete since the interaction between different branches are not fully accounted of. Therefore, a direct application of `dendrogram` method to molecular clouds are more suitable for the understanding of self-gravity [Goodman et al., 2009] rather than the importance of gravity for the cloud as a whole.
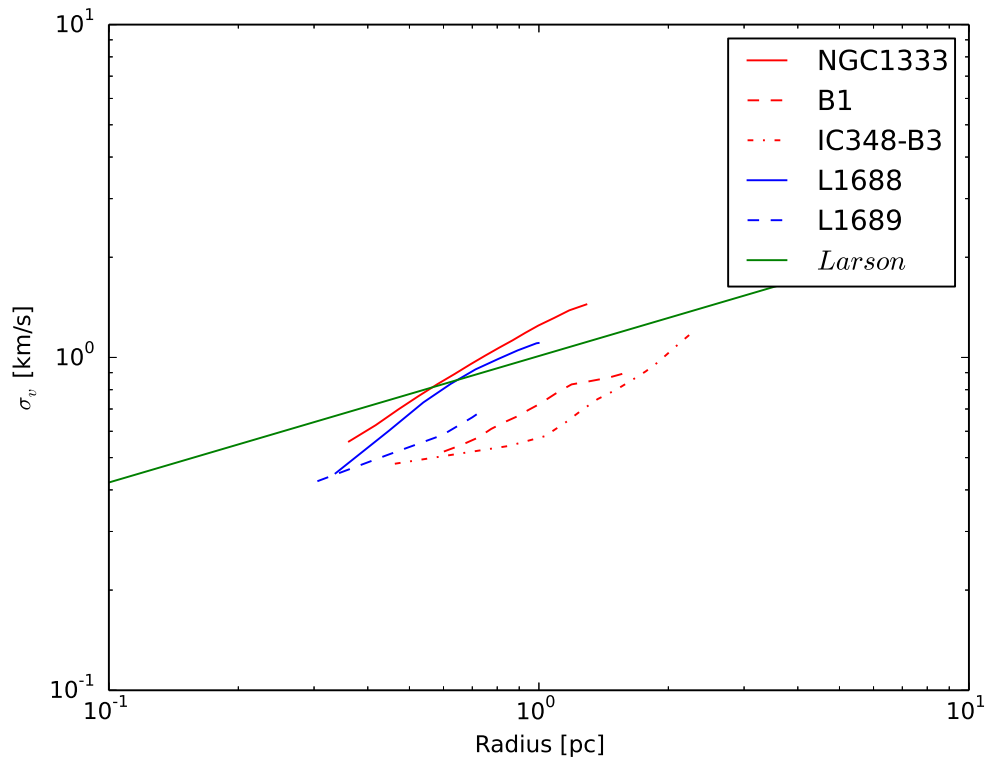
FIGURE 3.12: 3D velocity dispersion as a function of radius for different regions. The velocity-linewidth relation from Larson [1981] is also plotted.

Another open question in interstellar medium studies is the definition of an object. Indeed, what we refer to as a molecular cloud is a structure that is identified with certain algorithms [e.g. Jackson et al., 2006], and therefore the boundaries of the cloud are dependent on the algorithm employed. The commonly-used `clumpfind` [Williams et al., 1994] method tend to define a cloud based on iso-intensity contours in the 3D data cube. Since the structure of iso-intensity contours are highly complicated, the result of `clumpfind` relies on some technical parameters. With `G-virial`, it is possible to define objects through the *iso-G-virial* contours in the 3D data cube.

3.8 Conclusion

In this paper we proposed a *general method* (`G-virial`) to study the role of gravity in molecular clouds. Different from the previous methods which decompose molecular clouds based on contours in the 2D plane or 3D position-position-velocity data cubes, in this method all the gravitational interactions between all the pixels in the 3D data cubes are considered, and maps of the importance of gravity in the 3D position-position-velocity space can be generated.
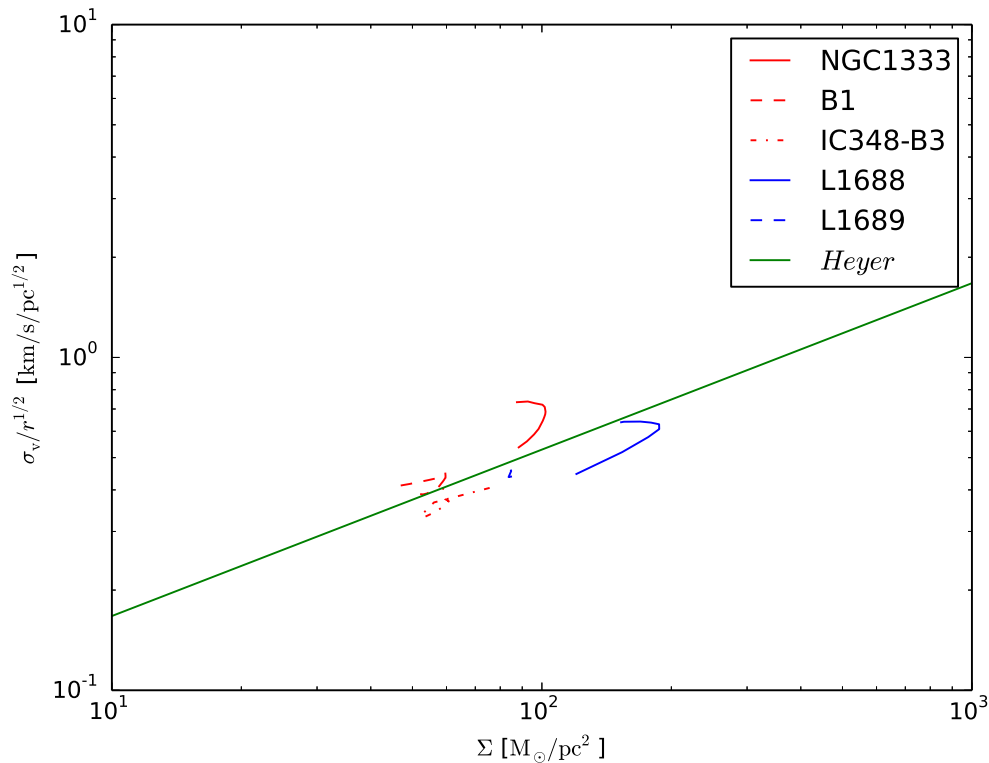
FIGURE 3.13: $\sigma_v/r^{1/2}$ as a function of column density σ for the regions. In order to be consistent with Heyer et al. [2009], σ_v is the 1D velocity dispersion as defined in Eq. 3.17 and $\Sigma \equiv M/\pi r^2$ where M is the mass r is the radius. The solid straight line shows the boundary below which the structures are gravitationally bound. It is defined as $\sigma_v/r^{1/2} = (\pi G/5)^{1/2}\Sigma^{1/2}$.

The generated 3D `G-virial` maps have a dimensionless unit that is the same as that of the virial parameter, and a larger `G-virial` is related to a larger chance of being gravitationally bound. Using a simple spherical-symmetric model, we demonstrate the connection between the `G-virial` of a particle and its gravitational boundedness. Different from the virial parameter which quantifies self-gravity, the `G-virial` quantifies the effect of *global* gravity on the gas where all the interactions between all the particles in the 3D data cube have been taken into account.

We analyzed the ^{13}CO(1-0) emission from the Perseus and Ophiuchus molecular clouds, and found that both can be decomposed into several regions which are gravitationally coherent (Fig. 3.7). Moreover, the cluster-bearing regions show higher values of `G-virial` at the centers which implies that gravity plays a more prominent role in these parts (Fig. 3.10).

`G-virial` maps take the form of 3D position-position-velocity data cubes. The iso-surfaces in the `G-virial` maps can be conveniently taken as bases to decompose and analyze the structures of the sub-regions in the clouds. In this work, we carried out

an analysis of a total of five regions identified in the Perseus and Ophiuchus molecular cloud, and derived mass-size relation and velocity dispersion-size relation for the regions. We found that cluster-bearing regions are more massive at a given radius than those which do not bear a cluster (Fig. 3.11), and the cluster-bearing regions have a higher velocity dispersion at the outer parts (Fig. 3.12).

We also found that the Larson relation [Larson, 1981] which describes the dependence of velocity dispersion of the regions as a function of region size, also holds within the regions (Fig. 3.12). The scaling coefficient for the Larson's relation appears larger for cluster-bearing regions, and this can be explained as due to an increase of gravity due to their larger column densities (Fig. 3.12, 3.13).

After demonstrating the capability of the `G-virial` to identify gravitationally coherent regions in the cloud, as well as its capabilities of decomposing the cloud and deriving relations such as mass-size and velocity-size relations, we suggest that our new method is useful for detecting and quantifying structures that take forms of 3D position-position-velocity data cubes, and should provide better pictures on how gravity functions in different situations.

3.9 Appendix

3.9.1 Relation between `G-virial` and the virial parameter

The relative importance between gravitational and kinematic energy is usually characterised with the virial parameter, which is introduced in Bertoldi & McKee [1992]. To evaluate the virial parameter, it is necessary to define a structure on which the virial parameter is calculated.

One difference between `G-virial` and the virial parameter is that to evaluate the `G-virial` no such boundary is needed. Therefore the `G-virial` can be viewed as a generalization of the virial parameter to a continuous distribution of mass.

To illustrate the physical meaning of the `G-virial`, we define a quantity called *particle virial, p-virial*, which is the ratio between the gravitational energy of a particle to its kinematic energy $\alpha_{\mathrm{p-virial}} = E_{\mathrm{p}}/2E_{\mathrm{k}}$. The potential energy E_{p} is determined by $m \times \phi$ where m is the mass of the particle and ϕ is the gravitation potential, and E_{k} is determined as $1/2 \times m \ (v - v_{\mathrm{c}})^2$. To define the kinematic energy, the velocity of the center of mass v_{c} is needed (e.g. the case of section 3.5). Therefore *p-virial* is only suitable to the cases where a center of mass can be easily found. In the case of a molecular cloud, this is not straightforward. This is because inside a molecular cloud
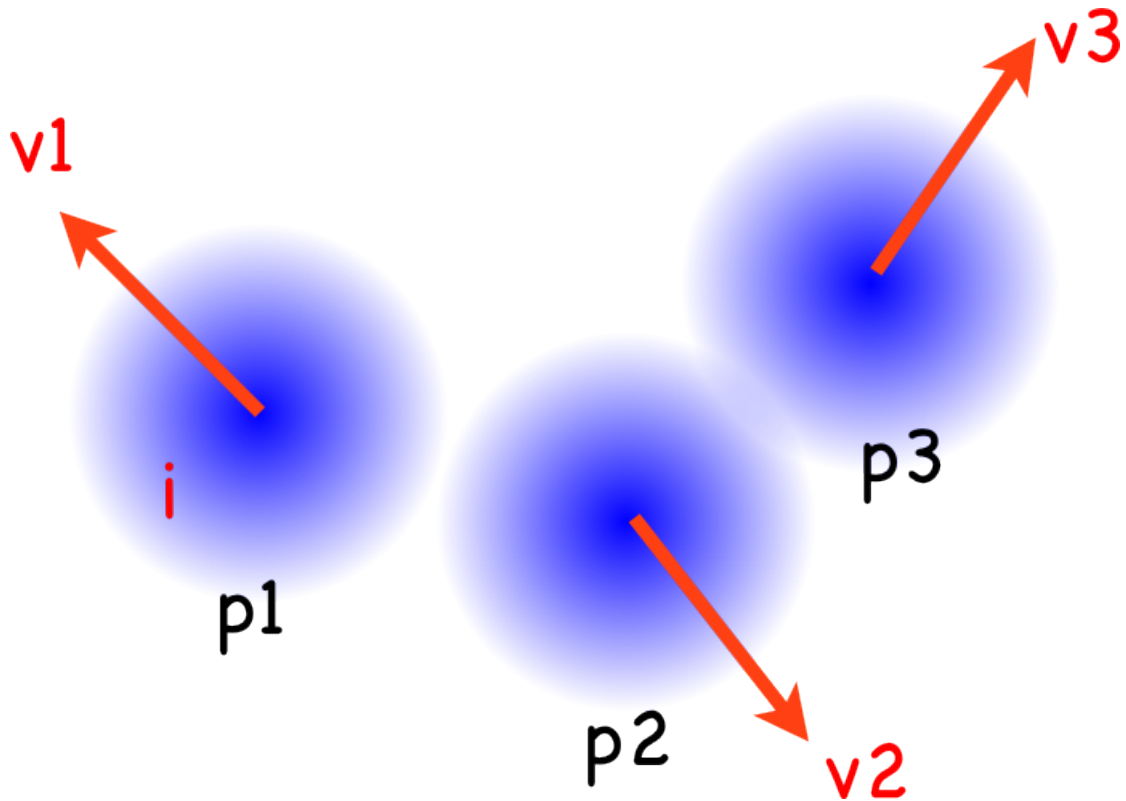
FIGURE 3.14: A illustration of the difficulty of finding a proper center of mass. Consider three clumps p1, p2, p3 moving at velocities v1, v2, v3. If we are interested in if i is gravitationally bound, since the majority of attraction comes from p1, physically the center of mass should be the center of mass of p1 instead of the center of mass of the three clumps p1, p2, p3, since p2, p3 do not contribute much gravitational attraction to i compared to p1. Therefore to estimated the gravitational boundedness, a naive calculation of the center of mass where all the mass in the whole cloud is included is not appropriate. In the case of a complicated distribution of gas, a choice of a center of mass is not straight-forward to find.

the condensations can move at different velocities. The velocity of the center of mass depends on which clumps are included in the calculation, which is not unique. This difficulty is illustrated in Fig. 3.14.

One major advantage of the `G-virial` over the *p-virial* is that no center of mass is needed. The `G-virial` is the sum of the gravitational boundedness, and to evaluate it, we do not need to introduce the center of mass. Therefore, the `G-virial` is suitable to the cases where we need to understand the importance of gravity even if the geometry of the object is complicated and the center of mass is not well defined.

3.9.2 Dependence on of `G-virial` the smoothing velocity c_0

The only free parameter in our method is the smoothing velocity c_0 in Eq. 3.6 (Section 3.4). We added this parameter to avoid the divergence of Eq. 3.6 when the separation

of velocity is zero.

Physically, if the velocity separation is zero, and if two gas particles spatially coincide with each other, the gravitational interaction will cause them to collide. However in reality the velocity separation can not be zero since the gas also have velocity dispersions that have either thermal or non-thermal origin [Larson, 1981]. A physically lower limit of c_0 should be the sound speed.

In reality, this is also affected by the superposition along the line of sight, since different gas which are physically unassociated can stay along the same line of sight and therefore appears as being gravitationally bound. Therefore it is difficult to find a unique value of c_0 based on first principles. In our case, we choose c_0 to be 1 km/s, which is larger than and still comparable to the sound speed.

Here we investigate how our results can be affected by varying the parameter c_0. First we made a `G-virial` map by assuming $c_0 = 1$ km/s and then we make another map by assuming $c_0 = 2$ km/s. Finally we make a pixel-by-pixel comparison of the maps (Fig. 3.15). We found that the major effect of changing c_0 is that the absolute values of `G-virial` changes. If we change c_0 to 2 km/s the `G-virial` decrease by a factor of ~ 2. However, there is good correspondence between the old and new `G-virial` values. Therefore, changing c_0 affects the absolute values of the `G-virial` however the relative values stays unaffected. Therefore, all our figures should be unaffected and the `G-virial` axes of Fig. 3.9 and Fig. 3.10 will change accordingly.

In the case where the `G-virial` is applied to different data cubes, in order for the results to be comparable, a unique choice of c_0 is necessary.

3.9.3 3D renderings of G-virial from both clouds

In order to provide intuitive representations of our `G-virial` maps, we present volume renderings of the 3D position-position-velocity data cubes with `yt` [Turk et al., 2011] in Fig. 3.6.

3.10 Acknowledgements
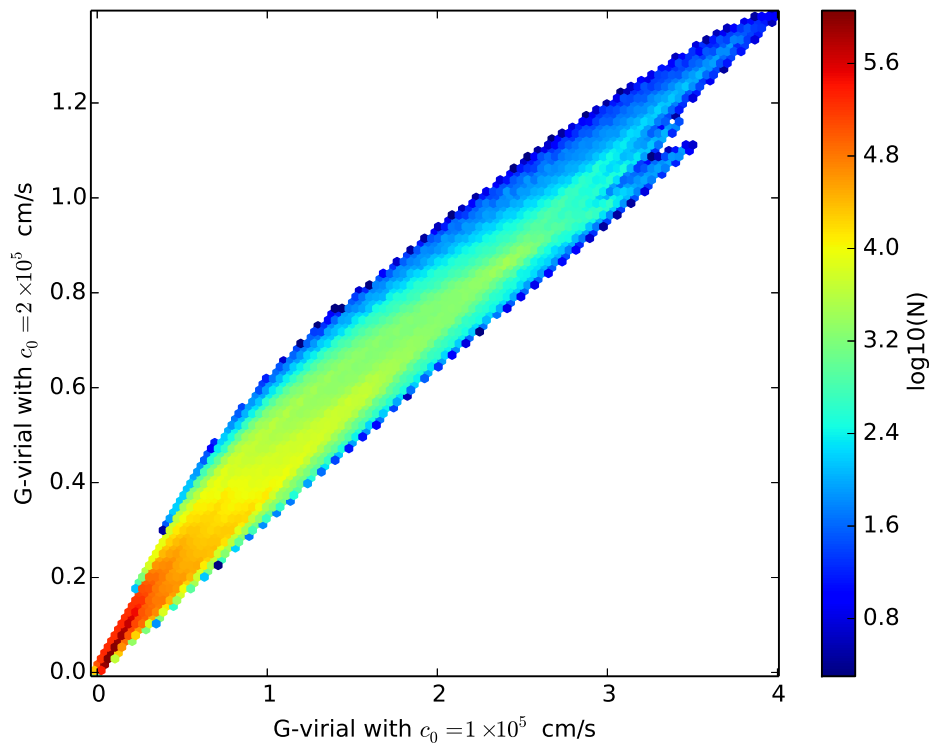
FIGURE 3.15: A comparison of `G-virial` map of the Ophiuchus molecular cloud under different c_0. The horizontal axis is the `G-virial` calculated assuming $c_0 = 1$ km/s and the vertical axis is the `G-virial` calculated assuming $c_0 = 2$ km/s. Grayscale image stands for the number of pixels that fall into each bin.
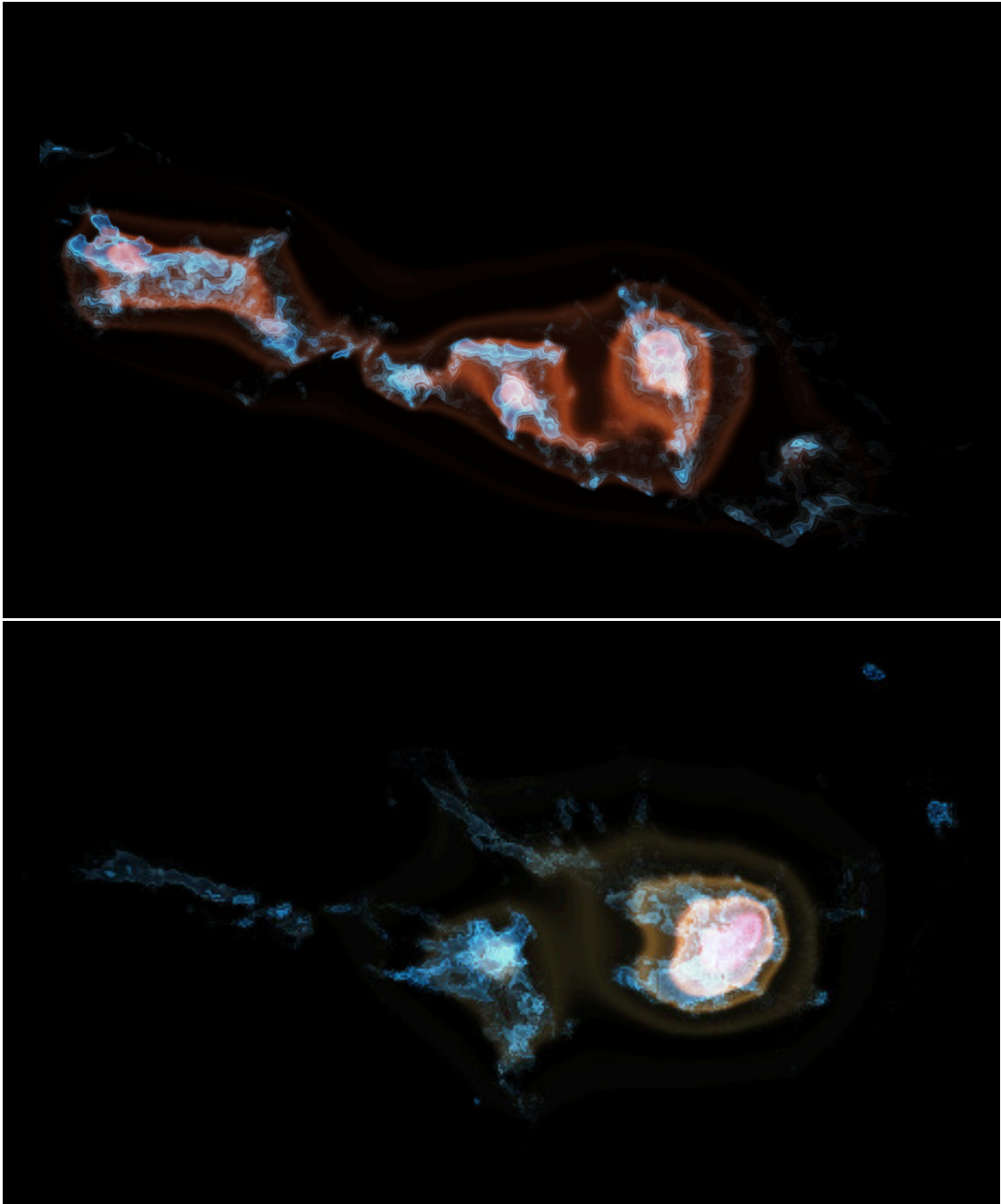
FIGURE 3.16: Volume rendering representations of the ^{13}CO(1-0) emission and the corresponding `G-virial` map. The upper panel shows the result from the Perseus molecular cloud and the lower panel shows the result from the Ophiuchus molecular cloud. The blue color stands for ^{13}CO(1-0) emission and the red and orange colors stand for the `G-virial`. Both clouds are projected along the velocity direction. For the Persues molecular cloud, the iso-surfaces of ^{13}CO(1-0) emission start from 0.3 K and increase in a step of 0.64 K. The contours of the `G-virial` starts from 1.2 and increase in a step of 0.8. For the Ophiuchus molecular cloud, the contours of ^{13}CO(1-0) emission start from 0.3 K and increase in a step of 1.24 K. The contours of the `G-virial` starts from 1.2 and increase in a step of 0.8.

Chapter 4

Protostellar outflow as an entrainment phenomenon [1]

4.1 Introduction

Protostellar outflow is a prominent process that is intimately connected with the formation of stars. When a protostar accretes gas from its surroundings, it produces a powerful wind or jet. As the wind or jet material moves away from the protostar, ambient gas is entrained. The mixture of the wind or jet gas and the ambient gas will move away from the protostar, forming a so-called molecular outflow. In observations of the star-forming regions with rotational transitions of molecules such as CO, outflows can be easily identified from the high-velocity part of the emission line. The physical size of the molecular outflow is about a parsec. The typical velocity of the outflowing gas is about tens of kilometers per second, and the morphology of the outflow can be collimated (jet-like) or less collimated (conical-shaped), or a combination of both.

Many of the outflows exhibit as conical-shaped geometry [Shepherd et al., 1998, Lee et al., 2000, Arce & Sargent, 2006, Qiu et al., 2009, Ren et al., 2011, Cyganowski et al., 2011]. It is still unclear how these conical-shaped outflows form. Models that can explain conical-shaped outflows include the wind-driven shell model [Shu et al., 1991, Li & Shu, 1996, Lee et al., 2001] and the circulation model [Fiege & Henriksen, 1996, Lery et al., 1999]. In the wind-driven shell model, the wind from the protostar blows into the ambient medium, and a shell forms at the interface between the wind and the ambient gas. The shell absorbs momentum from the wind and expands. The outflowing material consists of the ambient gas swept up by the shell. In the circulation model, the

---

[1]This chapter has been published as "Turbulent entrainment origin of protostellar outflows", Li, G.-X., Qiu, K., Wyrowski, F., & Menten, K. 2013, A&A, 559, A23.

gas circulates around the protostar in a quadrupolar way, and it is the gas that moves outward in this circulation cycle that constitutes the outflow.

Neither of these models properly addresses the role of supersonic turbulent motion in the formation and evolution of the protostellar outflows. This might be because the importance of supersonic turbulent motion in star-forming regions was not generally recognized when these models were proposed. Today, it is widely recognized that the interstellar medium where stars form is turbulent, this turbulence is supersonic in most star-forming regions [Larson, 1981, Ballesteros-Paredes et al., 2007]. This will bring about serious physical discrepancies to both models. For the wind-driven shell model, the turbulent ram-pressure (expressed as $p_{\text{turb}} \sim \rho \sigma_{\text{turb}}^2$) is much higher than the thermal pressure, and is often comparable to the ram-pressure of the wind (expressed as $p_{\text{wind}} \sim \rho_{\text{wind}} v_{\text{wind}}^2$, see section §4.4). Therefore the wind-driven shell model is no longer valid since the physical condition cannot allow the shell to expand for long. The circulation model is also questionable when the interstellar medium is turbulent, because turbulent motion is expected to significantly distort the motion of gas, making the initial condition unfavourable for circulation to occur.

The kinematic structures of the outflows are only poorly reproduced by the previous models. Mappings of outflows with molecular lines reveal the spatial and velocity structures of the outflowing gas, which is crucial to test the models. It is found that the outflows ubiquitously exhibit a broad line width at different positions. Seen from position-velocity diagrams, the outflowing gas exhibits a wide velocity spread at one given position (§4.3). This is difficult to understand in the context of the widely accepted wind-driven shell model [Shu et al., 1991, Li & Shu, 1996, Lee et al., 2001], because the shell swept by the wind will expand according to the **"Hubble law"**, and the expansion speed of the shell is higher in the directions where the shell has progressed further. Seen from the position-velocity diagram , we can identify two velocity components at one given position. One component comes from the front wall of the outflow cavity, the other from the back wall of the outflow cavity [Lee et al., 2000]. However, observations found that at one single position, there is only one broad component [e.g. Qiu et al., 2009].

It is observationally found that the opening angles of outflows evolve significantly during their lifetimes [Beuther & Shepherd, 2005, Arce & Sargent, 2006]. While usually interpreted as the evolution of the wind-envelope interaction [Arce & Sargent, 2006], a comprehensive treatment of this interaction in the presence of the turbulent motion of the ambient gas is still lacking.

In this study, we theoretically investigate the formation of outflows from the turbulent

mixing between the wind from the protostar and the *turbulent* ambient gas. In our *wind-driven turbulent entrainment* model, the ram-pressure of the wind and the turbulent ram-pressure of the ambient gas (envelope) establish hydrostatic balance, and the outflow is the gas contained in the turbulent entrainment layer between the wind and the turbulent envelope. In §4.2 we present the basic physical picture, followed by a detailed description of our model. In §4.3 we compare the image and position-velocity diagram from our model with existing observations. In §4.4.1 and 4.4.2 we offer a unified framework to understand outflows from low-mass protostars and high-mass protostars as well as AGN-driven outflows. We also discuss the possibility that the wind is not strong enough to push the envelope, and predict the existence of dwarf outflows in these situations (§4.4.3). In §4.5 we conclude.

Recently, the interaction between a wind and a turbulent core has been studied with radiation-hydrodynamic simulations [Offner et al., 2011], focusing on how the physical structure suggested by the simulations can be reproduced through millimetre-wavelength aperture synthesis observations. In this work, we present an explicit treatment of the mixing entrainment process, and study the consequences of this turbulent entrainment in producing protostellar outflows.

4.2 Model

In our model, the outflowing gas is contained in the turbulent entrainment layer that develops between the wind and the envelope (Fig. 4.1). The wind is collimated, and its strength reaches a maximum around the z-axis of Fig. 4.1. The wind is launched in a region close to the protostar due to magnetic centrifugal forces. This wind is generally collimated and exhibits universal asymptotic collimation properties [Shu et al., 1995, Matzner & McKee, 1999]. The wind evacuates a cavity and is confined mainly inside it. The ambient matter (envelope) is still present in regions father away from the outflow axis. The outflow layer lies between the cavity and the ambient matter. The outflow is generated by the interaction between the wind and the envelope.

The turbulent nature of the interstellar medium has been recognized for years. It has been suggested that it plays an important role in regulating the star formation processes inside molecular clouds [Plume et al., 1997, Krumholz & McKee, 2005, Ballesteros-Paredes et al., 2007]. Molecular outflows have been suggested as major drivers of this turbulent motion [Matzner, 2007, Nakamura & Li, 2007]. The role of turbulence in the formation and evolution of the molecular outflow remains unexplored. It is easy to show (§4.4.1) that at physical scales of about a parsec (which is the typical physical scale
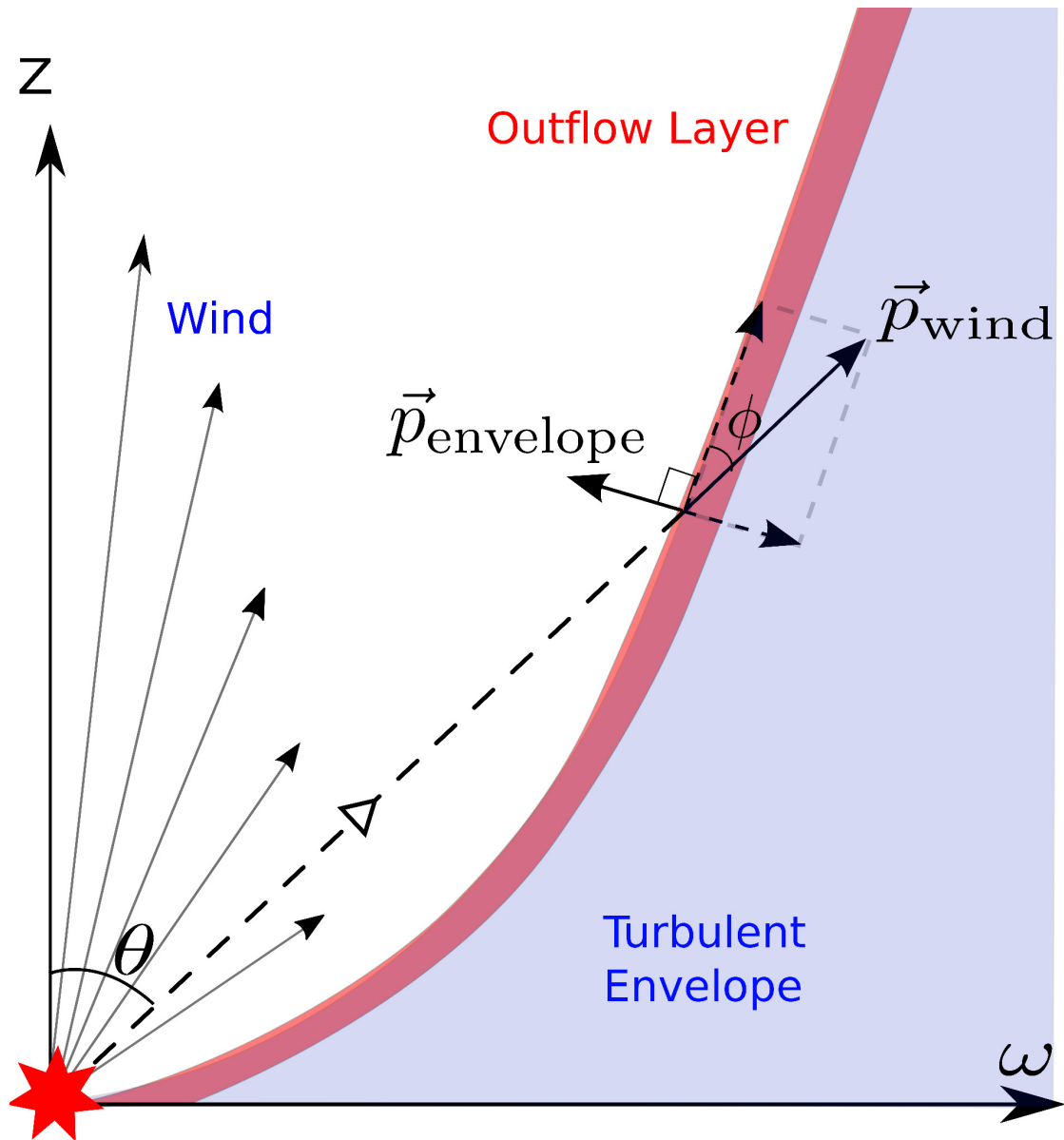
FIGURE 4.1: Cartoon showing the basic structure of our model. The outflow (red region) lies between the wind and the envelope. Arrows ($\vec{p}_{\mathrm{wind}}$ and $\vec{p}_{\mathrm{envelope}}$) denote the ram-pressure of the wind and the envelope. With **wind** we denote the cavity evacuated by the wind, with **turbulent envelope** we denote the turbulent envelope, and with **outflow layer** we denote the layer which contains the mixture of gas from the wind and gas from the envelope.

of the outflow), turbulence dominates the dynamical properties of the medium. It is therefore necessary to consider the roles of turbulence consistently.

In this study, we propose that the structure of the outflow is determined by the following processes: First, we propose that the wind and the envelope will establish hydrostatic balance, and this balance will determine the shape of the outflow. According to Fig. 4.1, the wind has a ram-pressure that points away from the protostar (see $\vec{p}_{\text{wind}}$ in Fig. 4.1, where $|\vec{p}_{\text{wind}}| \equiv p_{\text{wind}} = \rho_{\text{wind}} v_{\text{wind}}^2$), and the envelope has a ram-pressure that is perpendicular to the wall of the outflow cavity ($\vec{p}_{\text{envelope}}$). According to the balance of these two forces, the shape of the outflow cavity can be numerically calculated (§4.2.2).

Second, we propose that a turbulent mixing layer develops between the wind and the envelope. When the wind moves relative to the envelope, Kelvin-Helmholtz instability occurs. When the instability saturates, a mixing layer establishes. This mixing layer grows as it absorbs mass and momentum from the envelope and the wind. The mass and momentum of the mixing layer is determined by mass and momentum conservations (§4.2.3,4.2.4).

Turbulence plays an important role in both processes. First, turbulence influences the turbulent ram-pressure of the envelope, and in turn influences the pressure balance between the wind and the envelope. Therefore, turbulence influences the shape of the outflow (§4.2.2). Second, turbulence changes the mixing process that occurs between the wind and the envelope. Therefore, it influences the mass and velocity of the outflow (§4.2.3,4.2.4).

The structure of the molecular cloud is inhomogeneous at a variety of scales. On a parsec scale, millimeter/sub-millimeter studies suggest that the density distribution of molecular gas around the protostar is consistent with being spherically symmetric and can be described as a power-law $\rho \sim r^\gamma$ [e.g. Keto & Zhang, 2010, Longmore et al., 2011].

Following these author we parametrized the density distribution of the envelope as

$$\frac{\rho}{\rho_0} = \left(\frac{r}{r_0}\right)^{-k_\rho} . \tag{4.1}$$

By assuming hydrostatic equilibrium, Equation 4.1 leads to the distribution of the turbulent velocity σ_{turb} that takes the form [McLaughlin & Pudritz, 1996, McKee & Holliman, 1999, McKee & Tan, 2003]

$$\frac{\sigma_{\text{turb}}}{\sigma_0} = \left(\frac{r}{r_0}\right)^{1-k_\rho/2} . \tag{4.2}$$

Parameter	Definition	Fiducial Value
Envelope Parameters		
k_ρ	Power-law index for density distribution	1.785
k_σ	Power-law index for the distribution of the turbulent velocity	0.1075
r_0	Characteristic radius to specify the values of physical quantities	0.3 pc
ρ_0	Density at the characteristic radius	3.35×10^{-19} g cm^{-3}
σ_0	Velocity dispersion at the characteristic radius	4.08 km s^{-1}
Wind Parameters		
v_{wind}	Velocity of the wind	600 km s^{-1}
$\dot{M}_{\text{wind}}$	Mass-loss rate of the wind	0.5, 1, 1.5 $\times 10^{-3}$ M$_\odot$ yr^{-1}
Other parameters		
α	Entrainment Efficiency	0.1
β	Wind Efficiency	0.3
M_*	Stellar Mass	10 M$_\odot$
t	Age of outflow	1×10^4 yr

TABLE 4.1: Summary of model parameters.

The power-law index k_ρ in Equation 4.1 is set according to the observational studies by Beuther et al. [2002], Mueller et al. [2002], Keto & Zhang [2010], Longmore et al. [2011]. In our canonical model, consulting the results in Longmore et al. [2011] we set a density of 3.35×10^{-19} g cm^{-3} at $r = 0.3$ pc for Equation 4.1. The parameter values are summarized in Table 4.1. These parameters are set to be typical of high-mass protostars [e.g. Keto & Zhang, 2010, Longmore et al., 2011]. Furthermore, since our model is scale-free, the results can be scaled to different situations (§4.4.4).

4.2.1   Wind from the embedded protostar

In our model, the outflow consists of the envelope gas entrained by the wind. To specify the wind, we followed the formalism used by Lee et al. [2001]. In a spherical coordinate system (r, θ, ϕ), Shu et al. [1995] have shown that the radial velocity of an X-wind is roughly constant, and the density distribution takes the form

$$\rho_{\text{wind}} \sim \frac{1}{r^2 \sin^2 \theta} \; . \tag{4.3}$$

Equation 4.3 is shown to be valid not only for the X-wind model, but also for more general force-free winds [Ostriker, 1997, Matzner & McKee, 1999]. It has been shown that the terminal velocity of the wind v_{wind} is approximately the same at different angles [Najita & Shu, 1994]. In our modelling, the wind is parametrized as

$$
\begin{aligned}
\rho_{\text{wind}} &= \rho_{\text{norm}} \frac{1}{r^2 (\sin^2 \theta + \epsilon)} \\
v_{\text{wind}} &= v_t \; ,
\end{aligned}
\tag{4.4}
$$

where $\epsilon = 0.01$ is added to avoid the singularity at the pole $(\theta = 0)$ [Lee et al., 2001]. v_t is the terminal velocity of the wind, and ρ_{norm} is related to the wind mass-loss rate (rate at which the wind carries matter from the protostar, $\dot{M}_{\text{wind}}$) by mass conservation,

$$\int_0^\pi 2\pi r^2 \sin \theta \rho_{\text{wind}}(r) v_{\text{wind}} \mathrm{d}\theta = \dot{M}_{\text{wind}} \; . \tag{4.5}$$

We assumed that the wind has a terminal velocity of 600 km s^{-1} [similar to Cunningham et al., 2005]. The values for the mass-loss rate were chosen to match the values found by Beuther et al. [2004]. Parameters for the wind are listed in Table 4.1.

In principle, both the mass-loss rate of the wind and the density distribution of the envelope should evolve during the star formation process. However for simplicity, we only considered an envelope with a fixed density distribution and a wind with a fixed mass-loss rate. In practice, the timescale for local collapse is proportional to $\rho^{-1/2}$. Therefore, the central region where the protostars form evolves faster than the outer envelope, the density structure of the envelope evolves more slowly than the evolution of the wind mass-loss rate during the lifetime of the outflow.
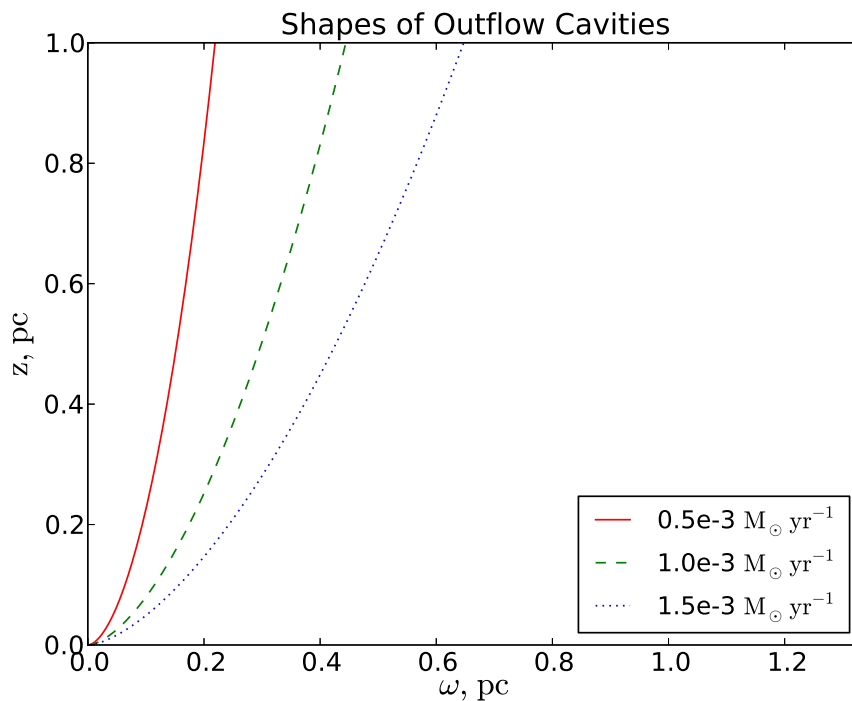
FIGURE 4.2: Shapes of outflow cavities calculated for models with different wind mass-loss rates. The parameters are taken from Table **??**. See §4.2.2 for details.

4.2.2 Shape of the outflow cavity

The shape of the outflow cavity is determined by the balance of the ram-pressure of the wind and the pressure of the envelope perpendicular to the outflow cavity wall (see Fig. 4.1). The magnitude of $\vec{p}_{\text{wind}}$ is $p_{\text{wind}} = \rho_{\text{wind}} v_{\text{wind}}^2$, and the magnitude of the ram-pressure vector $\vec{p}_{\text{envelope}}$ is $p_{\text{envelope}} = \rho_{\text{envelope}} \sigma_{\text{turb}}^2$. Projected perpendicular to the edge of the outflow cavity, the magnitude of the wind pressure is $|\vec{p}_{\text{wind}}| \sin \phi$ and the magnitude of the envelope pressure is $|\vec{p}_{\text{envelope}}|$ (Figure 4.1). The *pressure balance* perpendicular to the wall of the outflow cavity can then be written as

$$p_{\text{wind}} \sin \phi = p_{\text{envelope}} \ . \tag{4.6}$$

Along the cavity wall, no pressure balance is established, and the wind contributes its momentum to the outflow (see § 4.2.3).

Here we used cylindrical coordinates (ω, ϕ, z) for convenience. The polar angle θ is specified as (Figure 4.1)

$$\theta = \frac{\pi}{2} - \arctan\left(\frac{z}{\omega}\right) , \tag{4.7}$$

and the angle between the cavity wall and the z axis is specified as

$$\theta_{\text{wall}} = \frac{\pi}{2} - \arctan\left(\frac{\text{d}z}{\text{d}\omega}\right). \tag{4.8}$$

This gives a value ϕ of (Fig. 4.1)

$$\phi = \theta - \theta_{\text{wall}} = \arctan\left(\frac{\text{d}z}{\text{d}\omega}\right) - \arctan\left(\frac{z}{\omega}\right). \tag{4.9}$$

.

Combining Equations 4.6, 4.7, 4.8, and 4.9 gives

$$\frac{\text{d}z}{\text{d}\omega} = \tan\phi = \tan\left(\arctan\left(\frac{z}{\omega}\right) + \arcsin\frac{p_{\text{envelope}}}{p_{\text{wind}}}\right). \tag{4.10}$$

Equation 4.10 determines the shape of the outflow cavity. It is a first-order differential equation and can be solved numerically. We imposed the boundary condition $\omega = 4.5 \times 10^{15}$ cm at $z = 0$, which is similar to those used by Parkin et al. [2009]. The results are not sensitive to the choice of this boundary condition.

In deriving Equation 4.10, we have neglected the effect of centrifugal force. As will be shown in section 4.6.1, centrifugal force is not significant in our case.

Using Equation 4.10, we calculated the shapes of the outflow cavities for winds of different mass-loss rates. The results are shown in Fig. 4.2. It is clear that the opening angle of the outflow depends on the strength of the wind: a stronger wind leads to a less collimated outflow.

Observationally, the opening angle of the outflow evolves during the evolution of the protostar [Arce & Sargent, 2006, Beuther & Shepherd, 2005]. This is interpreted as the evolution of the wind-envelope interaction [Arce & Sargent, 2006]. However, according to the widely accepted wind-driven shell model, the opening angle of the outflow should be fixed as the wind collimation is fixed and the density structure of the envelope does not evolve much [Lee et al., 2001]. How the evolution of the wind-envelope interaction changes the collimation of the outflow is thus unclear.

According to our model, the outflow opening angle is determined by the force balance between the wind and the envelope. With the wind strength increases or the envelope becomes less turbulent, the opening angle of the outflow becomes larger, and the outflow tends to decollimate. Our model provides a quantitative explanation of the de-collimation of the outflow in the context of the wind-envelope interaction.

Turbulence in the envelope plays a vital role in our model: the shape of the outflow cavity is determined by the hydrostatic balance between the wind and the envelope, and an increase in the strength of the wind can decrease the collimation of the outflow, while an increase of the turbulence in the envelope can increase the collimation of the outflow. Turbulence helps to *collimate* the outflow.

4.2.3   Mass entrainment of the outflow layer

As discussed in §4.1, the growth of the outflow depends on the way matter is entrained into it.

The key parameter that characterizes the mass entrainment process is the local mass entrainment rate, which is the amount of matter entrained per given time interval per surface area. The entrainment rate $\dot{m}$ can therefore be defined as

$$\dot{m} = \frac{M_{\text{entrained}}}{\text{d}s \times \text{d}t} \ , \tag{4.11}$$

where $M_{\text{entrained}}$ is the amount of gas entrained, ds represents the unit surface area and dt represents the time interval. The entrainment rate depend on the density and the velocity involved in the entrainment process. Therefore, the general form of the entrainment rate can be formulated as

$$\dot{m} = f_{\text{entrainment}}(c_s, \sigma_{\text{turb}}, v_{\text{shear}}) \times \rho_{\text{envelope}} \ , \tag{4.12}$$

where c_s, σ_{turb} and v_{shear} are the sound speed, turbulent speed and the velocity difference between the shearing layer and the envelope, and ρ_{envelope} is the density of the envelope.

The factor $f_{\text{entrainment}}$ takes into account the effect of different speeds on the entrainment rate, and has the dimension of the velocity. In our case, the relative speed between the outflow and the envelope v_{shear} is much higher than the velocity dispersion of the envelope σ_{turb}, and σ_{turb} is higher than the sound speed ($v_{\text{shear}} >> \sigma_{\text{turb}} > c_s$).

The entrainment process is driven by the shearing motion and limited by the transport properties of the medium. The shearing motion is characterized by v_{shear} and the transport process is characterized by σ_{turb} and c_s. As $v_{\text{shear}} >> \sigma_{\text{turb}}$, the entrainment rate is limited by the transport and is determined by a combination of σ_{turb} and c_s. In a turbulent medium, turbulence dominates the transport. Therefore, in our model, $f_{\text{entrainment}}$ is determined by turbulence. We thus take

$$f_{\text{entrainment}} = \alpha \sigma_{\text{turb}} \ , \tag{4.13}$$

where α is a dimensionless factor that characterizes the efficiency of the entrainment process. We therefore parametrized the entrainment rate in the presence of turbulent motion as

$$\dot{m} = \alpha \sigma_{\text{turb}} \rho_{\text{envelope}} \ , \tag{4.14}$$

where σ_{turb} is the characteristic velocity of turbulent motion in the medium. We assume $\alpha = 0.1$ in this work.

Historically, turbulent mixing has long been proposed as a mean of entraining mass into the outflow [e.g. Canto & Raga, 1991, Watson et al., 2004]. However, these models are doubted because the entrainment rate is far too small to account for the actual mass the outflow [Churchwell, 1997]. Realizing the importance of turbulence for enhancing the mass and momentum transport, we here propose that the argument by Churchwell [1997] no longer holds in our cases because turbulent mixing can be significantly enhanced when the ambient medium is turbulent.

4.2.4   Mass and momentum conservation in the entrainment layer

Based on the assumption that the outflow gas is the entrained envelope material, we formulate the equations that govern the evolution of the outflow. The geometry of the outflow is illustrated in Fig. 4.3. We defined the x-axis to be along the wall of the outflow cavity and v_{x} as the average velocity of the outflow along the x-axis. By doing this, our x-axis is no longer a straight line. We used this construction for simplicity. ω is the same as illustrated in Fig. 4.1, which gives a circumference l_c of

$$l_{\text{c}} = 2\pi\omega \ . \tag{4.15}$$

In Fig. 4.3, ρ is the average density and d is the geometrical thickness of the outflow layer. In our case, the outflow is geometrically thin ($d \ll l$).

Σ is the integrated density, which is defined as

$$\Sigma = l_{\text{c}}\rho = 2\pi\omega\rho d \ , \tag{4.16}$$

and W is the integrated momentum, which is defined as

$$W = l_{\text{c}}\rho v_x = 2\pi\omega\rho v_x d \ , \tag{4.17}$$

$$\Sigma = 2\pi\omega\rho d$$
$$W = 2\pi\omega\rho v_{\mathrm{x}}d$$
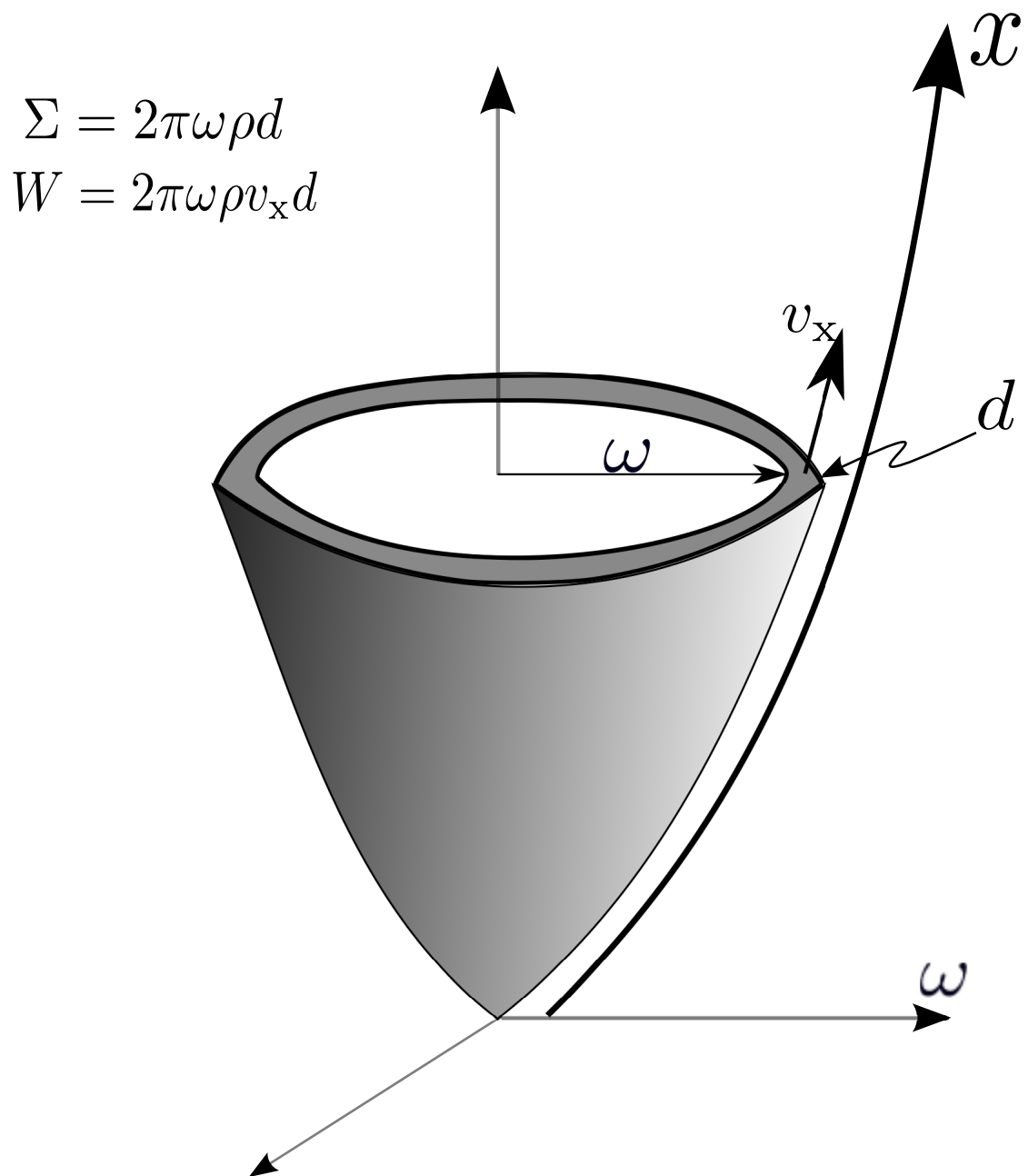
FIGURE 4.3: Cartoon illustrating the geometry of the outflow layer and the definition of physical quantities in §4.2.4 .

where v_x is the average outflow velocity along the outflow wall. Note that here d is introduced for convenience. At a given position, we calculated Σ and W first. d can then be evaluated as $d = \Sigma/(2\pi\omega\rho)$.

The equations of motion of the outflow layer describe the conservation of the mass and the momentum,

$$\frac{\partial}{\partial t}\Sigma(x,t) + \frac{\partial}{\partial x}\big(v_x(x,t)\Sigma(x,t)\big) = S_\Sigma(x) \tag{4.18}$$

$$\frac{\partial}{\partial t}W(x,t) + \frac{\partial}{\partial x}\big(v_x(x,t)W(x,t)\big) = S_W(x,\Sigma) , \tag{4.19}$$

where $W = v_x\Sigma$.

To solve it, we need the initial conditions $\Sigma(x, t = 0)$ and $W(x, t = 0)$.

We still need to specify the source terms S_Σ and S_W. According to the geometry in Fig. 4.1, S_Σ can be expressed as the sum of the mass flow from the wind and the mass flow from the envelope,

$$S_\Sigma = S_{\Sigma\mathrm{wind}} + S_{\Sigma\mathrm{envelope}} , \tag{4.20}$$

where

$$S_{\Sigma\mathrm{wind}} = \rho_{\mathrm{wind}}v_{\mathrm{wind}}\sin\phi \times 2\pi\omega \times \beta \tag{4.21}$$

and according to Equation 4.14,

$$S_{\Sigma\mathrm{envelope}} = \alpha\rho_{\mathrm{envelope}}\sigma_{\mathrm{turb}} \times 2\pi\omega . \tag{4.22}$$

Here, $S_{\Sigma\mathrm{wind}} \ll S_{\Sigma\mathrm{envelope}}$. Most of the mass in the outflow comes from the envelope.

S_W is the source term for the integrated momentum. S_W consists of the momentum injection by the wind, as well as the change of the momentum due to gravity. S_W can then be expressed as,

$$\begin{aligned} S_W &= S_{W\mathrm{wind}} + S_{W\mathrm{gravity}} \\ &= \rho_{\mathrm{wind}}v_{\mathrm{wind}}^2\sin\phi\cos\phi \times 2\pi\omega \times \beta + \Sigma g , \end{aligned} \tag{4.23}$$

where $g = GM_*/r^2 \cos\phi$ is the acceleration due to gravity. Here, M_* is the stellar mass (10 $M_\odot$), and $\cos\phi$ comes from projecting the gravity onto the wall of the outflow

cavity. β is the wind efficiency. It characterizes the efficiency with which the mixing layer absorbs mass and momentum from the wind. We took 0.3 as its fiducial value.

4.2.5 Local linear growth regime

Here we make an order-of-magnitude analysis of Equations 4.18. The first terms are the transient terms $\frac{\partial}{\partial t} \times P$. The second terms are the advection terms, $\frac{\partial}{\partial x}(v_x \times P)$, and the third terms are the source terms S_P. Here, P can be either Σ or W. If the outflow has initial mass and momentum distribution $P_0 = \Sigma_0$ or W_0, the mass/momentum accumulation timescales can be written as

$$t_{\text{accumulation}} = P_0/S_P \ . \tag{4.24}$$

and the advection timescales can be written as

$$t_{\text{advection}} = L/v_x \ . \tag{4.25}$$

Here, L is the physical scale of the outflow, which is about 1 parsec.

The mass/momentum accumulation timescale is dependent on the initial mass and momentum Σ_0 and W_0. If the majority of the mass and momentum of the outflow comes from the turbulence mixing process, Σ_0 and W_0 should be insignificant, therefore $t_{\text{accumulation}}$ is expected to be very short. Because we lack the knowledge on the initial mass and momentum distribution of the outflow, we assumed that the majority of the outflow mass and momentum comes from the turbulence mixing process. This assumption is valid as long as the outflow age is larger than the accumulation timescale $t_{\text{accumulation}}$ (Equation 4.24) is long. We studied the behaviour of Equations 4.18 by analysing the importance of different terms. For simplicity, we neglected the momentum added to the outflow due to self-gravity, therefore $W(x, \Sigma)$ in Equations 4.18 can be approximated as $W(x)$.

The advection timescale $t_{\text{advection}}$ is the time required for matter to travel throughout the outflow. If the outflow has an age of t_{outflow}, the transient term is

$$\text{TransientTerm} = \frac{\partial P}{\partial t} \sim \frac{P}{t_{\text{outflow}}} \ , \tag{4.26}$$

and the advection term is

$$\text{AdvectionTerm} = \frac{\partial v_x P}{\partial x} \sim \frac{v_x P}{L} \sim \frac{P}{t_{\text{advection}}} \ . \tag{4.27}$$

If we take the ratio between the advection term and the transient term, we have

$$\frac{\text{AdvectionTerm}}{\text{TransientTerm}} \sim \frac{v_x/L}{1/t_{\text{outflow}}} \sim \frac{t_{\text{outflow}}}{t_{\text{advection}}} \; , \tag{4.28}$$

where by definition $t_{\text{advection}} = L/v$. In our typical case, $t_{\text{outflow}} = 1 \times 10^4\text{yr}$ and $t_{\text{advection}} \sim L/v_x \sim 1\,\text{pc}/30\,\text{km s}^{-1} \sim 1 \times 10^5\text{yr}$. $t_{\text{outflow}} < t_{\text{advection}}$, therefore advection is not important in the whole outflow. In this case, the advection effect can smooth out the density variations at the small scale, but can not alternate the structure of the whole outflow significantly. This is also true for the outflow from the class 0 low-mass protostars [Arce et al., 2007].

If the age of the outflow is small ($t_{\text{outflow}} << t_{\text{advection}}$), as it is most cases, we can neglect the advection terms in Equations 4.18, therefore we have

$$\frac{\partial}{\partial t}\Sigma(x,t) = S_\Sigma(x) \tag{4.29}$$

$$\frac{\partial}{\partial t}W(x,t) = S_{\text{W}}(x) \; . \tag{4.30}$$

The surface density of the outflow can then be calculated as

$$\Sigma(x,t) = S_\Sigma(x) \times t_{\text{outflow}} \; , \tag{4.31}$$

and the velocity of the outflow can be calculated as

$$v_{\text{x}}(x,t) = \frac{S_W}{S_\Sigma} \; . \tag{4.32}$$

In this case, the velocity profile of the outflow is fixed and the surface density of the outflow grows linearly with time.

4.2.6 Advection-term-dominated regime

For the aged low-mass outflows (e.g outflows with $t \sim 10^7$ yr), we have $t_{\text{outflow}} \sim t_{\text{advection}}$, and the advection effect can alter the mass distribution of the outflow significantly. Neglecting the transient terms in Equations 4.18, we have

$$\frac{\partial}{\partial x}\big(v_x(x,t)\Sigma(x,t)\big) = S_\Sigma(x) \tag{4.33}$$

$$\frac{\partial}{\partial x}\big(v_x(x,t)W(x,t)\big) = S_{\text{W}}(x) \; , \tag{4.34}$$

hence

$$v_x = \frac{\int S_W \, dx}{\int S_\Sigma \, dx} \tag{4.35}$$

$$\Sigma = \frac{\left(\int S_\Sigma \, dx \right)^2}{\int S_W \, dx} \ . \tag{4.36}$$

Here, both the velocity and the surface density exhibit stationary profiles. By comparing Equation 4.31 and 4.32 with Equation 4.35, we find that when the outflow age is high, the advection term dominates the transient term, which prevents the outflow surface density from growing to infinity.

4.2.7 Role of gravity

Here we consider the role of the gravity term in the structure of the outflow. According to Equation 4.23, the contribution of gravity is quantified by the ratio

$$f_{\text{gravity}} = \frac{\Sigma g}{\rho_{\text{wind}} v_{\text{wind}}^2 \times 2\pi\omega \times \beta} \sim \frac{\rho d 2\pi\omega g\alpha}{\rho_{\text{wind}} \times v_{\text{wind}}^2 \times 2\pi\omega\beta} \ , \tag{4.37}$$

where $d = \sigma t \alpha$ is used. Here, d is the thickness of the outflow, α is the entrainment efficiency, σ is the velocity dispersion of the envelope and t is the outflow age. From this we have

$$f_{\text{gravity}} = \frac{gt}{\sigma} \times \frac{\alpha}{\beta} \ . \tag{4.38}$$

Here, σ is the velocity dispersion of the envelope, t is the age of the outflow, and $g \sim GM_*/r^2$ is the local gravity. Since $g \sim r^{-2}$, gravity will be important at regions close to the protostar, and it will be important when the mass of the outflow has grown significantly.

Considering the inner region of the outflow, we have $M_* = 10 M_\odot$, $r = 0.1$ pc and $t = 10^4$ yr. Therefore, $f_{\text{gravity}} \sim 10^{-2}$ and the gravity from the protostar is negligible. However, at regions closer to the protostar, gravity must play an important role in slowing down the outflow.

4.2.8 Numerical results

To illustrate how the mass and the momentum of the outflow grows with time, we assume a static envelope and a wind with a constant mass-loss rate and followed the evolution of the entrainment layer by solving Equations 4.18 – 4.23 numerically. The cavity shapes

are calculated in §4.2.2. At $x = 0$, we imposed

$$\frac{\partial \Sigma}{\partial x} = 0 \tag{4.39}$$

$$\frac{\partial W}{\partial x} = 0 \, , \tag{4.40}$$

and set the initial condition so that

$$\Sigma(x) = S_\Sigma \Delta t_0 \tag{4.41}$$

$$v_x(x) = 1 \times 10^{-4} \text{ cm s}^{-1} \, , \tag{4.42}$$

where $\Delta t_0 = 100 \ yr$. The equations are solved using FiPy (J. E. Guyer, D. Wheeler & J. A. Warren) [2].

We are mainly interested in the transient-term-dominated regime, since because this regime is relevant to all high-mass protostellar outflows and the majority of the young low-mass protostellar outflows.

In Fig. 4.4, we plot the results from our calculations for a realistic 10^4 yr outflow and unrealistically old 10^7 yr outflow. In our 10^4 yr outflow, the numerical solution agrees quite well with the analytical solutions (§4.2.5). At small radius, the numerical solutions show lower velocity. This is because the matter in regions close to the protostar is slowed down by the gravity from the protostar.

We also plot the results of an outflow with an unrealistically long lifetime of 10^7 yr. Because here gravity plays a much more significant role in slowing down the outflow (§4.2.7), the velocity of the outflow at the central part of the outflow becomes much lower.

In most cases, the effect of gravity is negligible in large portions of the outflow, the analytical solutions can be taken as good approximations to the structure of the outflow. However, it is difficult for the outflow to enter the advection-dominated regime, since here gravity tends to dominate the velocity structure of the outflow and to slow down the outward motion before advection is able to change the structure of the whole outflow significantly.

The final state we obtained from solving the equations of mass and momentum conservation in the *local linear growth regime* is representative of the real structure of the outflow, as long as the mass and momentum added to the outflow is much larger than the initial mass and momentum of the outflow. If the strength of the wind or the structure of the envelope changed during the evolution of the system, the final state of the outflow will

---

[2]Avaliable at http://www.ctcms.nist.gov/fipy/
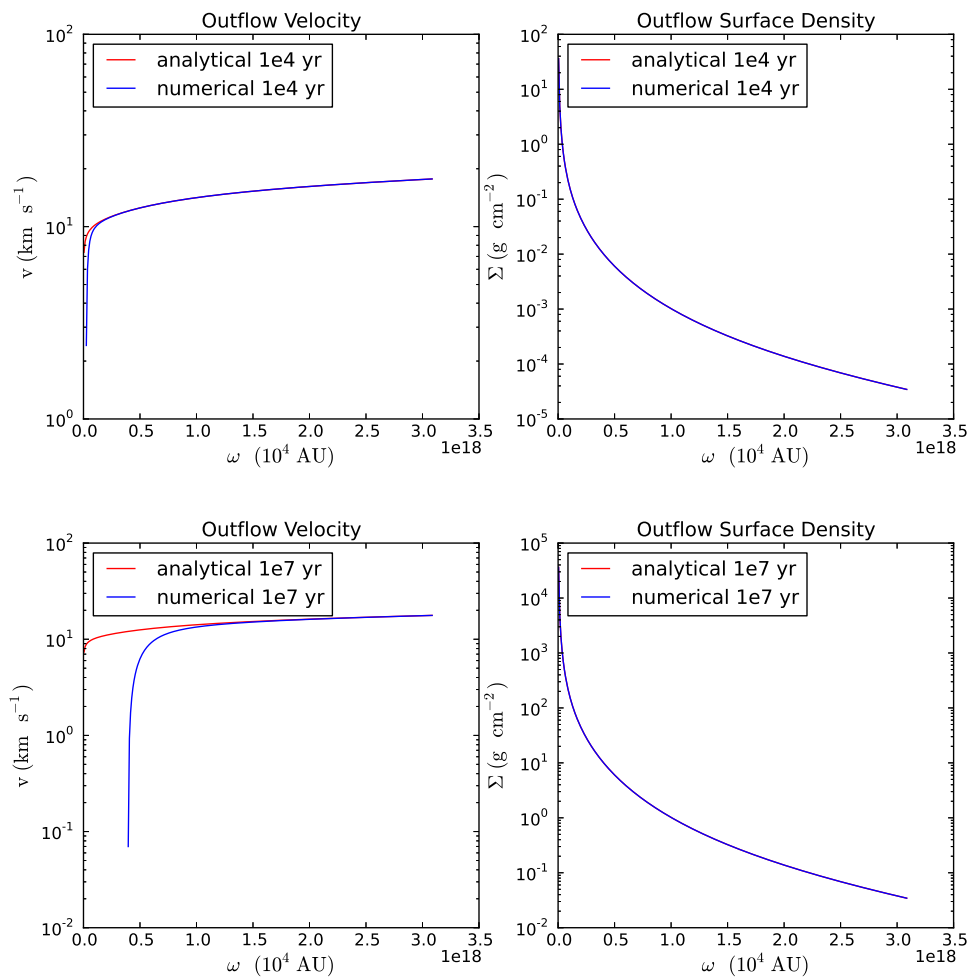
FIGURE 4.4: Velocity and surface density distribution of the outflow calculated by solving Equations 4.18. The blue lines are the numerical results and the red lines are results calculated by assuming the local conservation of energy and momentum (§4.2.5). The upper panels are the results for a 10^4 yr outflow. The lower panels are the results for an unrealistically old (10^7 yr) outflow. At smaller radii, the deviation of the numerical solutions from the analytical solutions are caused by the gravity term in Eq. 4.23.

change accordingly. Therefore, the system will evolve towards a new state, and the time for this evolution to take place is again the accumulation timescale (Equation 4.24). The older the outflow becomes, the more difficult it is for the outflow to relax to the new state.

In our present work, we assumed that the wind and envelope remain stationary. Our solution is valid when the structure of the wind and the structure of the envelope change slowly. Since detailed observations of the way in which the wind and envelope evolve are currently unavailable, we assume this simplicity. If the wind and the envelope both evolve significantly, it is still possible to calculate the structure of the outflow by making some modifications to the framework presented.
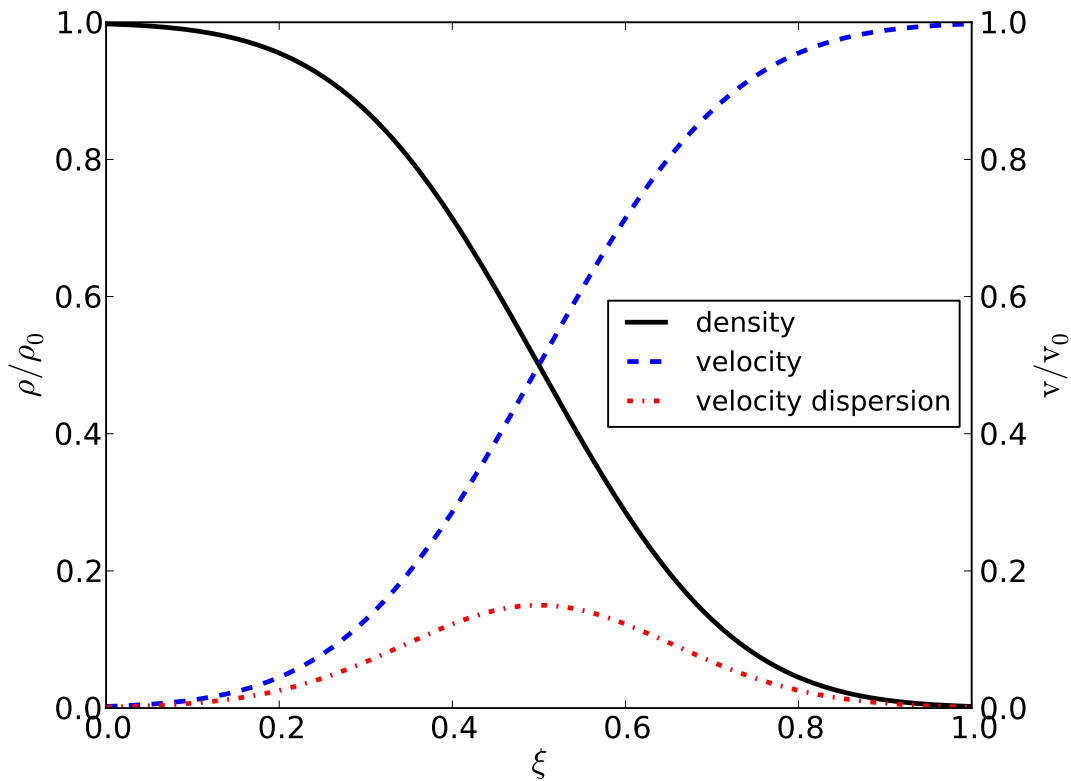
FIGURE 4.5: Density and velocity structure of the entrainment layer. The (black) solid line denotes the density structure (equation 4.43), the (blue) dashed line denotes the velocity structure (Equation 4.44), and the (red) dotted line denotes the structure of the fluctuating velocity (equation 4.46). ξ is defined in Equation 4.45.

4.2.9 Structure of the entrainment layer

To fully specify the structure of the outflow, we need to know the structure of the entrainment layer. The gas motion inside the entrainment layer is dominated by turbulence, and its velocity can be expressed as the sum of a mean component and a fluctuating component [Reynolds, 1895]. There are many experiments and numerical simulations that study the structure of such a mixing layer [e.g. Champagne et al., 1976, Bell & Mehta, 1990, Rogers & Moser, 1994], from which we obtained the structures of the mean velocity and the fluctuating (random) velocity, and parametrized them.

We found that the structure of the entrainment layer is universal and can be represented in a simple parametrized way. We fitted the mean density, the mean velocity and the turbulent velocity structures of Rogers & Moser [1994], and applied the fitting formula to our case.

The fitted density and mean velocity distributions take the forms of

$$\rho(\xi) = \frac{-\mathrm{erf}(4\xi - 2) + 1}{2} \rho_{\mathrm{envelope}} \ , \tag{4.43}$$

and

$$v(\xi) = \frac{\mathrm{erf}(4\xi - 2) + 1}{2} v_{\mathrm{norm}} \ , \tag{4.44}$$

where erf is the error function, and ξ is defined as

$$\xi = \frac{x}{2d} \ . \tag{4.45}$$

d is defined as $d = \Sigma / \rho_{\mathrm{envelope}}$, and $v_{\mathrm{norm}} = 5 \times v_x$ due to the normalization requirement.

The distribution of the fluctuating velocity of the entrainment layer takes the form

$$\begin{aligned}
v_{\mathrm{turb}} &= v_{\mathrm{turb\_norm}}(\mathrm{erf}(4\xi - 2) + 1)(-\mathrm{erf}(4\xi - 2) + 1) \\
&= v_{\mathrm{turb\_norm}}(1 - \mathrm{erf}^2(4\xi - 2)) \ , \tag{4.46}
\end{aligned}$$

where $v_{\mathrm{turb\_norm}} = 0.15 \times v_{\mathrm{norm}}$. Fig. 4.5 shows the structure of density, mean velocity, and fluctuating velocity inside the entrainment layer.

Fig. 4.6 shows the density distribution of our model, from which the entrainment layer can be identified as the region between the outflow cavity and the envelope.

4.3   Observational tests

Observationally, molecular outflows are frequently mapped in the emission from rotational transitions of molecules such as CO and HCO^+. These mapping observations can measure the intensity of the line emission from the outflow in the form of three-dimensional xyv (x-position-y-position-velocity) data cubes. CO is the most abundant and widespread molecule in the interstellar medium apart from the difficult-to-observe H_2, and has been used to trace the bulk of molecular gas. CO observations [Lada, 1985, Arce et al., 2007, and references therein] have revealed a diversity of molecular outflows, some of which show remarkably regular morphologies [e.g. Qiu et al., 2009].

Here we concentrated on modelling the emission from our outflows and studied the connection between the physical structure of the outflow models and the structure of our outflow models observed in a 3D data cube [e.g. Cabrit & Bertout, 1986, 1990, 1992, Stahler, 1994]. To model the emission from the outflow, we need to know its dynamics and its abundance/excitation conditions. The dynamical structure of the outflow has been obtained in §4.2. However, the abundance and excitation are still uncertain: in regions close to the central protostar, the CO molecule can be photodissociated and
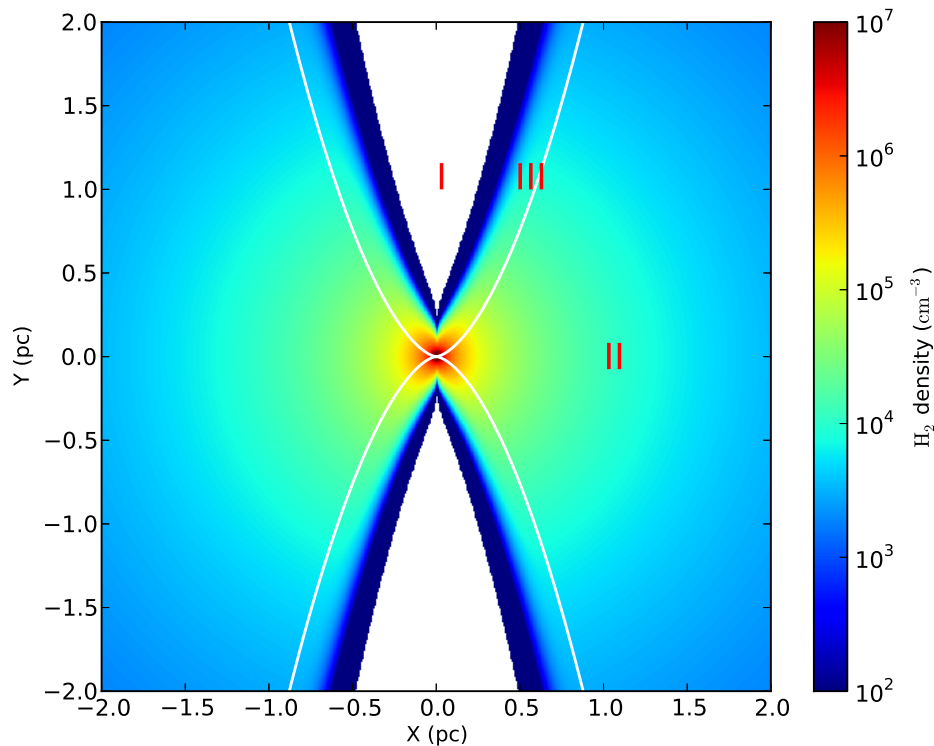
FIGURE 4.6: Density structure of the outflow. Region I represents the inner cavity blown by the wind, region II represents the envelope, and region III represents the outflow layer. The wind mass-loss rate is 1.5×10^{-3} $M_\odot$ yr^{-1}. The thickness of the entrainment layer has been scaled up by a factor of 30 for clarity.

cannot trace the gas anymore. The temperature of the outflow layer is determined by the balance between various heating and cooling processes, which are also uncertain. While these effects will influence the spacial and velocity distribution of the observed CO emission, the morphology of the outflow as well as its overall structure in the position-position and position-velocity spaces are relatively unchanged. Therefore we assume that the CO abundance is 10^{-4} relatively H$_2$ and that the outflow entrainment layer has a constant kinematic temperature of ~ 100K. In the following discussions, we focus on the overall morphology of the outflow in the position-position and position-velocity spaces.

For the velocity dispersion, velocity gradient and kinematic temperature from our model, we used a python version of RADEX [van der Tak et al., 2007] to calculate the population distribution of the CO molecule. We then used a ray-tracing code to calculate the line emission from our outflows. Our ray-tracing calculations were made with the help of LIME [Brinch & Hogerheijde, 2010].

Fig. 4.7 shows a comparison between our model and the observations by Qiu et al.
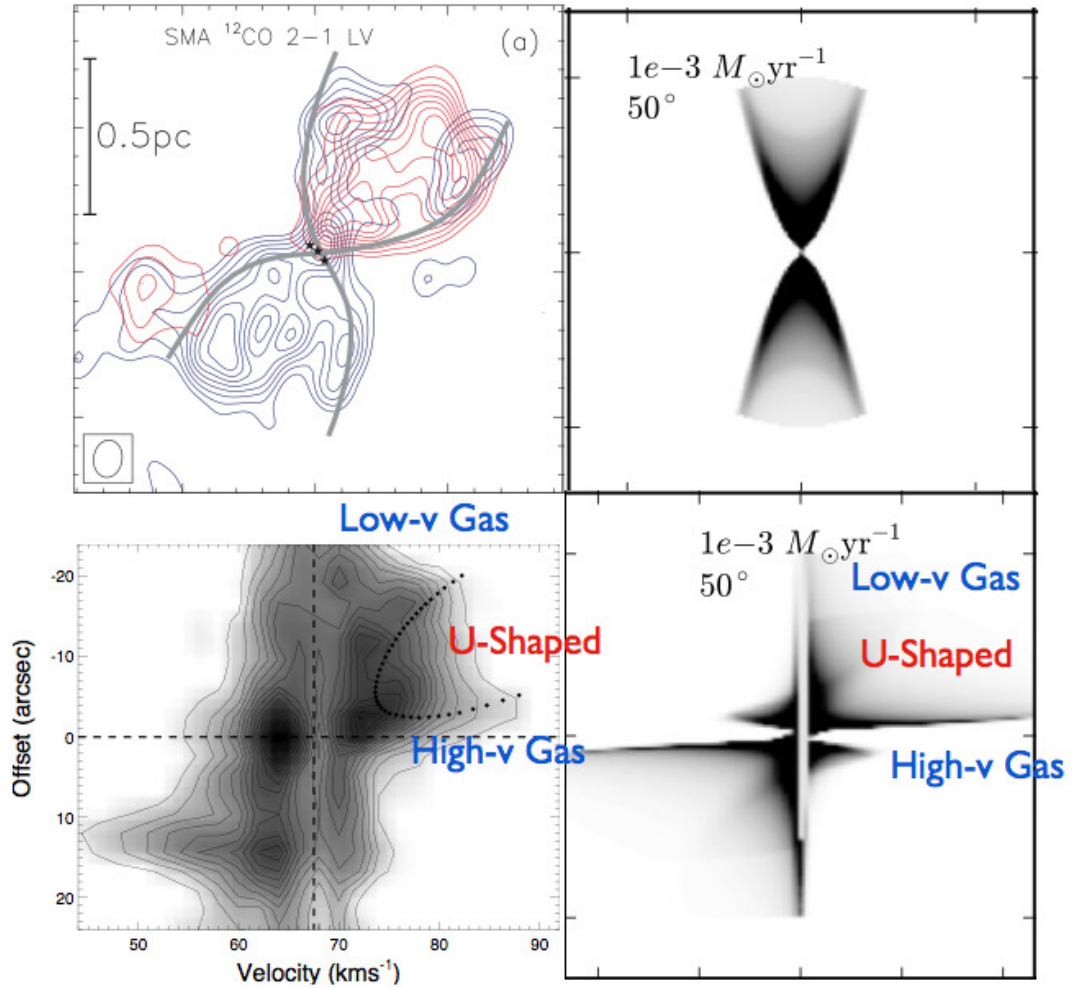
FIGURE 4.7: Comparison between the observations by Qiu et al. [2009] and the predictions from our wind-driven turbulent entrainment model. The **upper left panel** shows the morphology of the outflow observed by Qiu et al. [2009], the **lower left panel** shows the position-velocity structure of the observed outflow. The **upper right panel** shows the morphology of the outflow from our modelling, the **lower middle panel** shows the position-velocity structure of our outflow model cut along its major axis. The outflow model has a mass-loss rate of $1.0 \times 10^{-3} M_\odot \text{ yr}^{-1}$ and an inclination angle of $50°$. For both the observations (lower left panel) and our modelling (lower right panel), the U-shaped region is the region in the position-velocity diagram where the structure of the outflow exhibits a U shape, the Low-v gas region is the region where the gas has a relative small velocity at regions far from the protostar, and the High-v gas region is the region where the gas has a relatively high velocity in the close vicinity to the protostar.
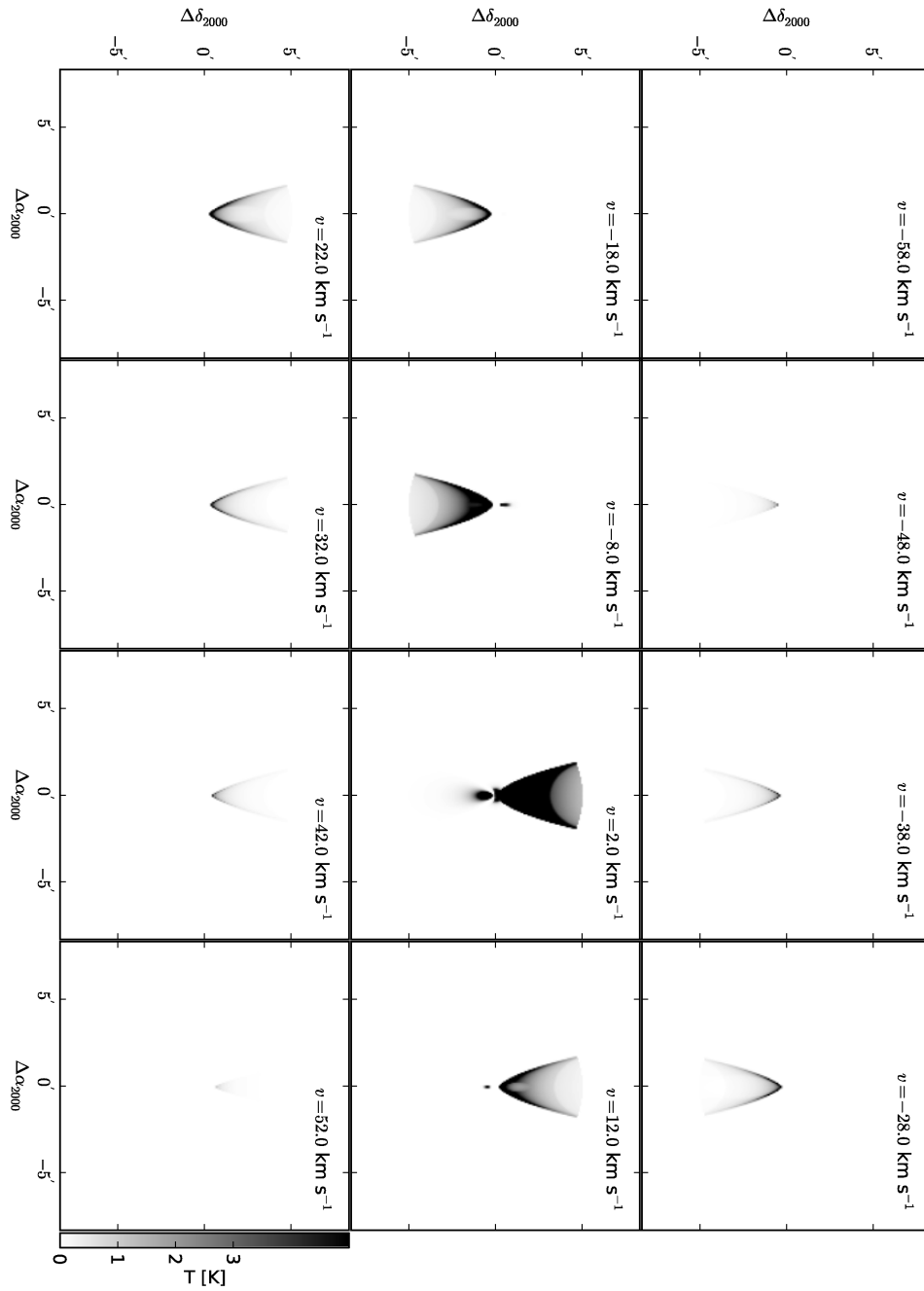
FIGURE 4.8: CO(3-2) channel map of an outflow that has a mass-loss rate of $1.0 \times 10^{-3} M_\odot$ yr^{-1} and an inclination angle of $50°$.
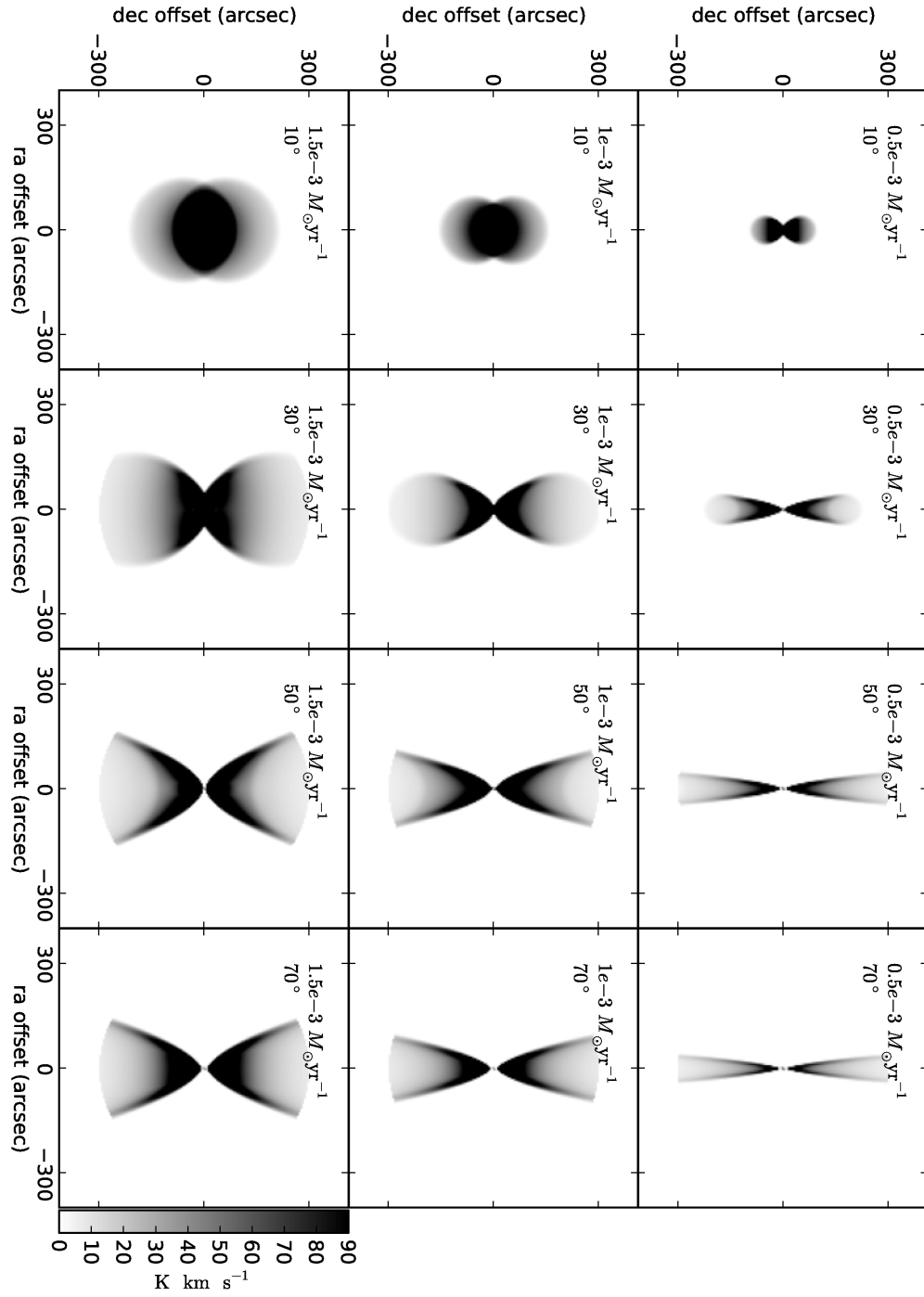
FIGURE 4.9: Velocity-integrated CO(3-2) images of outflows from our model with different wind mass-loss rates and inclination angles.
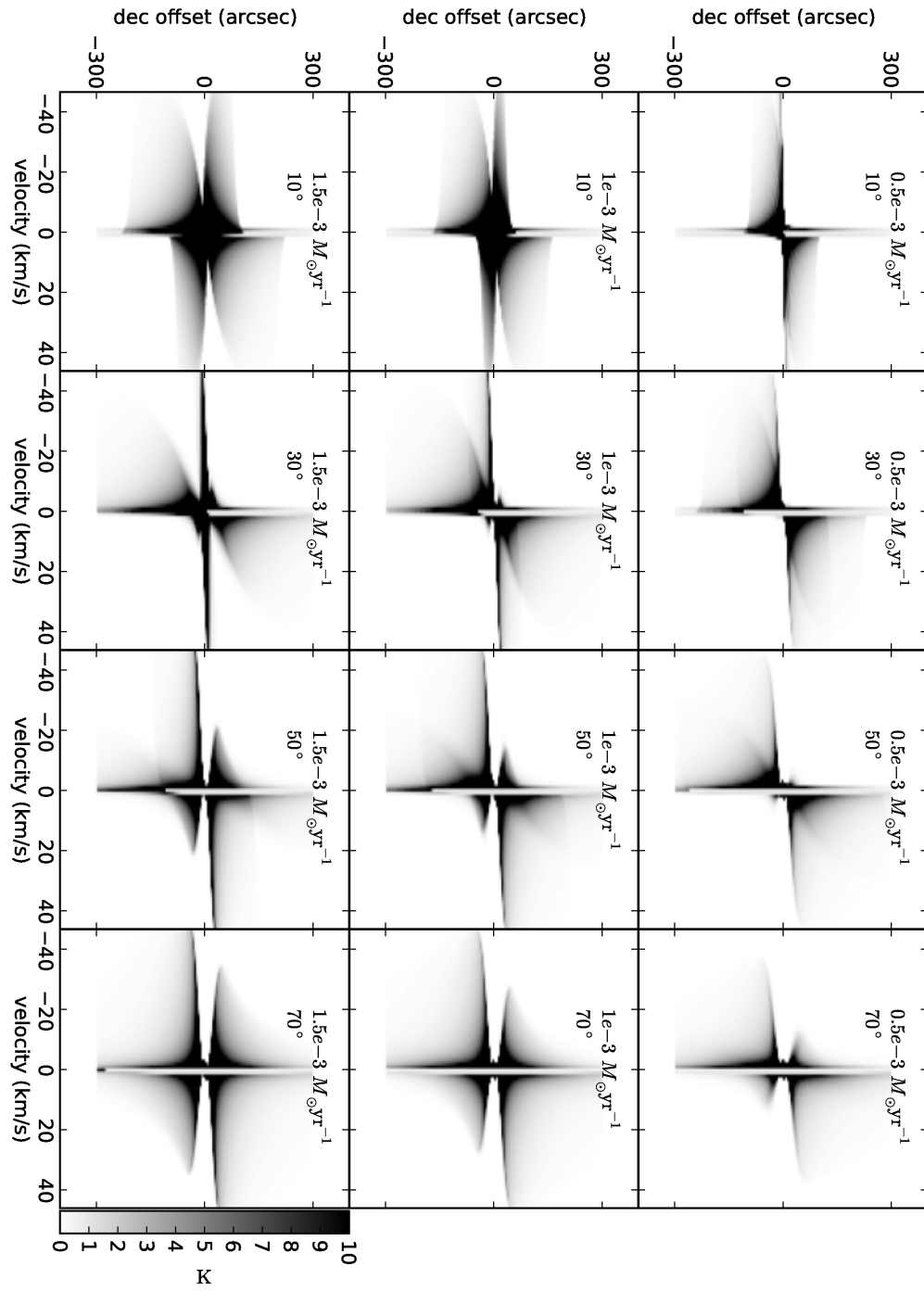
FIGURE 4.10: CO(3-2) position-velocity diagram cut along the major axis of our outflow models with diferent wind mass loss rates and inclination angles.

[2009]. We show the integrated image of the outflow and the position-velocity diagram of the outflow cut along the major axis. The integrated images of the outflow show a regular conical shape in both the observations and our modellings, and the position-velocity diagram of the outflows from observations and modellings show similar shapes. In regions close to the protostar, the observations show a velocity dispersion of about 20 km s^{-1}. This velocity dispersion comes from a continuous distribution of emission and is consistent with observational studies [e.g. Qiu et al., 2011, Cyganowski et al., 2011].

We propose that this feature is one strong evidence for the existence of the entrainment layer. By looking at one position in the image, we integrate through the whole entrainment layer. In one line of sight, this produces a continuous distribution of fluids that move at different speeds (Figure 4.5). Seen from the spectral line profile, we can always identify a broad component, since the line emission traces the distribution of the mass, and the mass distribution inside the entrainment layer is continuous.

On the other hand, the observation shown in Fig. 4.7 is difficult to understand in the context of the wind-driven shell model. In that model, the velocity of the outflow is proportional to the distance from the protostar and should vanish at close vicinity of the protostar, which is not observed (Fig. 4.7). Moreover, the outflow speed are high at regions far away from the protostar because only a high expansion velocity can make the gas move far. But in the observations we can still see low-velocity gas in regions far from the protostar.

Figure 4.8 shows a channel map of an outflow with a mass-loss rate of $1.0 \times 10^{-3} M_\odot$ yr^{-1} and an inclination angle of 50°. The inner part of the outflow is visible in most channels, implying a broad velocity spread at this location. This velocity spread is a direct consequence of the turbulent entrainment process.

Figures 4.9 and 4.10 show the calculated images and position-velocity diagrams of outflows from protostars with different mass-loss rates viewed at different inclination angles. The mass-loss rate takes values of 0.5, 1, 1.5, and $\times 10^{-3}$ M$_\odot$ yr^{-1}, the inclination angles values of 10°, 30°, and 50°. The calculated outflows exhibit a variety of morphologies. They also share some common characteristics: The outflow gas can reach a high velocity in regions close to a protostar; in regions far away from the protostar, there is still gas with low velocities. These features are natural outcomes of the entrainment process (§4.2.9) and can be observed under different circumstances.

4.4 Outflow entrainment as a universal process

Outflows are ubiquitously observed in a variety of situations, which include the formation of low-mass stars and high-mass stars, and the situation in which a wind blown by an AGN interacts and entrains the galactic-scale ambient gas [Alatalo et al., 2011, Tsai et al., 2012]. Here we considered the possibility that these outflows have a common origin, in that all these outflows are formed through the interaction between the wind and the ambient gas in the form of turbulent entrainment.

In §4.4.1, using the turbulent core model of massive star formation [McKee & Tan, 2002, 2003], we show that outflows from low and high-mass protostars can consistently be interpreted as resulting from an universal entrainment process. In §4.4.2, we derive universal scaling relations that can be used to estimate the mass and velocity of the outflows, and suggest that the AGN-driven outflows can be consistently explained in our model. In §4.4.3, using the insights obtained from the scaling analysis, we predict the existence of dwarf outflows in cluster-forming regions, and in §4.4.4 we discuss the self-similarity of our model.

4.4.1 Universal picture of protostellar outflows

As suggested by McKee & Tan [2002, 2003], the formation of high-mass stars can be viewed as a scaled-up version of the standard low-mass star formation theory from gas cores, where most of the pressure support is due to a combination of turbulence and magnetic fields instead of thermal pressure. In this picture, a high level of turbulence prevails in the high-mass star forming regions, causing significant turbulent ram-pressure of the ambient medium. The timescale for the formation of high-mass stars is short, and the accretion rate onto the high-mass protostar is much higher than in the low-mass case.

Our model of a turbulent entrainment outflow is self-similar in nature. By combining it with the self-similar star formation model, we can obtain a universal description of outflows from low and high-mass protostars.

Considering the fiducial case in McKee & Tan [2003], the accretion rate onto the protostar can be estimated as

$$\dot{m}_* \sim 4.6 \times 10^{-4} \times \left(\frac{m_{*f}}{30\ M_\odot}\right)^{3/4} \times \Sigma_{\rm cl} \times \left(\frac{m_*}{m_{*f}}\right)^{0.5} M_\odot\ {\rm yr}^{-1}\,, \qquad (4.47)$$

where m_* is the current mass of the protostar, m_{*f} is the final mass of the protostar when the accretion has been finished, and Σ_{cl} is the surface density of the clump. High-mass star-forming regions are characterized by a high value of Σ_{cl} [McKee & Tan, 2003]. The pressure of the wind from the protostar can be estimated as

$$
\begin{aligned}
\frac{p_{\text{wind}}}{k_{\text{B}}} &= \frac{\dot{m}_{\text{wind}} \times v_{\text{wind}}}{\pi r^2} \\
&= 0.77 \times 10^8 \times \left(\frac{m_{*f}}{30 \ M_\odot}\right)^{3/4} \times \Sigma_{\text{cl}}^{3/4} \times \\
&\quad \left(\frac{r}{\text{pc}}\right)^{-2} \times \left(\frac{m_*}{m_{*f}}\right)^{0.5} \text{K cm}^{-3} ,
\end{aligned}
\tag{4.48}
$$

where k_B is the Boltzmann constant, and we assumed $\dot{m}_{\text{wind}} = 1/3 \times \dot{m}_*$ [Najita & Shu, 1994, where $\dot{m}_*$ is the total accretion rate onto the protostar] and $v_{\text{wind}} = 600$ km s^{-1}. The average pressure of the clump is expressed as [McKee & Tan, 2003]

$$
\frac{\overline{p}_{\text{cl}}}{k_{\text{B}}} = \frac{0.88 \ G}{k_{\text{B}}} \Sigma_{\text{cl}}^2 = 4.2 \times 10^8 \ \Sigma_{\text{cl}}^2 \text{K cm}^{-3} .
\tag{4.49}
$$

For typical parameters, the average pressure of the envelope $\overline{p}_{\text{cl}}$ is similar to the average pressure of the wind at 1 pc, which is approximately the physical size of the outflow. This justifies our suggestion that the ram-pressure of the wind and the ram-pressure of the ambient medium are similar.

The collimation of the outflow is determined by the ratio between the turbulent ram-pressure of the envelope and the ram-pressure of the wind. Stronger winds lead to less-collimated outflows while more turbulent envelopes lead to highly collimated outflows. To summarize these effects, we define the *dimensionless* collimation parameter η of the outflow:

$$
\begin{aligned}
\eta &= \frac{\overline{p}_{\text{cl}}}{p_{\text{wind}}} \\
&= 5.5 \times \left(\frac{r}{\text{pc}}\right)^2 \left(\frac{m_*}{m_{*f}}\right)^{-1/2} \Sigma_{\text{cl}}^{1/2} \left(\frac{m_{*f}}{30 M_\odot}\right)^{-3/4} ,
\end{aligned}
\tag{4.50}
$$

with larger η implying more collimated outflows.

Equation (4.50) has several implications.

The ratio η is proportional to r^{-2}, which means that the pressure of the envelope gradually dominates the pressure of the outflow tends to collimate the outflow with increasing distance from the protostar. This may explain why many outflows exhibit a re-collimated shape, that is, the opening angle of the outflow becomes smaller as we moves away from the protostar [e.g. L1157, Bachiller & Perez Gutierrez, 1997].

Also, $\eta \sim \Sigma_{\text{cl}}^{1/2}$, which means that higher external pressure (stronger turbulence) leads to more collimated outflows. This agrees with the results in §4.2.2, and indicates that turbulence can *collimate* the outflow.

Third, if the pressure of the clump Σ_{cl} is roughly constant, the more massive the star is, the less collimated is the outflow. This is because η depends on the final mass of the protostar, $\eta \sim m_{*f}^{-3/4}$. The more massive the star, the stronger the wind it has. This stronger wind will push the envelope and leads to a less collimated outflow. If several stars form in a clustered way [Qiu et al., 2011], protostars of different mass will share one common environment. We then expect that more massive protostars produce less-collimated outflows.

4.4.2 Outflow mass and velocity

According to our model, the mass of the outflow is determined by the efficiency with which the outflow entrains the envelope gas. Given the opening angle, the mass of the outflow can be estimated as

$$M_{\text{outflow}} \sim \alpha \, \rho_{\text{average}} \, \sigma_{\text{average}} \times t \times L^2 \ . \tag{4.51}$$

where L is the physical scale of the outflow and ρ_{average} and σ_{average} are the average density and velocity dispersion, respectively. The average pressure of the envelope is

$$p_{\text{envelope}} \sim \rho_{\text{average}} \times \sigma_{\text{average}}^2 \ . \tag{4.52}$$

The momentum of the outflow is determined by the amount of momentum injected by the wind and can be estimated as

$$P_{\text{outflow}} \sim \dot{M}_{\text{wind}} \times t \times v_{\text{wind}} \times \beta \ , \tag{4.53}$$

and the ram-pressure of such a wind can be estimated as

$$p_{\text{wind}} \sim \frac{\dot{M}_{\text{wind}} \times v_{\text{wind}}}{L^2} \ . \tag{4.54}$$

If the cavity blown by the outflow is stable, the ram-pressure of the wind p_{wind} is expected to be similar to the turbulent ram-pressure of the envelope, p_{envelope}, and we have (from Equation 4.52 and Equation 4.54)

$$\dot{M}_{\text{wind}} \times v \sim \rho_{\text{wind}} \sigma_{\text{wind}} L^2 \ . \tag{4.55}$$

The outflow velocity is then (equations 4.51, 4.52, and 4.55)

$$
\begin{aligned}
v_{\text{outflow}} \quad &\sim \quad \frac{P_{\text{outflow}}}{M_{\text{outflow}}} \sim \frac{\dot{M}_{\text{wind}} v_{\text{wind}}}{\rho_0 \sigma_0} \times \frac{\beta}{\alpha} \\
&\sim \quad \sigma_{\text{average}} \frac{\beta}{\alpha} \sim 3 \times \sigma_{\text{average}} \ .
\end{aligned}
\tag{4.56}
$$

In the last step we inserted the numerical values of α and β. The velocity of the outflow is several times higher than the velocity dispersion of the envelope.

This fact can be understood as follows: If the wind and the envelope can establish hydrostatic equilibrium, then increasing turbulent velocity σ, the pressure of the wind has to scale according to σ^2 to balance wind pressure. Therefore, the momentum injection of the wind scales as σ^2. On the other hand, the mass supply of the outflow from the envelope in the form of the entrainment process only scales as σ^1. The outflow velocity, which is estimated as P/M, scales as σ^1.

These results outline one important property of the turbulent entrainment outflow, namely that the velocity of the outflow is higher than while still similar to the velocity dispersion of the ambient gas. This is independent of other parameters such as the strength of the wind, and is based only on the assumption that the wind and the envelope can establish hydrostatic equilibrium.

In recent *Herschel*-HIFI observations of high-J CO emission in low and high-mass star-forming regions [San Jose-Garcia et al., 2013], it was found that the velocity of the outflows (traced by the FWHM of the broad ^{12}CO(10-9) line emission) is higher than while still similar to the velocity of the envelope (traced by the FWHM of the C^{18}O(9-8) line). Also interesting is the fact that broader envelope line width is usually associated with broader outflow line width. This implies that the outflows from different regions share some physical similarities, and one possibility is that all these outflows come from the same entrainment process.

In a recently discovered AGN-driven outflow [Alatalo et al., 2011], the line width of the ambient gas (single-peaked central velocity component) is $\sigma_{\text{envelope}} \sim 100$ km s^{-1}, while the width of the broad line wing caused by the outflow activity is $v_{\text{outflow}} \sim 300$ km s^{-1}. Although velocity of the ambient gas and the velocity of the outflow are much higher than those of protostellar outflows, their ratio $v_{\text{outflow}}/\sigma_{\text{envelope}}$ is about 3. This is similar to the ratio predicted in our model (equation 4.56), which suggests that these outflows may be the outcome of the turbulent entrainment process working between the wind emitted by the central AGN and the galactic-scale ambient gas.

4.4.3 Dwarf outflows

As we have shown in §4.4.1, the emergence of an outflow depends on the pressure of the envelope and the pressure of the wind reaching a balance. This is not always true. If the wind from the protostars is not strong enough to blow away the envelope, we expect to see that the outflows have small spatial extent and are confined to small regions.

Such "Dwarf" outflows may exist under several conditions. If several protostars form in a clustered way [e.g. Qiu et al., 2011], then the outflows from the low-mass protostars of different mass may be confined by the turbulence and appear as "dwarf outflow". Alternatively, such "Dwarf" outflows may exist at regions where the wind from the protostar is extremely weak [e.g. VeLLOs Lee et al., 2009, Dunham et al., 2010]. Studies of such "Dwarf" outflows will help to gain insights into the interaction between the wind and the envelope in extreme cases.

4.4.4 Self-similarity of the model

We explored the self-similar properties of our model. Each model is characterized by several parameters: a wind mass-loss rate $\dot{M}_0$, a turbulence velocity σ_0, a wind velocity v_0^{wind}, a density ρ_0, an outflow age t_0, and the entrainment parameters α_0 and β_0. Our model is self-similar if when gravity is neglected. Here we derive the condition at which the structure of another outflow characterized by a different set of parameters ($\dot{M}_1$, σ_1, v_1^{wind}, ρ_1, t_1, α_1, and β_1) can be obtained from scaling of a different outflow.

The opening angle of the outflow is determined by the relative strength of the ram-pressure of the wind and the turbulent ram-pressure of the envelope. For it to be unchanged, we require

$$\frac{\rho_1 \sigma_1^2}{\rho_0 \sigma_0^2} = \frac{\dot{M}_1 \times v_1^{\text{wind}}}{\dot{M}_0 \times v_0^{\text{wind}}} \ . \tag{4.57}$$

If equation 4.57 is satisfied, the two outflows will have the same shape. But the total amount of gas contained in the outflows and their velocity are different. The amount of gas is proportional to the entrainment rate and proportional to the outflow age, therefore

$$\frac{M_1}{M_0} = \frac{\rho_1 \sigma_1 t_1 \alpha_1}{\rho_0 \sigma_0 t_0 \alpha_0} \ . \tag{4.58}$$

As discussed in §4.4.2, the velocity of the outflow is proportional to the velocity dispersion of the envelope,

$$\frac{v_1}{v_0} = \frac{\sigma_1}{\sigma_0} \ . \tag{4.59}$$

These scaling relations help us to put outflows with different masses and velocities into a common picture.

4.5   Conclusions

We studied the interaction between the wind from a protostar and the ambient gas in the form of turbulent mixing and proposed a wind-driven turbulent entrainment model for protostellar outflows. In the model, the wind from a protostar is in hydrostatic balance with the gas in the turbulent envelope, and the outflowing gas is completely contained in the turbulent entrainment layer that develops between the wind and the envelope. Turbulence in the ambient gas plays two roles in our model: first, turbulent motion determines the shape of the outflow (§4.2.2). Second, turbulence contributes to the mass growth of the mixing layer (§4.2.4). Our model is a universal one in that it can explain the outflows from both low and high-mass protostars (§4.4).

Our model can reproduce the geometry and kinematic structure of the observed outflows (§4.3, Figure 4.7, 4.9 and 4.10). The main results from this study can be summarized as follows:

1. At the physical scale of an outflow, the average ram-pressure of wind is similar to the average ram-pressure of its envelope (§4.2.2, 4.4.1).

2. The opening angle of the outflow is dependent on the pressure balance between the wind and the envelope, therefore it can evolve if the pressure of the wind or the pressure of the envelope changes (§4.2.2, 4.4.1).

3. The ram-pressure of the wind tends to decollimate the outflow, the ram-pressure of the environment tends to *collimate* the outflow (§4.2.2, 4.4.1).

4. At one given point in the observed image of the outflow, the emission has a wide spread in velocity (§4.3, Figure 4.10). Both high-velocity gas in the close vicinity of the protostar and low-velocity gas in regions far from the protostar exist as the results of the turbulent entrainment process.

5. If the outflow is formed through the turbulent entrainment process outlined here, the velocity spread of the outflow is expected to be about times the velocity spread of the ambient gas (§4.4.2). This is independent of the other physical parameters, such as the strength of the wind and the density of the region.

6. In clustered star-forming regions, we expect a population of dwarf outflows that are confined by the pressure of their environment into small regions (§4.4.3).

The universality of the entrainment process motivates speculation that the same entrainment process may be at work in AGN-driven outflows [Alatalo et al., 2011, Tsai et al., 2012]. We suggest that the turbulent entrainment process works ubiquitously in nature and plays an important role in shaping outflows in many different situations.

4.6 Appendix

4.6.1 Effect of centrifugal forces

As the outflowing gas moves along the cavity, it exerts a centrifugal force on its surrounding. This effect has been considered in several previous works [Canto, 1980, Canto & Rodriguez, 1980, Biro et al., 1993, e.g.]. The pressure produced by the centrifugal force can be estimated as

$$p_{\text{centrifugal}} \sim v_{\text{outflow}}^2 \kappa \rho_{\text{outflow}} d \ , \tag{4.60}$$

where v_{outflow} is the velocity of the outflow, κ is the curvature of the outflow cavity, ρ_{outflow} is the density of the outflow, and d is the thickness of the outflow.

The ram-pressure of the envelope is

$$p_{\text{envelope}} \sim \rho_{\text{envelope}} \times \sigma_{\text{turb}}^2 \ . \tag{4.61}$$

In our entrainment model, the density of the outflow is similar to the density of the envelope $\rho_{\text{outflow}} \sim \rho_{\text{envelope}}$, and the velocity of the outflow is several times the velocity dispersion of the envelope (Equation 4.56). Therefore, the ratio between centrifugal pressure and the pressure of the envelope is

$$f = \frac{p_{\text{centrifugal}}}{p_{\text{envelope}}} \sim \frac{\rho_{\text{outflow}} \kappa d v_{\text{outflow}}^2}{\rho_{\text{envelope}} \sigma_{\text{turb}}^2} \sim 10 \times d \times \kappa \sim 10 \times \frac{d}{R} \ , \tag{4.62}$$

where R is the curvature radius. Here we are interested in making order-of-magnitude estimations, and the effect of projection on the pressure is neglected. Therefore we have $p_{\text{wind}} \sim p_{\text{envelope}}$. In our calculation, R is approximately the size of the outflow and d is the thickness of the outflow. Here, we take advantage of the fact that $\rho_{\text{outflow}} \sim \rho_{\text{envelope}}$ and $v_{\text{outflow}} \sim 3v_{\text{envelope}}$. It can be seen that if $d \sim R$, centrifugal force will play an important role in changing the shape of the outflow cavity. In our case, since $d \ll R$ (Fig. 4.6, note that the thickness of the outflow has been artificially scaled up for clarity, and

in fact our outflow layer is very thin compared with the size of the outflow), the influence of centrifugal force is within a few percent and is therefore generally insignificant.

Our case is different from the case of Canto & Rodriguez [1980] and Biro et al. [1993] who found the centrifugal force to be important. This is because our entrainment process conserves momentum and at the same time increases the mass of the outflow significantly, and in Canto & Rodriguez [1980] and Biro et al. [1993] the entrainment process is insignificant. To illustrate the effect of mass growth on the centrifugal force, we consider a particle of mass m rotating along a circle of radius R with velocity v. The centrifugal force can be expressed as

$$f = \frac{mv^2}{R} = \frac{p^2}{mR} \ , \tag{4.63}$$

where p is magnitude of the momentum of the particle. Here, it is quite clear that when the momentum is conserved, the larger the mass, the weaker the centrifugal force.

In our case, the entrainment process conserves momentum, but the mass of the outflow has been increased by a huge factor. Assuming pressure balance $p_{\rm wind} \sim p_{\rm envelope}$, we have $\rho_{\rm wind} v_{\rm wind}^2 \sim \rho_{\rm envelope} \sigma_{\rm envelope}^2$. The mass from the wind is $m_{\rm wind} \sim \rho_{\rm wind} v_{\rm wind} \beta \times {\rm d}s$, where ${\rm d}s$ represents the surface area, and the mass from the envelope is $m_{\rm envelope} \sim \alpha \times \rho_{\rm envelope} \sigma_{\rm envelope} \times {\rm d}s$. The ratio $m_{\rm envelope}/m_{\rm wind}$ is

$$\frac{m_{\rm envelope}}{m_{\rm wind}} \sim \frac{\rho_{\rm envelope} \times v_{\rm envelope}}{\rho_{\rm wind} \times v_{\rm wind}} \tag{4.64}$$
$$\sim \frac{p_{\rm envelope}/\sigma_{\rm envelope} \times \alpha}{p_{\rm wind}/v_{\rm wind} \times \beta} \sim \frac{1}{3} \times \frac{v_{\rm wind}}{\sigma_{\rm envelope}} \ .$$

Since $v_{\rm wind} >> \sigma_{\rm envelope}$, the mass growth from the entrainment process is huge, therefore the centrifugal force becomes insignificant.

As the wind gas mixes with the ambient gas, the momentum of the system is conserved, but the mass of the system becomes much larger, therefore the centrifugal force becomes much smaller. This is because the momentum-conserving entrainment process increases the outflow mass significantly so that the centrifugal force is insignificant.

4.7   Acknowledgements

Chapter 5

Discussions & summary

In this chapter I discuss briefly the major findings of my PhD study.

5.1 Structure of the Milky Way and the evolution of molecular clouds

5.1.1 Scene

In two of the chapters, I discuss the dynamics of molecular clouds, chose to focus on different questions.

In recent years, studies of molecular clouds has been progressing in two directions. The first follows the time axis, and the second one goes toward the physics of molecular cloud. Along the time axis, it is recognized that molecular clouds are evolving objects. So instead of asking questions such as "On what timescale do molecular clouds collapse?" people begin to think of the clouds as objects that are constantly interacting with each other [Dobbs & Pringle, 2013]. Today it is believed that molecular clouds are born either from agglomeration of smaller cloudlets [Dobbs et al., 2011], or from dynamically-triggered thermal instability [Hennebelle & Pérault, 1999] that occurs in the spiral arms. If the molecular clouds are constantly interacting with each other as found by Dobbs et al. [2011], it is difficult to speak of the lifetimes of molecular clouds. The lifetime of the molecular gas may still be valid. It is also realized that massive stars which form inside molecular clouds are capable of destroying their parental cloud [Walch et al., 2012]. In this sense, the clouds can have finite lifetimes.

The other direction goes towards examining the physics of the molecular clouds. What controls the evolution of a molecular cloud? Some time ago, the paradigm was that

molecular clouds are supported against gravity by magnetic fields, nowadays it is thought that molecular clouds are dominated by turbulence and collapse as a result of gravity [Larson, 1981, Krumholz & McKee, 2005]. However, it is not clear how the turbulence is injected. It is also not known if gravitational collapse contributes to driving and maintaining the turbulence in the cloud [Klessen & Hennebelle, 2010, Robertson & Goldreich, 2012]. Moreover, the physics of turbulence is in itself very complicated, and what will happen if we combine turbulence with gravity is a question that is still not resolved [1].

5.1.2 Dynamics and lifetime of molecular gas

The research of my PhD can be easily projected along the two directions. The chapter on the ≥ 500 pc filamentary gas wisp focuses on the large-scale structure of the molecular gas, and is among the first few works that study the coherent structure of the molecular gas in the Milky Way beyond the cloud scale.

The project must be understood in the context of the recent developments in the understanding of molecular cloud. These developments are driven from two sides: On the theoretical side, it has now became feasible to simulate the whole galactic disk and at the same time resolve the individual molecular clouds, despite the quite different approaches adopted by different authors, filamentary condensations of molecular gas are commonly seen in the simulations [Tan, 2000, Kim & Ostriker, 2002, Dobbs & Bonnell, 2006, Dobbs et al., 2006, Shetty & Ostriker, 2006, Tasker & Tan, 2009, Ceverino et al., 2012]. On the observational side, filamentary gas condensations are found in a recent survey of spiral galaxy M51 [Schinnerer et al., 2013]. However no such structures have been studied in the Milky Way.

With this background we study the coherence of molecular gas in the Milky Way. One advantage of studying such structures is that we are in the Milky Way, and as a result we have much better spatial resolution and sensitivity compared to the case of nearby galaxies.

What we finally found is a filamentary gas structure that is ≥ 500 pc long. The structure has a length that is much larger than the thickness of the molecular disk, and is highly elongated. The fact that the gas wisp is much larger than the thickness of the Milky Way disk implies that the gas wisp can not be created *locally* in the disk. The global evolution of the galactic disk must have played a role. This is in good agreement with what has been found in recent simulations of the galactic disk.

---

[1]However the interest in combining an ideal turbulence with gravity is increasing [Hennebelle & Chabrier, 2008, Hopkins, 2013].
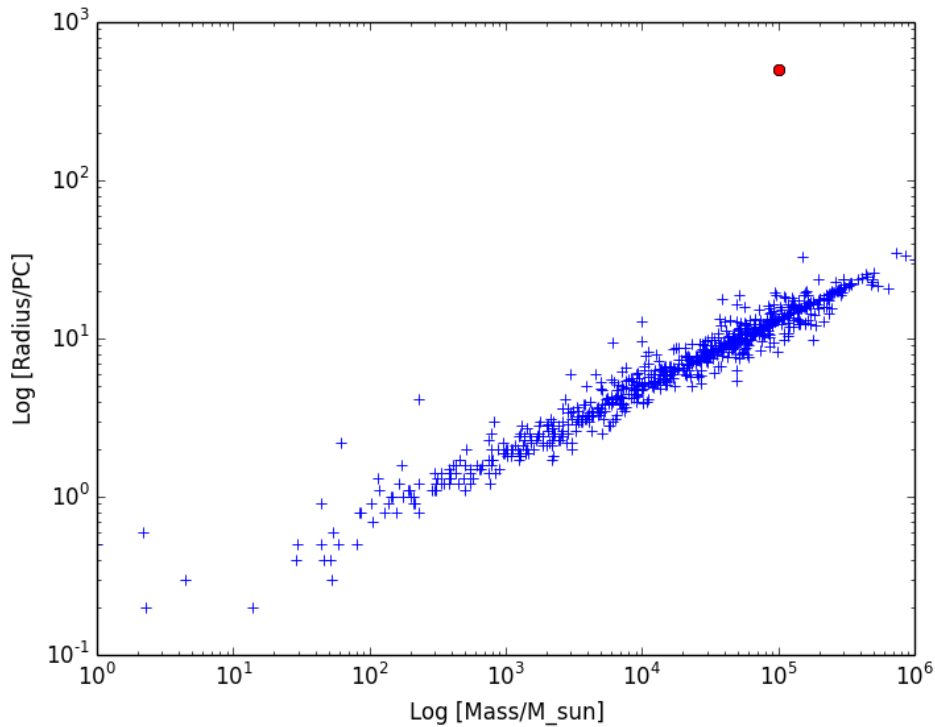
FIGURE 5.1: Mass-radius relation of the filamentary gas wisp and the clouds in the Galactic Ring Survey. The blue "+'s' stand for the molecular clouds observed in the Galactic Ring Survey [Jackson et al., 2006], and the red dot stands for the filamentary gas wisp [Li et al., 2013b].

The filamentary gas wisp is still shorter than the typical separation between different spiral arms in the Milky Way projected along the direction of the Galactic rotation. Therefore it is not fully clear if it will survive from one of the spiral arms in the Milky Way to another. If it survives, it means that molecular gas can be cold when it enters the spiral arm, and this will give a stronger support to the cloud formation scenario of Pringle et al. [2001].

Since our filamentary gas wisp is a new kind of object, it is interesting to compare it to the "ordinary" molecular clouds observed in the Galactic Ring Survey [Roman-Duval et al., 2010]. The mass, radius and velocity dispersion of our filamentary gas wisp is measured in Chapter 2.

Fig. 5.1 is a comparison between molecular clouds covered in the GRS survey and the filamentary gas wisp in the mass-radius plane. The GRS clouds satisfy $m \sim r^{2.36}$ [Roman-Duval et al., 2010] and compared to the clouds, our filamentary gas is much longer. Fig. 5.2 is a comparison in the mass-velocity plane. If counted as a single object, the mass of the filamentary gas is comparable with that of an ordinary molecular cloud,
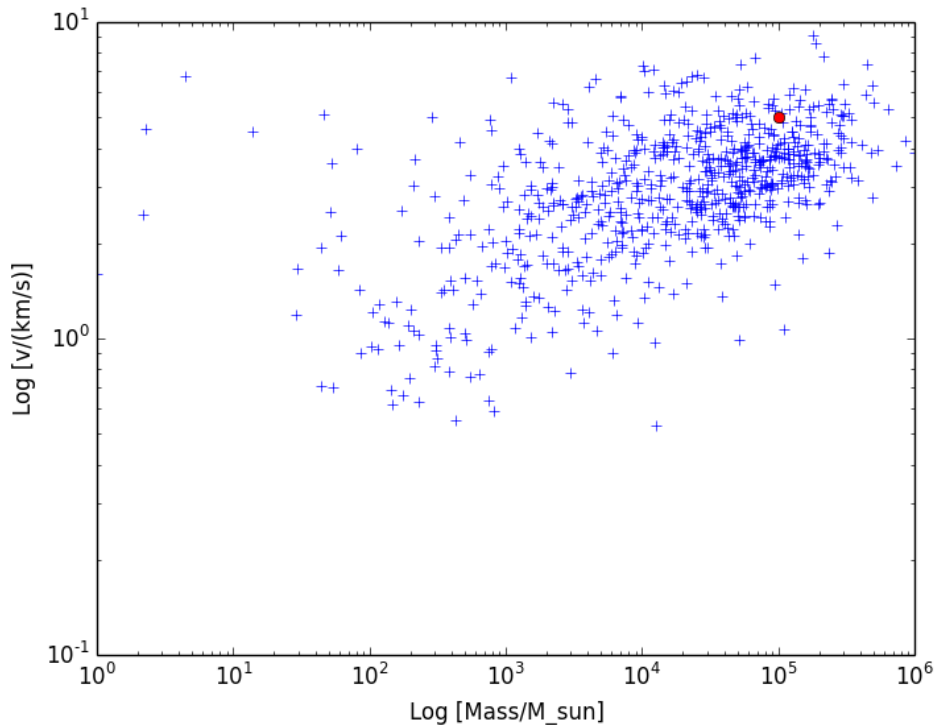
FIGURE 5.2: Mass-velocity relation of the filamentary gas wisp and the clouds in the Galactic Ring Survey. The blue "+'s' stand for the molecular clouds observed in the Galactic Ring Survey [Jackson et al., 2006], and the red dot stands for the filamentary gas wisp [Li et al., 2013b].

and so does the velocity dispersion. Fig . 5.3 is the same comparison in the length-velocity dispersion plane. Here the filamentary gas wisp is much larger than an ordinary molecular cloud, however its velocity dispersion is comparable to the velocity dispersion of a ordinary cloud.

In short, our filamentary gas wisp is a highly elongated object, and its velocity dispersion (~ 5 km s^{-1}) is surprisingly small given its length. This have interesting implications for the dynamics of molecular clouds.

The velocity dispersion of the molecular gas is a measure of the amount of kinematic energy, which is related to the degree of turbulent motion at a given physical scale. It is proposed that the kinematic energy of the molecular cloud is injected from outside the cloud [Klessen, 2011]. This means the injection scale must be larger than the cloud scale ($\sim 10^2$ pc). In our case, we probe the physical scale from 1 parsec to 500 parsec with our filamentary gas wisp [Li et al., 2013b], and find that the velocity dispersion reaches its maximum at ~ 100 pc and does not go up even if we reach the maximum physical scale of 500 pc. *Therefore, the plausible scale at which turbulence in injected into a molecular cloud is the physical size of a molecular cloud. In other words, turbulence is injected*
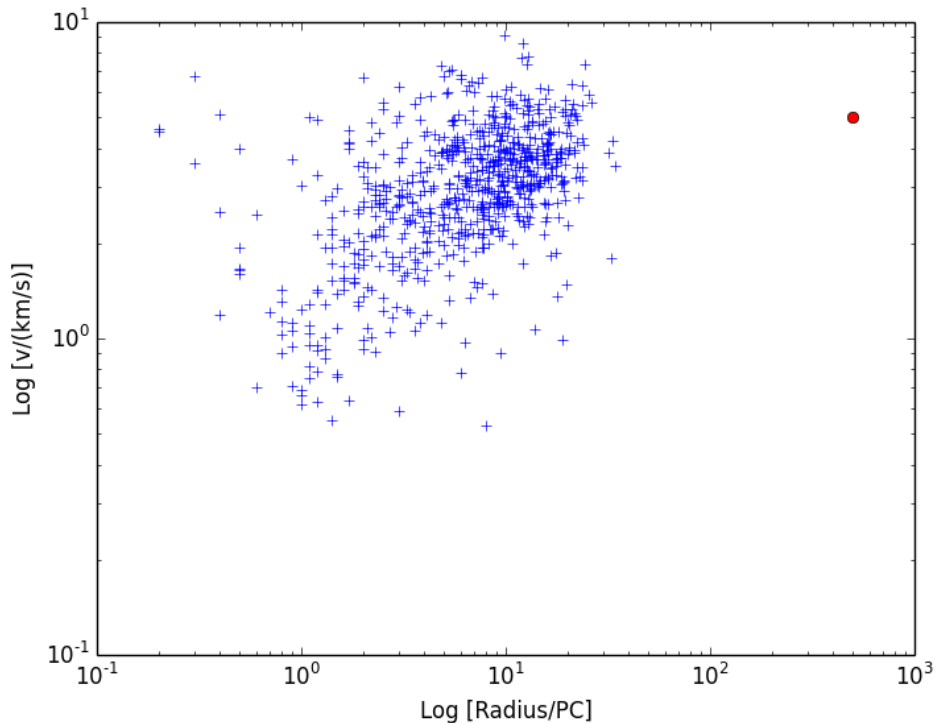
FIGURE 5.3: Size-velocity relation of the filamentary gas wisp and the clouds in the Galactic Ring Survey. The blue "+'s' stand for the molecular clouds observed in the Galactic Ring Survey [Jackson et al., 2006], and the red dot stands for the filamentary gas wisp [Li et al., 2013b].

right at the boundary of the clouds. This may imply that turbulence in injected during the very process of cloud formation.

We therefore have an example where our knowledge is restricted by our method. Historically molecular gas has been studied in terms of "molecular cloud". Molecular cloud is just a proper name used to refer to objects detected in a survey through certain algorithms (e.g. the use of clumpfind, [Williams et al., 1994] in the Galactic Ring Survey [Jackson et al., 2006]). Since most of the research is based this concept, the structures beyond the cloud scale is neglected automatically. One part of my contribution is to overcome this barrier and to *recover what we had lost after we accepted the concept "molecular cloud"*.

What did we obtain from this effort? The energy source of turbulence in molecular cloud is a long-standing question in the field. Until now a definitive answer has not been found, and this is mainly because the answer is not in the cloud. It is just *outside* the cloud. For a better understanding to turbulence it is mandatory to recover the large structures beyond the scales of individual clouds.

5.1.3 Internal dynamics of the molecular clouds

In another direction, my research focuses on the *physics* of molecular clouds. When I started studying star formation, it was believed theoretically that molecular clouds are dominated by turbulence, and gravity is important at the smaller scales where collapse is expected to occur. I also realized that gravity is a long-range force, and strangely nearly all the studies of the importance of gravity in molecular clouds are localized [e.g. Bertoldi & McKee, 1992].

The "traditional" way of analyzing the importance of gravity is very simple: first, we select a region based on a certain algorithm (e.g. clumpfind, [Williams et al., 1994]), and second, we analyze the importance of gravity using the virial parameter [Bertoldi & McKee, 1992]. It is in this way that gravity has been found to be important in several cases [Kauffmann et al., 2013].

There are several drawbacks with this approach. The first one is the arbitrariness of the region. Indeed, varying the clump search input parameters may result in quite different outcomes [Pineda et al., 2009]. Therefore it is not clear if the structures found by an algorithm correspond to "real" structures. Interestingly, using an improved algorithm, Goodman et al. [2009] found that gravity is dominant at a variety of physical scales in the molecular cloud L1448.

Another related issue is the large dispersion of virial parameters found for different objects. In [Kauffmann et al., 2013], the resulting virial parameters range from 1 to 10, and it is still difficult to say if molecular gas is gravitationally bound in general.

After a few trials I realized that the problem is in the question itself. So instead of asking "Is gravity important at regions that are selected?" I turn the question around and ask "Over what region does gravity become important?". Therefore I started to think of a method which estimates the importance of gravity *before* the regions are identified. In order to achieve this, the importance of gravity had to be assessed with a completely different approach.

I finally developed a method which can mark out the regions where gravity dominates in 3D position-position-velocity data cubes. With this method it is straightforward to demonstrate that gravity is *dominant* at some of the active regions of the molecular clouds where star clusters form, and is important for the majority of the molecular gas in the cloud. What is more interesting is that the method opens up a set of possibilities of linking gravity with different observations. It allows us to ask questions such as "Are all the regions where star cluster formation take place gravitationally bound?", and several follow-up studies are already going on.

5.2 Molecular outflow and star cluster formation

In another project I studied the formation of molecular outflows.

Outflow is a phenomenon that occurs commonly during the formation of stars. It is believed to be one of the major means of sustaining turbulence in the clouds. *If the energy of outflows can maintain turbulence, why can't turbulence back-reacts on outflows?* Following this question I calculated the pressure from the wind and the pressure from the *turbulent* envelope, and found that the two are comparable. Therefore the pressure from the envelope is not negligible. If we want a physically-consistent model of outflows from protostars, we must take the interaction between the wind and the *turbulent* envelope into account.

Therefore I decided to tackle this problem by constructing an analytical model of wind-ambient gas interaction. What I finally found is that the observed mass, momentum and kinematic structure of molecular outflows can be produced by taking the interaction between the wind and the *turbulent* envelope into account.

The model is analytical, and it can be easily scaled to explain outflows with different parameters. More interestingly, since the outflow shape is determined by the pressure balance between the wind and the envelope, the opening angle can be used as an indicator of the pressure of the envelope.

5.3 Final words

Here I would like to recapitulate what is discussed in the introduction. In the beginning I mentioned a table which summarizes all the relevant knowledge for my star formation studies (Table. 1.1). It seems that the knowledge in star formation has a well-defined structure.

What did I accomplish in my PhD? Where did I contribute in the context of Table. 1.1? Instead of working inside the individual cells, I tried to connect different cells. On the large scale, I tried to connect the dynamics of the Milky Way with the dynamics of molecular clouds. On the cloud scale, I tried to combine the theoretical studies of the gravitational dynamics of molecular clouds with observational data. In the project on the molecular outflow, I connected the turbulence in star-forming regions with the formation of the outflow. For all these projects, I tried to connect either the studies at different physical scales (vertical axis) or the studies at different physical processes (horizontal axis). If what I listed in Table 1.1 is something real, then the purpose of my studies is to show that the table is *evolving*: the boundaries are certainly not rigid,

and perhaps this whole constellation of knowledge will dissolve. This thesis should be considered as the dissolution itself.

Bibliography

Alatalo, K., Blitz, L., Young, L. M., et al. 2011, ApJ, 735, 88

Anderson, L. D., & Bania, T. M. 2009, ApJ, 690, 706

André, P., Belloche, A., Motte, F., & Peretto, N. 2007, A&A, 472, 519

André, P., Di Francesco, J., Ward-Thompson, D., et al. 2013, ArXiv e-prints, arXiv:1312.6232

André, P., Men'shchikov, A., Bontemps, S., et al. 2010, A&A, 518, L102

Arce, H. G., & Sargent, A. I. 2006, ApJ, 646, 1070

Arce, H. G., Shepherd, D., Gueth, F., et al. 2007, Protostars and Planets V, 245

Arzoumanian, D., André, P., Didelon, P., et al. 2011, A&A, 529, L6

Audit, E., & Hennebelle, P. 2005, A&A, 433, 1

Bachiller, R., & Perez Gutierrez, M. 1997, ApJ, 487, L93

Ballesteros-Paredes, J., Hartmann, L., & Vázquez-Semadeni, E. 1999, ApJ, 527, 285

Ballesteros-Paredes, J., Klessen, R. S., Mac Low, M.-M., & Vazquez-Semadeni, E. 2007, Protostars and Planets V, 63

Bally, J., Lanber, W. D., Stark, A. A., & Wilson, R. W. 1987, ApJ, 312, L45

Bania, T. M., Anderson, L. D., & Balser, D. S. 2012, ApJ, 759, 96

Beaumont, C. N., Offner, S. S. R., Shetty, R., Glover, S. C. O., & Goodman, A. A. 2013, ApJ, 777, 173

Beaumont, C. N., Williams, J. P., & Goodman, A. A. 2011, ApJ, 741, 14

Bell, J. H., & Mehta, R. D. 1990, AIAA Journal, 28, 2034

Benjamin, R. A., Churchwell, E., Babler, B. L., et al. 2003, PASP, 115, 953

Bertoldi, F., & McKee, C. F. 1992, ApJ, 395, 140

Beuther, H., Schilke, P., & Gueth, F. 2004, ApJ, 608, 330

Beuther, H., Schilke, P., Menten, K. M., et al. 2002, ApJ, 566, 945

Beuther, H., & Shepherd, D. 2005, in Cores to Clusters: Star Formation with Next Generation Telescopes, ed. M. S. N. Kumar, M. Tafalla, & P. Caselli, 105–119

Bieging, J. H., Peters, W. L., & Kang, M. 2010, ApJS, 191, 232

Biro, S., Canto, J., Raga, A. C., & Binette, L. 1993, Rev. Mexicana Astron. Astrofis., 25, 95

Bocchino, F., Bandiera, R., & Gelfand, J. 2010, A&A, 520, A71

Brinch, C., & Hogerheijde, M. R. 2010, A&A, 523, A25

Cabrit, S., & Bertout, C. 1986, ApJ, 307, 313

—. 1990, ApJ, 348, 530

—. 1992, A&A, 261, 274

Canto, J. 1980, A&A, 86, 327

Canto, J., & Raga, A. C. 1991, ApJ, 372, 646

Canto, J., & Rodriguez, L. F. 1980, ApJ, 239, 982

Carey, S. J., Noriega-Crespo, A., Mizuno, D. R., et al. 2009, PASP, 121, 76

Ceverino, D., Dekel, A., Mandelker, N., et al. 2012, MNRAS, 420, 3490

Champagne, F. H., Pao, Y. H., & Wygnanski, I. J. 1976, Journal of Fluid Mechanics, 74, 209

Churchwell, E. 1997, ApJ, 479, L59

Churchwell, E., Povich, M. S., Allen, D., et al. 2006, ApJ, 649, 759

Crutcher, R. M. 1999, ApJ, 520, 706

Cunningham, A., Frank, A., & Hartmann, L. 2005, ApJ, 631, 1010

Cyganowski, C. J., Brogan, C. L., Hunter, T. R., Churchwell, E., & Zhang, Q. 2011, ApJ, 729, 124

Dalgarno, A., & McCray, R. A. 1972, ARA&A, 10, 375

de Geus, E. J., de Zeeuw, P. T., & Lub, J. 1989, A&A, 216, 44

Dekel, A., Sari, R., & Ceverino, D. 2009, ApJ, 703, 785

Dobbs, C. L., & Bonnell, I. A. 2006, MNRAS, 367, 873

Dobbs, C. L., Bonnell, I. A., & Pringle, J. E. 2006, MNRAS, 371, 1663

Dobbs, C. L., Burkert, A., & Pringle, J. E. 2011, MNRAS, 413, 2935

Dobbs, C. L., & Pringle, J. E. 2013, MNRAS, 432, 653

Dobbs, C. L., Pringle, J. E., & Burkert, A. 2012, MNRAS, 425, 2157

Dunham, M. M., Evans, N. J., Bourke, T. L., et al. 2010, ApJ, 721, 995

Egusa, F., Koda, J., & Scoville, N. 2011, ApJ, 726, 85

Elmegreen, B. G., & Elmegreen, D. M. 2005, ApJ, 627, 632

Elmegreen, B. G., & Lada, C. J. 1977, ApJ, 214, 725

Elmegreen, D. M. 1980, ApJ, 242, 528

Enoch, M. L., Young, K. E., Glenn, J., et al. 2006, ApJ, 638, 293

Ewen, H. I., & Purcell, E. M. 1951, Nature, 168, 356

Fiege, J. D., & Henriksen, R. N. 1996, MNRAS, 281, 1038

Field, G. B., Goldsmith, D. W., & Habing, H. J. 1969, ApJ, 155, L149

Glover, S. C. O., & Clark, P. C. 2012, MNRAS, 421, 9

Goldsmith, P. F., Heyer, M., Narayanan, G., et al. 2008, ApJ, 680, 428

Gong, H., & Ostriker, E. C. 2011, ApJ, 729, 120

Goodman, A. A., Rosolowsky, E. W., Borkin, M. A., et al. 2009, Nature, 457, 63

Goodman, A. A., Alves, J. F., Beaumont, C., et al. 2013, in American Astronomical Society Meeting Abstracts, Vol. 221, American Astronomical Society Meeting Abstracts, 234.01

Guillard, P., Boulanger, F., Pineau des Forêts, G., et al. 2012, ApJ, 749, 158

Gutermuth, R. A., Megeath, S. T., Myers, P. C., et al. 2009, ApJS, 184, 18

Heitsch, F., & Hartmann, L. 2008, ApJ, 689, 290

Heitsch, F., Slyz, A. D., Devriendt, J. E. G., Hartmann, L. W., & Burkert, A. 2006, ApJ, 648, 1052

Hennebelle, P., & Chabrier, G. 2008, ApJ, 684, 395

Hennebelle, P., & Pérault, M. 1999, A&A, 351, 309

Heyer, M., Krawczyk, C., Duval, J., & Jackson, J. M. 2009, ApJ, 699, 1092

Heyer, M. H., & Brunt, C. M. 2004, ApJ, 615, L45

Hollenbach, D. J., & Tielens, A. G. G. M. 1999, Reviews of Modern Physics, 71, 173

Hopkins, P. F. 2013, MNRAS, 433, 170

Inoue, T., & Inutsuka, S.-i. 2012, ApJ, 759, 35

Jackson, J. M., Finn, S. C., Chambers, E. T., Rathborne, J. M., & Simon, R. 2010, ApJ, 719, L185

Jackson, J. M., Rathborne, J. M., Shah, R. Y., et al. 2006, ApJS, 163, 145

Kauffmann, J., Pillai, T., & Goldsmith, P. F. 2013, ArXiv e-prints, arXiv:1308.5679

Kauffmann, J., Pillai, T., Shetty, R., Myers, P. C., & Goodman, A. A. 2010a, ApJ, 712, 1137

—. 2010b, ApJ, 716, 433

Keto, E., & Zhang, Q. 2010, MNRAS, 406, 102

Kim, W.-T., & Ostriker, E. C. 2002, ApJ, 570, 132

Kirk, H., Pineda, J. E., Johnstone, D., & Goodman, A. 2010, ApJ, 723, 457

Klessen, R. S. 2011, in EAS Publications Series, Vol. 51, EAS Publications Series, ed. C. Charbonnel & T. Montmerle, 133–167

Klessen, R. S., & Hennebelle, P. 2010, A&A, 520, A17

Koyama, H., & Inutsuka, S.-I. 2000, ApJ, 532, 980

Krumholz, M. R., & McKee, C. F. 2005, ApJ, 630, 250

Kryukova, E., Megeath, S. T., Gutermuth, R. A., et al. 2012, AJ, 144, 31

Lada, C. J. 1985, ARA&A, 23, 267

—. 2010, Royal Society of London Philosophical Transactions Series A, 368, 713

Lada, C. J., Lada, E. A., Clemens, D. P., & Bally, J. 1994, ApJ, 429, 694

Larson, R. B. 1972, MNRAS, 156, 437

—. 1981, MNRAS, 194, 809

Lazarian, A., & Pogosyan, D. 2004, ApJ, 616, 943

Lee, C.-F., Mundy, L. G., Reipurth, B., Ostriker, E. C., & Stone, J. M. 2000, ApJ, 542, 925

Lee, C.-F., Stone, J. M., Ostriker, E. C., & Mundy, L. G. 2001, ApJ, 557, 429

Lee, C. W., Bourke, T. L., Myers, P. C., et al. 2009, ApJ, 693, 1290

Lee, W.-K., & Shu, F. H. 2012, ApJ, 756, 45

Leisawitz, D., & Bash, F. 1982, ApJ, 259, 133

Lery, T., Henriksen, R. N., & Fiege, J. D. 1999, A&A, 350, 254

Li, G.-X., Qiu, K., Wyrowski, F., & Menten, K. 2013a, A&A, 559, A23

Li, G.-X., Wyrowski, F., Menten, K., & Belloche, A. 2013b, A&A, 559, A34

Li, H.-B., Blundell, R., Hedden, A., et al. 2011, MNRAS, 411, 2067

Li, H.-b., Fang, M., Henning, T., & Kainulainen, J. 2013c, MNRAS, 436, 3707

Li, H.-B., & Henning, T. 2011, Nature, 479, 499

Li, Z.-Y., & Shu, F. H. 1996, ApJ, 472, 211

Lockman, F. J. 1989, ApJS, 71, 469

Longmore, S. N., Pillai, T., Keto, E., Zhang, Q., & Qiu, K. 2011, ApJ, 726, 97

Longmore, S. N., Rathborne, J., Bastian, N., et al. 2012, ApJ, 746, 117

Longmore, S. N., Kruijssen, J. M. D., Bastian, N., et al. 2014, ArXiv e-prints, arXiv:1401.4175

Lynds, B. T. 1970, in IAU Symposium, Vol. 38, The Spiral Structure of our Galaxy, ed. W. Becker & G. I. Kontopoulos, 26

Mac Low, M.-M., & Klessen, R. S. 2004, Reviews of Modern Physics, 76, 125

Matzner, C. D. 2007, ApJ, 659, 1394

Matzner, C. D., & McKee, C. F. 1999, ApJ, 526, L109

McKee, C. F., & Holliman, II, J. H. 1999, ApJ, 522, 313

McKee, C. F., & Ostriker, J. P. 1977, ApJ, 218, 148

McKee, C. F., & Tan, J. C. 2002, Nature, 416, 59

—. 2003, ApJ, 585, 850

McLaughlin, D. E., & Pudritz, R. E. 1996, ApJ, 469, 194

Men'shchikov, A., André, P., Didelon, P., et al. 2010, A&A, 518, L103

Mercer, E. P., Clemens, D. P., Meade, M. R., et al. 2005, ApJ, 635, 560

Mueller, K. E., Shirley, Y. L., Evans, II, N. J., & Jacobson, H. R. 2002, ApJS, 143, 469

Najita, J. R., & Shu, F. H. 1994, ApJ, 429, 808

Nakamura, F., & Li, Z.-Y. 2007, ApJ, 662, 395

Nakanishi, H., & Sofue, Y. 2006, PASJ, 58, 847

Norman, C. A., & Ferrara, A. 1996, ApJ, 467, 280

Ntormousi, E., & Burkert, A. 2011, ArXiv e-prints, arXiv:1111.1859

Nutter, D., Kirk, J. M., Stamatellos, D., & Ward-Thompson, D. 2008, MNRAS, 384, 755

Offner, S. S. R., Lee, E. J., Goodman, A. A., & Arce, H. 2011, ApJ, 743, 91

Ostriker, E. C. 1997, ApJ, 486, 291

Parkin, E. R., Pittard, J. M., Hoare, M. G., Wright, N. J., & Drake, J. J. 2009, MNRAS, 400, 629

Peretto, N., André, P., Könyves, V., et al. 2012, A&A, 541, A63

Pineda, J. E., Rosolowsky, E. W., & Goodman, A. A. 2009, ApJ, 699, L134

Plume, R., Jaffe, D. T., Evans, II, N. J., Martin-Pintado, J., & Gomez-Gonzalez, J. 1997, ApJ, 476, 730

Polychroni, D., Schisano, E., Elia, D., et al. 2013, ApJ, 777, L33

Pon, A., Toalá, J. A., Johnstone, D., et al. 2012, ApJ, 756, 145

Pringle, J. E., Allen, R. J., & Lubow, S. H. 2001, MNRAS, 327, 663

Qiu, K., Zhang, Q., & Menten, K. M. 2011, ApJ, 728, 6

Qiu, K., Zhang, Q., Menten, K. M., Liu, H. B., & Tang, Y.-W. 2013, ArXiv e-prints, arXiv:1311.0566

Qiu, K., Zhang, Q., Wu, J., & Chen, H.-R. 2009, ApJ, 696, 66

Rathborne, J. M., Jackson, J. M., & Simon, R. 2006, ApJ, 641, 389

Rathborne, J. M., Johnson, A. M., Jackson, J. M., Shah, R. Y., & Simon, R. 2009, ApJS, 182, 131

Ren, J. Z., Liu, T., Wu, Y., & Li, L. 2011, MNRAS, 415, L49

Reynolds, O. 1895, Royal Society of London Philosophical Transactions Series A, 186, 123

Ridge, N. A., Di Francesco, J., Kirk, H., et al. 2006, AJ, 131, 2921

Robertson, B., & Goldreich, P. 2012, ApJ, 750, L31

Rogers, M. M., & Moser, R. D. 1994, Physics of Fluids, 6, 903

Roman-Duval, J., Federrath, C., Brunt, C., et al. 2011, ApJ, 740, 120

Roman-Duval, J., Jackson, J. M., Heyer, M., et al. 2009, ApJ, 699, 1153

Roman-Duval, J., Jackson, J. M., Heyer, M., Rathborne, J., & Simon, R. 2010, ApJ, 723, 492

Rosolowsky, E. W., Pineda, J. E., Kauffmann, J., & Goodman, A. A. 2008, ApJ, 679, 1338

San Jose-Garcia, I., Mottram, J. C., Kristensen, L. E., et al. 2013, ArXiv e-prints, arXiv:1301.4658

Schinnerer, E., Meidt, S. E., Pety, J., et al. 2013, ArXiv e-prints, arXiv:1304.1801

Schneider, S., & Elmegreen, B. G. 1979, ApJS, 41, 87

Schuller, F., Menten, K. M., Contreras, Y., et al. 2009, A&A, 504, 415

Shepherd, D. S., Watson, A. M., Sargent, A. I., & Churchwell, E. 1998, ApJ, 507, 861

Shetty, R., & Ostriker, E. C. 2006, ApJ, 647, 997

Shu, F. H., Najita, J., Ostriker, E. C., & Shang, H. 1995, ApJ, 455, L155

Shu, F. H., Ruden, S. P., Lada, C. J., & Lizano, S. 1991, ApJ, 370, L31

Simon, R., Jackson, J. M., Clemens, D. P., Bania, T. M., & Heyer, M. H. 2001, ApJ, 551, 747

Simpson, R. J., Povich, M. S., Kendrew, S., et al. 2012, MNRAS, 424, 2442

Smith, R. J., Clark, P. C., & Bonnell, I. A. 2009, MNRAS, 396, 830

Solomon, P. M., Rivolo, A. R., Barrett, J., & Yahil, A. 1987, ApJ, 319, 730

Sousbie, T. 2011, MNRAS, 414, 350

Spergel, D. N., Bean, R., Doré, O., et al. 2007, ApJS, 170, 377

Stahler, S. W. 1994, ApJ, 422, 616

Starck, J. L., Donoho, D. L., & Candès, E. J. 2003, A&A, 398, 785

Stil, J. M., Taylor, A. R., Dickey, J. M., et al. 2006, AJ, 132, 1158

Tan, J. C. 2000, ApJ, 536, 173

Tan, J. C., Kong, S., Butler, M. J., Caselli, P., & Fontani, F. 2013, ArXiv e-prints, arXiv:1303.4343

Tasker, E. J. 2011, ApJ, 730, 11

Tasker, E. J., & Tan, J. C. 2009, ApJ, 700, 358

Testi, L., & Sargent, A. I. 1998, ApJ, 508, L91

Thompson, M. A., Urquhart, J. S., Moore, T. J. T., & Morgan, L. K. 2012, MNRAS, 421, 408

Toomre, A. 1964, ApJ, 139, 1217

Toomre, A., & Toomre, J. 1972, ApJ, 178, 623

Tsai, A.-L., Matsushita, S., Kong, A. K. H., Matsumoto, H., & Kohno, K. 2012, ApJ, 752, 38

Turk, M. J., Smith, B. D., Oishi, J. S., et al. 2011, ApJS, 192, 9

Urquhart, J. S., Hoare, M. G., Purcell, C. R., et al. 2009, A&A, 501, 539

van der Tak, F. F. S., Black, J. H., Schöier, F. L., Jansen, D. J., & van Dishoeck, E. F. 2007, A&A, 468, 627

Van Loo, S., Butler, M. J., & Tan, J. C. 2013, ApJ, 764, 36

Vázquez-Semadeni, E., Colín, P., Gómez, G. C., Ballesteros-Paredes, J., & Watson, A. W. 2010, ApJ, 715, 1302

Vázquez-Semadeni, E., Gómez, G. C., Jappsen, A. K., et al. 2007, ApJ, 657, 870

Walch, S. K., Whitworth, A. P., Bisbas, T., Wünsch, R., & Hubber, D. 2012, MNRAS, 427, 625

Walsh, A. J., Myers, P. C., & Burton, M. G. 2004, ApJ, 614, 194

Walsh, A. J., Breen, S. L., Britton, T., et al. 2011, MNRAS, 416, 1764

Ward-Thompson, D., Kirk, J. M., André, P., et al. 2010, A&A, 518, L92

Watson, C., Araya, E., Sewilo, M., et al. 2003, ApJ, 587, 714

Watson, C., Zweibel, E. G., Heitsch, F., & Churchwell, E. 2004, ApJ, 608, 274

Weaver, H. F. 1970, in IAU Symposium, Vol. 39, Interstellar Gas Dynamics, ed. H. J. Habing, 22

Whiting, M. T. 2012, MNRAS, 421, 3242

Whitworth, A. P., Bhattal, A. S., Chapman, S. J., Disney, M. J., & Turner, J. A. 1994, A&A, 290, 421

Whitworth, A. P., & Francis, N. 2002, MNRAS, 329, 641

Whitworth, A. P., & Ward-Thompson, D. 2001, ApJ, 547, 317

Williams, J. P., Blitz, L., & McKee, C. F. 2000, Protostars and Planets IV, 97

Williams, J. P., de Geus, E. J., & Blitz, L. 1994, ApJ, 428, 693

Wilson, R. W., Jefferts, K. B., & Penzias, A. A. 1970, ApJ, 161, L43

Acknowledgements

Curriculum vitae of Guang-Xing Li

Contact Information

Office Address:	Auf dem Hügel 69, D-53121, Bonn, Germany
Telephone Number:	+49 (228) 525 468
E-mail:	gxli@mpifr-bonn.mpg.de, ligx.ngc7293@gmail.com

Research Interests

- Structure of Milky Way and other galaxies
- Star formation in molecular clouds
- Molecular outflows from forming stars
- Theory of accretion disks
- Astrophysical turbulence
- Radiative transfer
- Advanced data visualization

Education

Max-Planck Institute for Radio Astronomy, Bonn, Germany

Dr. rer. nat. Candidate, Astrophysics, Aug. 2010 (expected graduation date: Jun. 2014)

Topic:	Mathesis of star formation – from kiloparsec scale to a parsec
Advisors:	Prof. Karl Menten, Dr. Friedrich Wyrowski, Prof Pavel Kroupa

University of Science and Technology, Hefei, China

M.S., Astrophysics, Jul. 2010

Dissertation Topic:	Observational signature of relativistic accretion disks
Advisor:	Prof. Ye-Fei Yuan

Peking University, Beijing, China

B.S. , Electronics, Jul. 2007

Dissertation Topic:	Hydrostatic solution of relativistic quark stars
Advisor:	Prof. Ren-Xin Xu

Professional Experiences

Teaching Assistant of *Thermodynamics and Statistical Physics* for undergraduate students (Sept. 2007 – Jan. 2008)

Honors and Awards

Guang-Hua Scholarship for excellent graduate student. Oct. 2009
Prize for Outstanding Graduate Student, issued by Personnel Bureau Centres of Excellence of Anhui Province. Apr. 2010

Publications

- Guang-Xing Li, Keping Qiu, Friedrich Wyrowski, Karl Menten, 2013, **"Turbulent Entrainment Origin of Protostellar Outflows."**, A&A, 559, A23

- Guang-Xing Li, Friedrich Wyrowski, Karl Menten, Arnaud Belloche, 2013, " **A 500 pc filamentary gas wisp in the disk of the Milky Way."**, A&A, 559, A34

- N. Peretto, G. A. Fuller, Ph. Andre, D. Arzoumanian, S. Bardeau, S. Duarte Puertas, J. P. Guzman, C. Lenfestey, G.-X. Li, F. A. Olguin, V. M. Rivilla, H. de Villiers, J. Williams, **"SDC13 infrared dark clouds: Longitudinally collapsing Filaments?"**, A&A, 561, A83

- Guang-Xing Li, Ye-Fei Yuan, Xinwu Cao, **"Emergent spectra from disks surrounding Kerr black holes: Effect of photon trapping and disk self-shadowing."** ApJ, 715, 623